NTNU

Norwegian University of
Science and Technology

Influence of precipitate-free zones on tensile ductility and tear resistance of 6000 aluminium alloys

An experimental and numerical study

Sondre Sævareid

Master of Science in Mechanical Engineering
Submission date: December 2017
Supervisor: Odd Sture Hopperstad, KT

Norwegian University of Science and Technology
Department of Structural Engineering

Abstract

The influence of the precipitate free zones (PFZs) on ductility of aluminium alloys of the 6xxx- series was investigated. Precipitate free zones are zones along the grain boundary with no precipitates, resulting in a softer zone compared to the grain interior. The width of these zones can vary and can be changed using different quenching rates. How the PFZs affect the mechanical properties of the 6xxx-series is not fully examined and was the main topic of this thesis. Three 6xxx-series alloys were investigated: AA6060, AA6082.25 and AA6082.50. How the PFZs influence the ductility was investigated by using two different quenching rates after solution heat-treatment: air-cooling and water-quenching at room temperature. This was done to achieve two different PFZ-widths, where the air-cooling would result in the widest PFZ. It was expected that a wider PFZ resulted in a less ductile material. The experiments were conducted using three tests: the round smooth tensile test, the round v-notch tensile test, and the Kahn tear test. The results were then compared both experimentally and numerically.

The smooth tensile test and the v-notch tensile test were used for material calibration. Central mechanical properties from the Kahn tear test were obtained and used to compare the air-cooled and water-quenched test specimens. One of these properties was the unit propagation energy (UPE) and is a measure of the material's ability to withstand crack growth. This was used to investigate the ductility of the different materials. The air-cooled specimens all had wider PFZs compared to their water-quenched counterparts, which was expected. However, this did not result in a significant reduced ductility of the air-cooled test specimens. In three out of six cases, the UPE for the air-cooled specimens was larger compared to their water-quenched counterparts. In the cases where the water-quenched specimens had higher UPEs, it was due to an increased maximum force. The PFZ-width appeared not to have a large influence on tear resistance for the quenching rates used.

A numerical study was performed in which all tests were simulated using the Gurson-Tvergaard-Needleman (GTN) model. The fracture model was calibrated by only varying the initial void volume fraction. The GTN-model accounts for damage and failure by void nucleation, growth and coalescence only and the model gave good results where this fracture mode was dominant. Some of the materials had a significant presence of fracture along the grain boundaries. For these materials, the resulting forces in the simulations were overestimated, indicating that the presence of fracture along the grain boundaries happens with less resistance.

A wider PFZ resulted in an increase of intergranular fracture. However, this increase did not affect the ductility in terms of the UPE. The difference in strength between the grain interior and PFZ was probably more important than the width of the PFZ. The air-cooled specimens had a significant lower strength compared to their water-quenched counterparts and resulted in material with higher ductility.

Preface

This thesis was the final effort of my Master in Science degree in Mechanical Engineering at NTNU, specialising in Applied Mechanics. My thesis was completed during 20 weeks in the autumn of 2017 and written for the Structural Impact Laboratory (Simlab) at the Norwegian University of Science and Technology (NTNU). The work was done under supervision of Professor Odd Sture Hopperstad and the PhD Candidates Bjørn Håkon Frodal and Emil Christiansen at the Department of Structural Engineering at NTNU.

Acknowledgements

This thesis would not have been possible without the help of my supervisors professor Odd Sture Hopperstad and the PhD candidates Bjørn Håkon Frodal and Emil Christiansen. Professor Odd Sture Hopperstad has provided me with a lot of theory in the form of relevant articles and arranging weekly meetings where I got a lot of input. The PhD candidates Bjørn Håkon Frodal and Emil Christiansen also attended these meetings, which I am very grateful for. Bjørn Håkon Frodal was always available and helped me a lot with the simulations in Abaqus and whatever else I needed help for. Emil Christiansen was very helpful with everything regarding the microstructure and fractography. His knowledge about PFZs and other metallurgical aspects has been very useful. He also provided all the pictures from SEM and TEM, which was very beneficial. Professor Odd Sture Hopperstad and Bjørn Håkon Frodal has spent many hours reading my thesis and giving valuable input regarding my work, which I am very grateful for. I would also like to thank Trond Auestad and Tore Kristensen for conducting the experimental tests.

I would also like to thank my family for supporting and helping me with the finishing touches on my thesis.

Nomenclature

δ_{ij}	Kroenecker delta
$\dot{\lambda}$	Plastic multiplier
$\dot{\varepsilon}^p_{ij}$	Plastic strain rate
$\dot{\varepsilon}_p$	Volumetric plastic strain rate
$\dot{f}$	Change of void volume fraction
$\dot{f}_{gr}$	Change of void volume fraction due to void growth
$\dot{f}_{nucl}$	Change of void volume fraction due to void nucleation
$\boldsymbol{\sigma}$	Stress tensor
$\boldsymbol{\sigma'}$	Deviatoric stress tensor
$\boldsymbol{\sigma}_h$	Hyrostatic stress tensor
σ_1	First principal stress
σ_2	Second principal stress
σ_3	Third principal stress
σ_h	Hydrostatic stress
σ_t	True stress
σ_y	Yield stress
σ_{eq}	von Mises stress
ε_e	Elastic strain
ε_p	Plastic strain at necking

ε_p	Plastic strain
ε_t	Logarithmic strain
A	Cross section
A_0	Initial cross section
AC	Air-cooled
b	Width from notch root to the back of the Kahn specimen
C_i	Strain hardening parameter in the Voce-rule
D_0	Initial diameter
D_x	Diameter in x-direction
D_y	Diameter in y-direction
E	Young' modulus
ED	Extrusion direction
F	Force
f	Void volume fraction
f_0	Initial void volume fraction
f_c	Critical void volume fraction
f_F	Void volume fraction at failure
f_K	Void volume fraction at the formation of a crack
f_p	Area fraction of constituent particles
I_1	First principal invariant
IE	Initiation energy
J_2	Second deviatoric invariant
p	Plastic strain
PE	Propagation energy
Q_i	Strain hardening parameter in the Voce-rule
T	Triaxiality ratio
t	Thickness
TD	Transversal direction

UIE Unit initiation energy

UPE Unit propagation energy

WQ Water-quenched

Table of Contents

Chapter 1

Introduction

Aluminium alloys are lightweight materials and with a stiffness of 1/3 compared to steel alloys they have a high strength to weight ratio. Aluminium alloys are also good energy absorbents. The high strength and low weight, makes aluminium alloys very desirable for the transportation industry. However, due to the lower strength compared to steel alloys, steel alloys are preferable in situations that demands high stiffness, for instance components influencing the handling properties of a car. Aluminium alloys are much used in the bodywork of cars where the ability to absorb energy in the event of a car crash is important.

Strength and ductility are central properties for aluminium alloys, but they are known to be at the expense of each other [1], i.e. it is not possible to achieve high strength and high ductility at the same time. Knowing more about the competition between strength and ductility is important to ensure the best possible properties for a given application.

The mechanical properties for age-hardening aluminium alloys can be altered through quenching and ageing. Comparing the effect of different quenching rates and ageing periods is of interest to learn how this affects the microstructure and the mechanical properties. Dumont et al. [2] investigated the effect of different quenching rates and ageing periods for an aluminium alloy of the 7xxx-series. This research was done in the form of a Kahn tear test and special emphasis was put on the effects quenching and ageing had on the notch resistance. Fractography and microstructure were investigated to find the fracture mechanisms present. Similar research was also done by Morgeneyer et al. [3] who found that the notch resistance was heavily reduced using air-cooling instead of a water-quench. Gräf and Hornbogen [4] found that at peak ageing condition of a Al-Zn-Mg alloy, localisation of strain along the grain boundaries and inter-crystalline cracking dominated.

In aluminium alloys, precipitate free zones (PFZs) are present along the grain boundaries. Research by Unwin et al. [5] showed that the width of the PFZ varies with different quenching methods. The PFZs are softer zones compared to the grain interior, and plastic deformations favour to take place in these zones. This may compromise the toughness

and tear resistance of the material. How the PFZ influences the ductility, and thus the tear resistance of the alloys is not fully understood. This will be further examined in this thesis.

Fracture in aluminium alloys predominantly happens by void nucleation, growth and coalescence. A porous plasticity model is needed to be able to analyse these fractures numerically. The one used in this thesis is the model first proposed by Gurson [6], later modified by Tvergaard and Needleman [7], the Gurson-Tvergaard-Needleman-model, or GTN-model. Tvergaard and Needleman [7] analysed the necking and failure of a round tensile test where the GTN- model was used to account for both void nucleation, growth and coalescence. The analysis started with no initial voids in the material. Due to high hydrostatic tension in the centre of the test specimen, voids formed, eventually coalescing creating a macroscopic crack. At the end, all stress carrying capacity vanished and failure occurred.

Numerical simulations of the Kahn tear test have been conducted by Chabanet et al. [8] where the simulations were done using the GTN-model and a cohesive zone model. It was found that the GTN-model was able to model the behaviour of the Kahn tear test. Some limitations were found in that the GTN-model, as it was not able to model slant fracture which was present in the experimental Kahn tear test.

The alloys used in this thesis are of the 6xxx-series, namely AA6060, AA6082.25 and AA6082.50. The test specimens in use are all made from a flat shaped extruded profile. Extrusion of aluminium alloys gives anisotropic mechanical behaviour. The alloys in use have also been shown to be pressure sensitive [9].

To what extent AA6060, AA6082.25 and AA6082.50 are affected in terms of ductility due to the PFZ is not fully examined and will be further investigated in this thesis. Kahn tear tests will be performed with two different quenching methods, air-cooling and water-quenching at room temperature. The test specimens will be aged to peak strength (T6). The influence of these quenching rates on the notch resistance, resistance to crack propagation and maximum force will be examined.

The microstructure will be investigated to find possible reasons for change in mechanical properties. Both scanning electron microscopy (SEM) and transmission electron microscopy (TEM) will be used. SEM is used to find the fracture mechanisms that are present, and TEM is used to find the width of the PFZ and other microstructural characteristics.

In the numerical part, Abaqus/Explicit will be used with the GTN-model. All the experiments conducted will be simulated. The round smooth tensile test will be performed to calibrate the hardening behaviour. The results of the round v-notch tensile test will be used to calibrate the fracture model. At the end, the Kahn tear test will be simulated with the hardening behaviour and fracture model to investigate the limitations of the GTN-model. The GTN- model will be used without void nucleation and the void volume fraction at failure together with the critical void volume fraction will be held constant. Pressure sensitivity and anisotropy effects will not be accounted for in the simulations. There will neither be a model for fractures along the grain boundaries.

A brief overview of the different chapters is covered below.

Chapter 2- Theory
This chapter covers the relevant theory needed for this thesis. The topics covered are; materials mechanics, ductile fracture by void nucleation, growth and coalescence, the Gurson-Tvergaard-Needleman model, ageing and quenching and finally an introduction to precipitate free zones.

Chapter 3- Experimental study
The smooth tensile tests, the v-notch tensile tests and the Kahn tear tests were performed. The properties are compared using two different quenching rates for the three different tests, and two different material orientations for the Kahn tear test. Central mechanical properties are obtained and compared to each other.

Chapter 4- Numerical study
The fracture model is calibrated by simulating the v-notch tensile test with different parameters in the GTN-model. The results are compared to experimental values to verify that they give a satisfactory result. The smooth tensile test is checked for the calibrated values from the v-notch tensile test. Finally, the Kahn tear test is modelled using the calibrated parameters.

Chapter 5- Concluding remarks
The experimental results are evaluated and compared with the simulations.

Chapter 6- Future work
What can be further explored after this thesis.

Chapter 2

Theory

In this chapter, an introduction to the theory needed for the topic of the Master's thesis is covered. First, an introduction to stress tensors and stress invariants are given. Next, a mathematical approach for modelling plastic properties is shown, followed by central terms for the Kahn tear test. After that, an introduction to aluminium alloys and extrusion is given. Later, different fracture mechanisms, followed by void growth and the Gurson-Tvergaard-Needleman model are described. Lastly, an introduction to heat treatment and precipitate free zones is given.

2.1 Materials mechanics

2.1.1 Stress

For a 3D- stress state, there can be nine stress components. The stress tensor is:

$$\boldsymbol{\sigma} = [\sigma_{ij}] \tag{2.1}$$

From the stress tensor, three invariants can be defined. These invariants are the same for a given stress state independent of the orientation of the axes. Only the first stress invariant will be presented, and it is:

$$I_1 = \sigma_{kk} = \sigma_{11} + \sigma_{22} + \sigma_{33} \tag{2.2}$$

The stress tensor is often divided into two parts, the hydrostatic, and the deviatoric stress tensor. The hydrostatic stress, defined as:

$$\sigma_h = \frac{I_1}{3} \tag{2.3}$$

The hydrostatic stress tensor is defined as:

$$\boldsymbol{\sigma}_h = \sigma_h[\delta_{ij}] \tag{2.4}$$

where δ_{ij} is the Kroenecker delta defined as equal to one when $i = j$ and equal to zero otherwise. The deviatoric stress tensor is defined by subtracting the hydrostatic stress tensor from the stress tensor:

$$\boldsymbol{\sigma}' = \boldsymbol{\sigma} - \boldsymbol{\sigma}_h \tag{2.5}$$

The reason for splitting the stress tensor into two different tensors is that these tensors influence the material in fundamentally different ways. The hydrostatic tensor contributes to volume deformation. The deviatoric stress tensor contributes to shape change. The hydrostatic part of the stress tensor does in practice not influence the yielding of metals [10]. Yield criteria for metals are therefore mostly a function of the deviatoric stress tensor. One of these is the von Mises yield criterion, which is defined as:

$$\Phi(\boldsymbol{\sigma}) = \sigma_{eq} - \sigma_y = 0 \tag{2.6}$$

where σ_y is the yield stress, and σ_{eq} is the von Mises stress defined as:

$$\sigma_{eq} = \sqrt{3J_2} \tag{2.7}$$

where J_2 is the second invariant of the deviatoric stress tensor. This invariant is defined as:

$$J_2 = \frac{1}{2}\sigma'_{ij}\sigma'_{ij} = \frac{1}{6}\big((\sigma_1 - \sigma_2)^2 + (\sigma_2 - \sigma_3)^2 + (\sigma_3 - \sigma_1)^2\big) \tag{2.8}$$

where $\sigma_1, \sigma_2,$ and σ_3 are the principal stresses.

2.1.2 Stress triaxiality

Stress triaxiality is a function of the hydrostatic stress and the von Mises stress. The triaxiality relation T is defined as:

$$T = \frac{\sigma_h}{\sigma_{eq}} \tag{2.9}$$

Both σ_h and σ_{eq} are invariants, so triaxiality is a function of invariants only. The different experiments that will be conducted in this thesis exhibit different levels of triaxiality and this will be further explored in Chapter 4.

2.1.3 Measures for calibration

Materials, in general, have an elastic zone, and a plastic zone. The main difference between them is that loading within the elastic zone does not lead to any permanent deformations, but loading in the plastic zone does. When looking at a stress-strain diagram, the elastic zone is often recognized by a straight line. The slope of this line is the Young's modulus. When the plastic zone starts, the slope changes and the curve become nonlinear. The transition between the two zones is the yield strength. The yield strength is the maximum stress the material can withstand without any permanent deformations. Below, a step by step approach for fitting a mathematical model to a material's behaviour is given

To calibrate the material model for finite element analysis in this thesis, a material calibration will be performed using a round smooth tensile test. From the test data, curve fitting can be performed to define the plastic behaviour. The steps for achieving this curve is explained in this section. The first quantities needed are the true stress and true strain. True stress is defined as:

$$\sigma_t = \frac{F}{A} \tag{2.10}$$

where F is the force applied, and A is the cross section measured. The accompanying true strain or logarithmic strain is defined as:

$$\varepsilon_t = \ln\left(\frac{A_0}{A}\right) \tag{2.11}$$

where A_0 is the initial cross section. The Young's modulus mentioned above is expressed as:

$$E = \frac{\sigma_t}{\varepsilon_e} \tag{2.12}$$

where ε_e is the elastic strain. Later, experiments will be performed with both round smooth tensile tests, and round v-notch tensile tests, see Section 3.4. The initial cross section is circular and expressed as:

$$A = \pi\frac{D_0^2}{4} \tag{2.13}$$

where D_0 is the initial diameter. When force is applied, the cross-section is assumed to take an elliptical shape, the cross-section then becomes:

$$A = \pi\frac{D_x D_y}{4} \tag{2.14}$$

where D_x and D_y are the diameter in x- and y-direction respectively. Now the true stress and true strain are defined. However, these are not the final quantities needed for the material calibration. Next, the plastic strain must be calculated. That is done by the following equation:

$$\varepsilon_p = \varepsilon_t - \frac{\sigma_t}{E} \tag{2.15}$$

where σ_t/E is the elastic strain. Next, a Bridgman-LeRoy [11] correction must be performed. This correction is done after necking because necking induces a complex triaxial stress state, which means that there are stresses in multiple directions, and this must be corrected. Necking occurs at maximum force or dF=0. The correction is done by calculating the equivalent stress σ_{eq} after maximum force, where σ_{eq} is defined as:

$$\sigma_{eq} = \frac{\sigma_t}{(1 + 2R/a)\ln(1 + a/2R)} \tag{2.16}$$

where a/R is:

$$\frac{a}{R} = 1.1(\varepsilon_p - \varepsilon_{p,neck}) \tag{2.17}$$

where $\varepsilon_{p,neck}$ is the plastic strain at necking. The plastic strain together with σ_{eq} are the quantities needed for a material calibration. Note that the σ_{eq} is the same as σ_t before necking Plotting these two quantities against each other and fitting a curve using a least square method gives the plastic properties of the materials. The function that the data should be fitted to is defined by the Voce-rule, which is defined as follows:

$$\sigma_y(p) = \sigma_0 + \sum_{i=1}^{2} Q_i(1 - \exp(-C_i p)) \tag{2.18}$$

where $\sigma(p)$ is the flow stress and Q_i, and C_i are hardening parameters and p is the plastic strain. The different parameters for the different alloys and heat treatments will be presented in section 3.4. There exist numerous equations that can be used to fit the experimental data.

2.2 The Kahn tear test

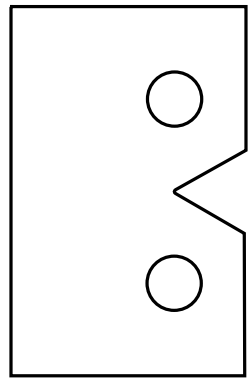

Figure 2.1: Geometry of the Kahn tear test.

The Khan tear test is used to provide a measure of notch toughness and resistance to crack growth [12]. In figure 2.1, the geometry of the Kahn tear test can be seen. It is a rectangular shape with two holes for loading and a notch. The two main quantities obtained from the Kahn tear test are the Unit Initiation Energy (UIE), and the Unit Propagation Energy(UPE). The UIE indicates a material's ability to withstand crack initiation and is defined as:

$$UIE = \frac{IE}{bt} \tag{2.19}$$

where IE is the initiation energy which is the energy needed for the crack to initiate. The initiation energy is the area under the force-displacement curve befor maximum force and

is indicated in figure 2.2. b is the distance from the notch root to the back of the specimen, and t is the thickness of the specimen. The UPE is defined similarly:

$$UPE = \frac{PE}{bt} \tag{2.20}$$

where PE is the propagation energy, the energy needed to propagate the crack to failure. The PE is also shown in figure 2.2. The UPE indicates the material's ability to prevent crack propagation and can be seen as a combination of strength and ductility [12].

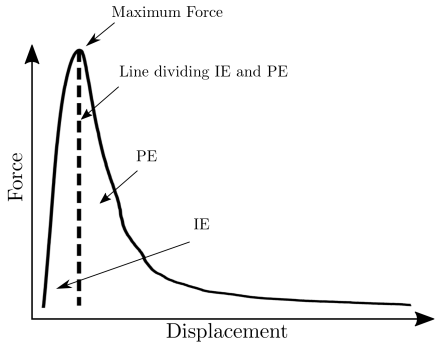

Figure 2.2: A force-displacement curve showing the area used for UIE and UPE.

2.3 Aluminium alloys

Aluminium is an element characterized by its low weight, making it very applicable for light weight structures. However, pure aluminium is very soft, so to achieve a more desirable material characteristic adding alloying elements is often of interest. Aluminium alloys are classified into different alloying families, dependent on which alloying elements that are present. The families are the 1xxx-,2xxx-,3xxx-,5xxx-,6xxx-, 7xxx-, and 8xxx-series. These families may be split into heat- treatable, and non-heat-treatable alloys. The non-heat-treatable alloys are the 1xxx-, 3xxx-, 5xxx-, and 8xxx- series.

The 1xxx- family is the high purity aluminium family. In this family is among others the super-purity aluminium consisting of 99.99% aluminium [13]. The 2xxx- family is divided into two groups, one having copper as the main alloying element, the other containing both copper and magnesium. The Cu- Mg family led to the discovery of age-hardening, done by Alfred Wilm in 1906 [13]. The 2xxx-family is frequently used in airplanes. The next family, the 3xxx-family has manganese and magnesium as the main alloying elements. Typical properties are high ductility, moderate strength and excellent resistance to corrosion. Magnesium is the main alloying element in the 5xxx- family. Aluminium and magnesium can form solid solution using a magnesium content ranging from 0.8% to 5%, which makes it possible to achieve many different mechanical properties. This family has excellent corrosion resistance, making them applicable to hulls for smaller boats [13]. The 6xxx- family contains magnesium and silicon as primary alloying elements. Medium

strength, good weldability, and corrosion resistance distinguish this family. This family is frequently extruded [13]. The 7xxx- family is also split into two groups, one having zinc and magnesium as main alloying elements, the other containing zinc, magnesium and copper. The Zn-Mg-Cu alloys have a high strength/weight ratio, making them relevant to the aircraft industry. At last is the 8xxx- family, consisting of alloys with many different alloying elements. Among these is the 8001 containing nickel and iron, used in nuclear energy installations [13].

2.4 Extrusion

Extrusion consists of forcing a billet, often preheated, through a die. The die's cross-section may be of a complex shape, which may be difficult to achieve with other manufacturing processes. Another advantage of extrusion is the possibility to create long beams without the need for welding. Aluminium alloys are suitable for extrusion due to their good workability, but high amounts of alloying elements make the process of extrusion more difficult [14]. The 6xxx-series is the most used for extrusion, because of its suitable material characteristics, economical production and it is generally easy to extrude [14].

2.5 Elementary fracture mechanisms

There are two main fracture paths; through the grains (transgranular fracture), or along the grain boundary (intergranular fracture) [2]. A fracture path through a test specimen's cross-section can be a combination of the two, depending on the microstructure. The fracture paths can also be split into different fracture mechanisms. During a Kahn tear test, four central fracture mechanisms are present [2]. They can be present together, and the presence of each fracture mechanism can be measured by analysing the fracture surface. The mechanisms as written by Dumont et al.[2] are:

1. Fracture or decohesion of the coarse constituent particles.
2. Ductile transgranular fracture, characterised by dimples, the centre of which contain constituent particles.
3. Ductile transgranular shear fracture, showing large planar areas crossed by intense slip lines.
4. Ductile intergranular (or inter-subgranular) fracture, characterised by relatively smooth surfaces revealing the initial grain structure.

The level of each fracture mode is largely dependent on ageing and quenching. Dumont et al. [2] examined the area fraction of each fracture mechanism for different material orientations and heat treatments. The testing they did was in the form of a Kahn tear test. It was found that the area fraction of intergranular fracture increased significantly from a fast quench to a slow quench [2]. The notch resistance, which was measured by the UIE, was found to decrease with a faster quench. The area fraction of intergranular fracture never exceeded 50%, and this was not high enough to explain the large loss in UIE. The

drop in UIE was then not found to be due to an increase in intergranular fracture only. There had to be a mechanism within the grains to also account for this drop [2].

2.6 Ductile fracture

Ductile materials usually fail by nucleation, growth, and coalescence of voids [15]. Many materials have initial microscopic voids in the material matrix. A ductile fracture is commonly observed in three stages. These stages, as written by Anderson[15], are:

1. Formation of a free surface at an inclusion- or second-phase particle by either interface decohesion or particle cracking.

2. Growth of the void around the particle, by means of plastic strain and hydrostatic stress.

3. Coalescence of the growing void with adjacent voids.

Void nucleation occurs when a critical stress value causes the second phase particle to debond from the matrix. As the stresses increases, the nucleated voids and the initial voids starts to grow. At a critical size, the voids coalesce with their neighbours and failure occurs[15]. Void nucleation will not be implemented in the later numerical study, and no more theory on void nucleation will be presented.

2.6.1 Void growth and coalescence

If the initial volume fraction is lower than 10%, it can be expected that the voids will grow independently at the early stages of plastic deformations [15]. Upon further loading, they start interacting with neighbouring voids. Plastic strains then become concentrated along a sheet of voids [15]. Eventually, internal necking between the voids occur, causing them to coalesce. Finally, the material fails when voids along a path have all grown together. The course of void nucleation, growth and coalescence can be seen in Figure 2.3.

At necking in a uniaxial tensile test, a triaxial stress state develops in the centre of the neck region. This stress state induces void growth and coalescence. After fracture, the centre of the specimen will have a different fracture surface compared to the outer part. The outer part of the fracture surface has a relatively smooth surface. The centre has a coarser surface, and small dimples can be seen. The coarser surface is due to fact to the fact that there were larger hydrostatic stresses present in the centre, resulting in a higher triaxiality [15].

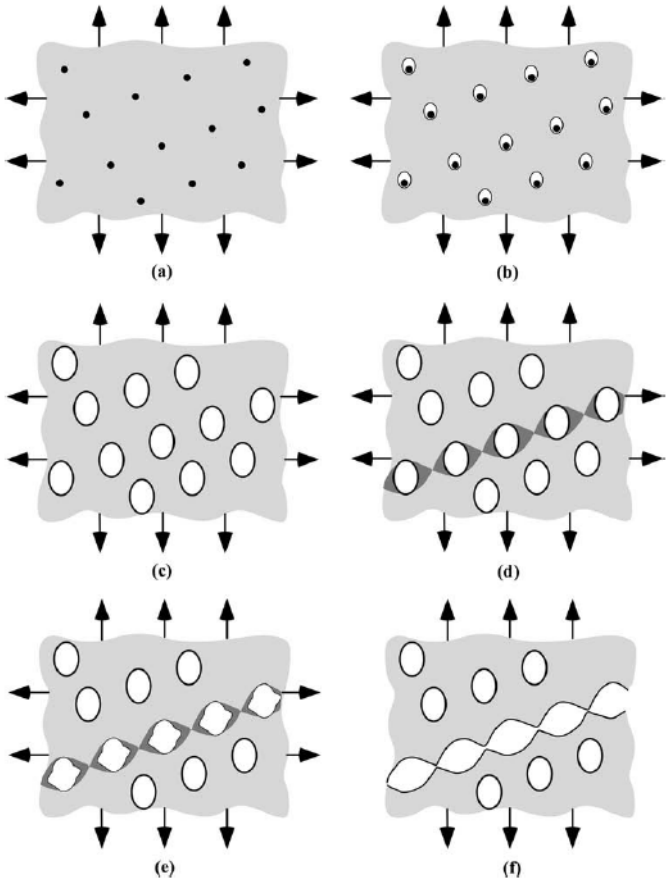

Figure 2.3: Failure resulted by void nucleation, growth and coalescence. (a) Inclusions in a ductile matrix, (b) voids starts to nucleate, (c) the voids start to grow, (d) strain localize between the voids, (e) the region between the voids starts to neck, and (f) the voids coalesce and the material fractures. Adopted from [15].

2.7 The Gurson-Tvergaard-Needleman-model

In 1977, Gurson developed a porous plasticity model [6]. This model was later modified by Tvergaard and Needleman [7] [16] [17].The Gurson- Tvergaard- Needleman-model, or the GTN-model, is an isotropic yield function. The model contains the von Mises stress and models void growth and void coalescence. It is defined as:

$$\Phi(\sigma_{eq}, \sigma_h, f, \sigma_0) = \frac{\sigma_{eq}^2}{\sigma_y^2} + 2q_1 f \cosh\left(\frac{3\sigma_h}{2\sigma_y} q_2\right) - 1 - q_3 f^2 = 0 \tag{2.21}$$

where σ_{eq} is the equivalent von Mises stress, σ_h is the hydrostatic stress, f is the void volume fraction, and σ_y is the yield stress. When $f = 0$, the material has no voids, and the yield function is reduced to the von Mises yield criterion. For f larger than the critical void volume fraction, f_c, void coalescence is modelled with an accelerated void growth. The void volume fraction is then presented as $f^*(f)$. As defined by [7]:

$$f^*(f) = \begin{cases} f & \text{if } f \leq f_c \\ f_c + \kappa(f - f_c) & \text{if } f_c < f < f_F \end{cases} \tag{2.22}$$

where f_F is the void volume fraction at failure and κ is defined as:

$$\kappa = \frac{f_K - f_c}{f_F - f_c} \tag{2.23}$$

and f_K is defined as:

$$f_K = \frac{q_1 + \sqrt{q_1^2 - q_3}}{q_3} \tag{2.24}$$

where f_K is the value of f^* when a macroscopic crack forms, i.e. $f^*(f_F) = f_K$. f_F is as mentioned the void volume fraction at failure. At this point, the material has lost all its stress carrying capacity [7]. The GTN- model as defined above, is the general definition as defined by Tvergaard [16]. In Tvergaard and Needleman [7], q_3 is defined as:

$$q_3 = q_1^2 \tag{2.25}$$

This relation will be used for the analysis in this thesis. When this is applied, equation 2.24 reduces to:

$$f_K = \frac{q_1 + \sqrt{q_1^2 - q_1^2}}{q_1^2} = \frac{1}{q_1} \tag{2.26}$$

Typical values are $q_1 = 1.5$ and $q_2 = 1$[17]. For $q_1 = 1.5$, the maximum void volume fraction at failure is then:

$$f_K = \frac{1}{1.5} = \frac{2}{3} \tag{2.27}$$

The void volume fraction changes through $\dot{f}$:

$$\dot{f} = \dot{f}_{gr} + \dot{f}_{nucl} \tag{2.28}$$

where $\dot{f}_{gr}$ and $\dot{f}_{nucl}$ is change due to void growth and void nucleation respectively. Void nucleation will not be used, $\dot{f}$ then reduces to:

$$\dot{f} = \dot{f}_{gr} = (1 - f)\dot{\varepsilon}_p \tag{2.29}$$

where $\dot{\varepsilon}_p$ is the volumetric plastic strain rate defined as:

$$\dot{\varepsilon}_p = \dot{\varepsilon}^p_{kk} \tag{2.30}$$

The plastic strain rate, $\dot{\varepsilon}^p_{ij}$ is defined through the flow rule:

$$\dot{\varepsilon}^p_{ij} = \dot{\lambda}\frac{\partial \Phi}{\partial \sigma_{ij}} \tag{2.31}$$

where $\dot{\lambda}$ is the plastic multiplier.

2.8 Ageing and quenching

Altering the microstructure of an alloy may be necessary to get the desired mechanical properties. As mentioned in Section 2.5, there are four different fracture mechanisms observed in a Kahn tear test. The presence of each fracture mechanism can be influenced by ageing and quenching. Through these treatments, the microstructure of the alloy is altered, resulting in different mechanical properties. There are different forms and combinations of ageing and quenching. One of these is precipitation strengthening, and is performed through the following steps:

1. Solutionizing. The alloy is heated to a temperature where the alloying elements are dissolved. This temperature is held until a homogeneous solution is achieved.
2. Quenching. The state achieved during solutionizing is not a stable state at room temperature. Rapid quenching is performed to induce a supersaturated solid solution. It may be detrimental that the temperature is lowered quickly enough. For low quench rates, solutes can precipitate, which can give unwanted material properties. Vacancies in the structure can also be depleted, and vacancies are crucial for nucleation of precipitates [18]. In general, alloys with a high content of alloying elements are more sensitive to quenching, because the possibility of precipitates forming is higher [18].
3. Ageing. Natural ageing is simply that the microstructure changes over time at room temperature. Artificial ageing is when the material is kept at an elevated temperature for a given period. The supersaturated state developed achieved in the solutionizing step is now allowed to change. The temperature and duration of the ageing treatment depend on which precipitates is desired, and how large they should be.

2.8.1 Mechanical properties depending on heat treatment

As mentioned above, ageing and quenching are performed to alter the mechanical properties. In Figure 2.4, it can be seen how the yield strength changes during ageing when different quenching rates are performed. It can be seen that there is a peak in yield strength. This is commonly referred to as the peak ageing state. The three different lines plotted in figure 2.4 are for three different quenching rates. It can be seen that both ageing and quenching influences the yield strength. The strain hardening rate has the opposite relationship to ageing compared to yield strength. In an under-aged state, the microstructure is still in a partially supersaturated state resulting from the solutionizing of the alloy and shearable Guinier- Preston zones. These zones are the first precipitates to form during ageing [19], and dissolves as ageing continues [2]. At peak ageing, the strain hardening rate is at its lowest. This is due to a low solute content, and there are shearable precipitates present [2].

2.9 Precipitate free zones

A precipitate free zone is a zone within the grain that has no precipitates and they are located along the grain boundaries. The precipitate free zones are softer compared to the rest

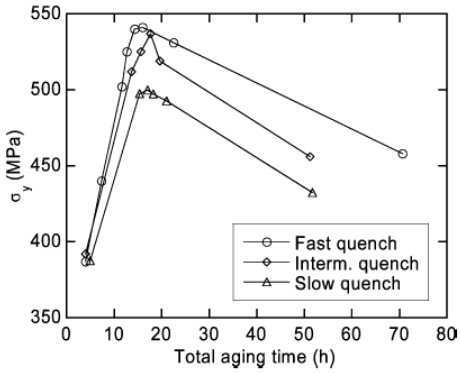

Figure 2.4: Yield strength as a result of different quenching rates and ageing times for AA7050. Adopted from Dumont et al. [2].

of the microstructure, and plastic strains tend to localize in these zones [18]. In aluminium, PFZs are always present in some level, but they are not always a problem. Knowing how these zones occur, and understanding how the PFZ affects the fracture properties is crucial.

2.9.1 Origin of the PFZ

The origin of PFZs is a complex subject. Research has shown that the PFZ originates from two main mechanisms; vacancy depletion and solute depletion [20]. The first case occurs when vacancies are depleted along the grain boundary. It appears to be a critical level of vacancies needed for precipitates to form. If the vacancy concentration is below this value, no precipitates forms, and a PFZ is formed. Vacancy depletion can as mentioned in Section 2.8 be caused by a too slow quench after solutionizing, this can also by the case of solute depletion. These phenomena are very complex and will be further explained below.

Unwin et al. [5] examined the origin of the PFZ. They worked with two different alloys, one from the Al-Zn-Mg-family (7xxx-series), and one from the Al-Cu-family (2xxx-series). The specimens they worked with were $150\mu m$ thick. The research was started by solutionizing the alloys, then quenching them in water at $T_1 = 22°C$, and finally ageing them at $T_2 = 180°C$. The PFZ present in the different microstructures for this treatment was $0.5 - 0.7\mu m$ wide, and there were also observed homogeneously distributed precipitates inside the grains. Next, a disturbance in the quenching was performed to see how that would affect the PFZ. The disturbance was done by cooling the specimen at $T_1' = 180°C$ before quenching it. This turned out to have a large impact on the PFZ-width. The value of T_1' and T_2 were both kept above $T_{G.P.}$, which is the upper temperature at which GP-zones form, in order to ensure that no GP-zones were created. This is important because of vacancies and GP-zones interact and that would make the interpretation of the results more difficult [5]. The interruption at T_1' was held for 3 sec and 10 sec. The PFZ-width increased rapidly after less than 10 seconds at T_1'. Regarding the vacancy depletion, they found that the grain boundary worked as a sink for vacancies during the quenching under

certain circumstances. Many precipitates need vacancies to nucleate. For some alloys, if aged below the GP-solvus, the vacancy depleted areas may get GP-zones as they do not need vacancies to nucleate [13].

The PFZ is as mentioned located along the grain boundary, and therefore a fracture located here will be an intergranular fracture. In work done by Dumont et al. [2] it was found that the proportion of intergranular fracture was maximum in the peak ageing condition. In the over-aged state, the overall toughness is lowered resulting in a more similar yield strength to that of the PFZ. In this way, the effect of the PFZ was lowered due to a more similar yield strength for the rest of the microstructure. The influence of the PFZ is lowered for this case because it has properties similar to that of the grain interior.

The presence of the PFZ is dependent on the ageing and quenching. Quenching has an influence on the amount of coarse precipitates able to inhibit the grain boundaries [2]. The extrusion will influence the anisotropy of the alloy, and this gives different preferential directions for fracture along the PFZ [2]. This means that the fracture toughness is expected to be different in different load directions. Both the extruded direction and the transversal direction will be examined in Chapter 3 for the Kahn tear test to see how the material orientation influences the result.

Chapter 3

Experimental study

In this experimental study, three different tests will be conducted. They are the round smooth tensile test, the round v-notch tensile test, and the Kahn tear test. For the Kahn test, the alloys AA6060, AA6082.25 and AA6082.50 will be used. AA6082.50 will not be used for the v-notch- and smooth-tensile test. The smooth tensile test will be used to find the hardening parameters from the Voce- rule and to calibrate the material model for the numerical study, as explained in Section 2.1.3. The v-notch tensile test is useful because it has similar triaxiality ratios to the Kahn test. It is also less computationally expensive to simulate compared to the Kahn tear test and is therefore used to calibrate the fracture model. The Kahn tear test is the primary test in this thesis and will be used to study the effect of the PFZ. At first, an introduction to the alloys of interest is given, followed by an introduction to material orientation. Next, an explanation of the heat treatment used to prepare the tests is given. Lastly, the experimental setups and results are presented.

3.1 Alloys of interest

All of the alloys used in this thesis are members of the 6xxx-family. The basis of this family is the presence of magnesium and silicon. This family consists of medium strength structural alloys with a good weldability, good resistance to corrosion and is immune to stress- corrosion cracking [13]. They are frequently extruded, and some are also available as plates and sheets. When mixing magnesium and silicon into aluminium alloys, the alloys can be divided into two groups. The first is to add magnesium and silicon in what is called a ”balanced” manner to create quasi- binary Al-Mg_2Si- alloys. For this case the ratio Mg to Si is $1.73 : 1$. The other group is to add an excess of silicon to what is needed to form the first group [13]. The first case mentioned above contains between 0.8% and 1.2% magnesium and silicon. As seen in Table 3.1 this is the case for all alloys of interest. These alloys have the advantage that they can be quenched directly from the extrusion press without the need for solution treatment afterwards [13].

Three different aluminium alloys will be used in this thesis, and they are: AA6060,

Table 3.1: Chemical composition of the different alloys used. The composition is in wt% and the values are adopted from Frodal et al. [21].

Alloy	Fe	Si	Mg	Mn	Cr	Cu	Zn	Ti	Al
AA6060	0.193	0.422	0.468	0.015	0.000	0.002	0.005	0.008	Bal.
AA6082.25	0.180	0.880	0.600	0.530	0.150	0.020	0.005	0.011	Bal.
AA6082.50	0.200	1.020	0.670	0.540	0.001	0.003	0.005	0.010	Bal.

AA6082.25, and AA6082.50. The two latter are quite similar, the chromium content is the main difference, which is 150 times higher in AA6082.25. Table 3.1 shows the complete composition of the three materials. The alloying elements present are iron, silicon, magnesium, manganese, chromium, copper, zinc, and titanium. They are present in some form in all the alloys used, except there is no chromium present in AA6060.

The microstructure of the three alloys were examined by Frodal et al. [21]. A recrystallized microstructure with equiaxed grains was found for AA6060. The grain size was about $60 - 70\mu m$. AA6082.25 did not recrystallize and had a typical fibrous structure with fibres several millimetres long in the extruded direction, approximately $10\mu m$ in the normal direction and $150\mu m$ in the transversal direction. AA6082.50 is recrystallized, but has elongated grains like AA6082.25. The grains are much wider for AA6082.50, about $300 - 400\mu m$. The grain structures can be seen in Figure 3.1.

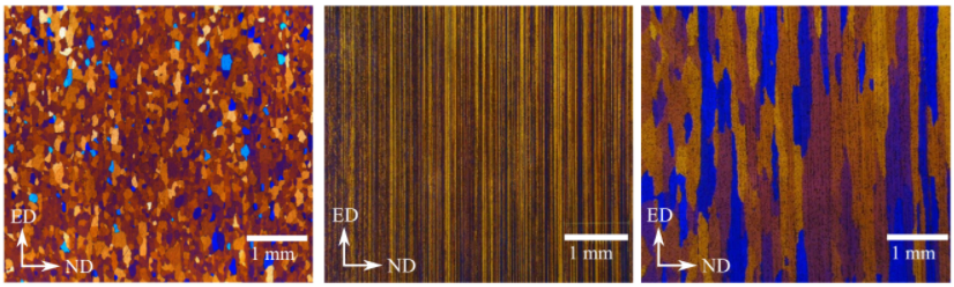

Figure 3.1: Grain structure of the different alloys: (a) AA6060, (b) AA6082.25, (c) AA6082.50. Figure adopted from Frodal et al. [21].

3.2 Material orientation

The test specimens used for the experiments are machined out of a flat extruded profile. The effect of different loading orientation will be examined by using two orientations. The first is when the length of the specimen and the loading axis is oriented along the extrusion direction of the profile and is denoted ED. When taken out 90° with respect to the extrusion direction it is denoted TD for transverse direction. This is the second orientation. Figure 3.2 shows the difference between the two orientations. The Kahn tear

tests will be conducted in both TD and ED, but the v-notch and smooth tensile tests will only be conducted in TD.

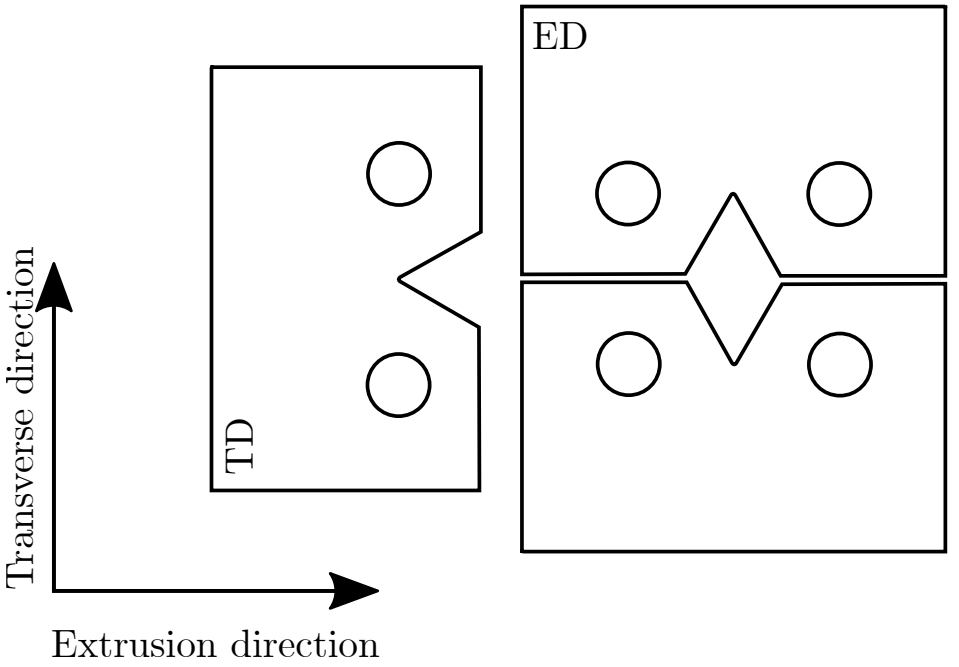

Figure 3.2: Orientations of the Kahn test specimens machined from the extruded profile.

3.3 Heat treatment

As mentioned in Section 2.8, heat treatment is used to alter the mechanical properties of the material. The heat treatments used in this study can be seen in Figure 3.3. Two different sequences were used, with the same ageing period and two different quenching rates. The ageing was done to peak strength, T6 temper. The ageing period giving peak strength for the water-quenched specimens was applied for the air-cooled specimens as well. It is not certain that this gives peak strength for the air-cooled specimens. As a result, they may be a bit under- or over-aged. The quenching methods are air-cooled, denoted AC, and water-quenched at room temperature, denoted WQ.

Both treatments began with solutionizing at $540°C$ for 15 minutes. Then the specimens were either water-quenched to room temperature immediately or air-cooled to $50°C$ and then water-quenched to room temperature. After 15 minutes at room temperature, the specimens were aged at $185°C$ for 5 hours. The solutionizing was done in a solution of molten salt, and the ageing in an oil bath. The Kahn tear test specimens were linked together in groups of six when treated, as seen in Figure 3.4. As was the v-notch and the smooth tensile tests.

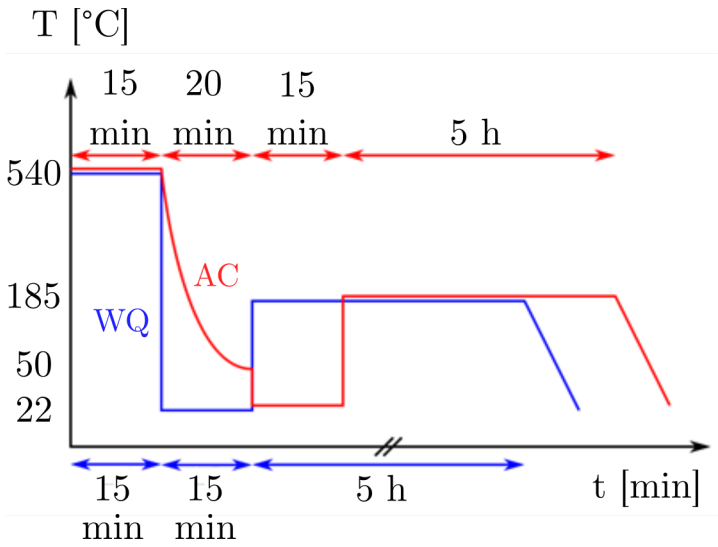

Figure 3.3: Heat treatment curve for the experimental study. Courtesy of Emil Christiansen.

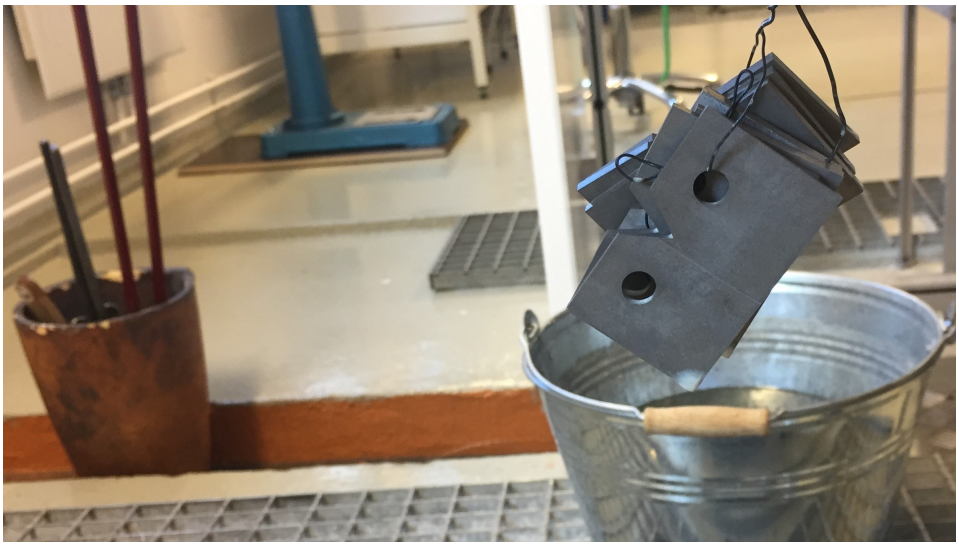

Figure 3.4: Arrangement of Kahn tear test specimens during heat treatment.

3.4 Smooth and v-notch round tensile tests

The smooth and v-notched round tensile tests are mainly included to calibrate the material model to simulate the Kahn tear test in Chapter 4. The geometry of each test specimen can

be seen in Figure 3.5. The alloys used were AA6060 and AA6082.25. Both these alloys were tested both air-cooled and water-quenched, resulting in four configurations.

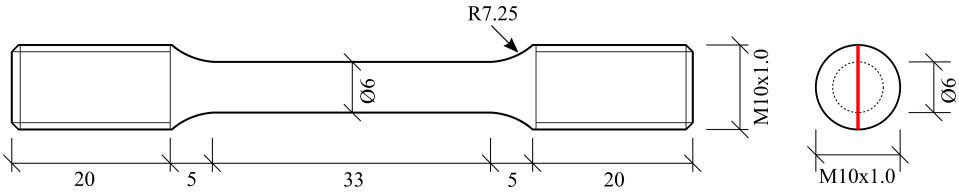

(a) Smooth tensile geometry.

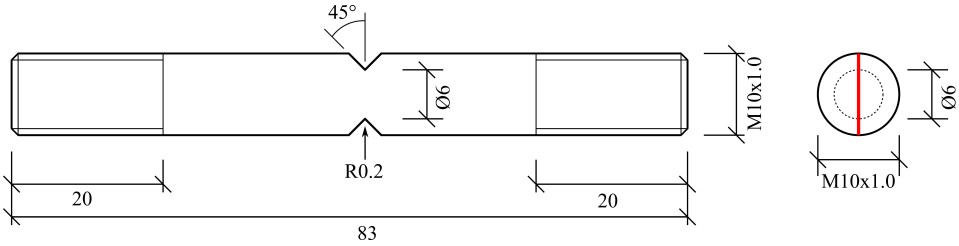

(b) V-notch geometry.

Figure 3.5: Geometry with dimensions for the smooth and v-notched round tensile tests. The red line indicates the thickness direction from the extruded profile. Courtesy of Bjørn Håkon Frodal.

3.4.1 Experimental setup

The tests were conducted in the laboratory at the Department of Structural Engineering. The loading machine used was Zwick Roell Z030 with a 30kN load cell. The crosshead velocity applied was 1mm/min for the smooth tensile test and 0.12 mm/min for the v-notch tensile test. An AEROEL XLS 13XY laser micrometre was used to monitor the diameter. With two lasers oriented 90° to each other, the diameter in ED and ND (normal direction/thickness direction of extruded profile) was measured. The red line on the test specimens was used to measure the correct directions. These measures were used to establish the true stress and true strain, as explained in Section 2.1.3. The lasers were continuously moved to find the diameter at the narrowest point. This resulted in some noise in the data. This was filtered out in MATLAB by running through the calculated area vector and always taking the minimum value of two neighbouring numbers. This way, a sudden jump in the area vector was filtered out. The setup with the loading machine and the laser is shown in Figure 3.7. Three repetitions were made for each configuration, with two heat treatments, and two different alloys, giving a total of:

$$N = 3 \text{ repetitions} * 2 \text{ heat treatments} * 2 \text{ alloys} = 12 \text{ tests} \tag{3.1}$$

for the smooth and the v-notch tensile test. Samples of the test specimens can be seen in Figure 3.6.

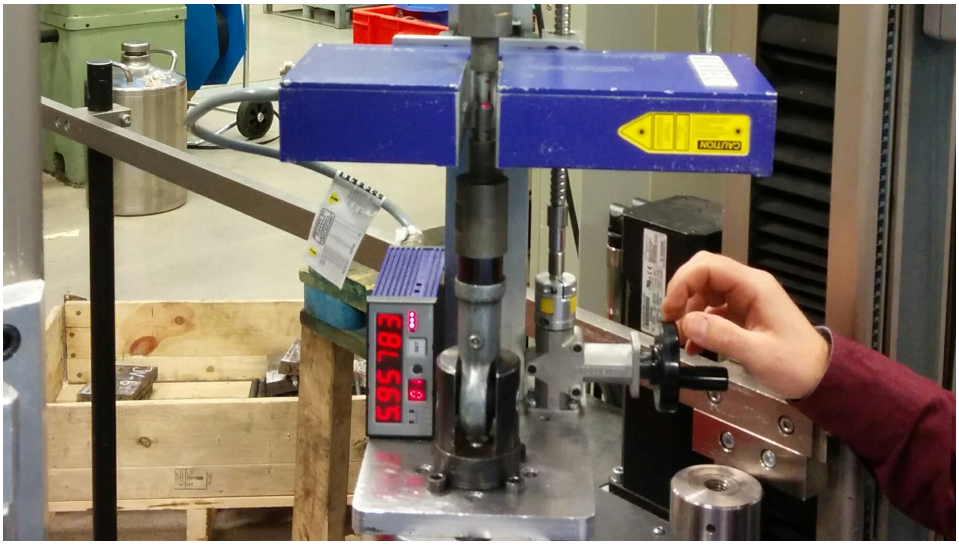

Figure 3.7: Test setup with loading machine and lasers. Courtesy of Bjørn Håkon Frodal.

(a) Smooth tensile specimen. **(b)** V-notch tensile specimen.

Figure 3.6: Smooth and v-notch tensile specimens. Courtesy of Bjørn Håkon Frodal.

3.4.2 Experimental results

From the tests, data containing the resulting force, F, and the diameters D_x and D_y were used to find the true stress and logarithmic strain using the method explained in Section 2.1.3. The true stress- logarithmic strain plots can be seen in Figure 3.8. The different configurations are named by first putting the alloy followed by a to letter code indicating heat treatment. The effect of the cooling method is strongest for AA6082.25. The water-quenched AA6082.25 has approximately three times as high yield strength compared to its air-cooled counterpart. For AA6060, this difference is only 35%. The yield strength was found by curve fitting the stress curve to the Voce-rule. This was introduced in Section 2.1.3 and will be further explained in Chapter 4. The maximum stress with accompanying strain can be seen in Table 3.2 and Table 3.3 for the smooth and v-notch tensile test respectively. The scatter between parallel tests is small for AA6060. The true stress-logarithmic strain curves for both the smooth and the v-notch tensile tests have quite similar shape for both quenching rates for AA6060, but the yield stress is lower for the air-cooled specimens. For AA6082.25 the maximum stress is significantly higher for the water-quenched curves compared to the air-cooled, for both the smooth tensile tests and the v-notch tests. The fracture strain for the water-quenched v-notch tensile test is less than half of the air-cooled

counterpart. It can be seen from Figure 3.8b that the strain hardening of the air-cooled AA6082.25 is much higher at the beginning compared to the water-quenched AA6082.25.

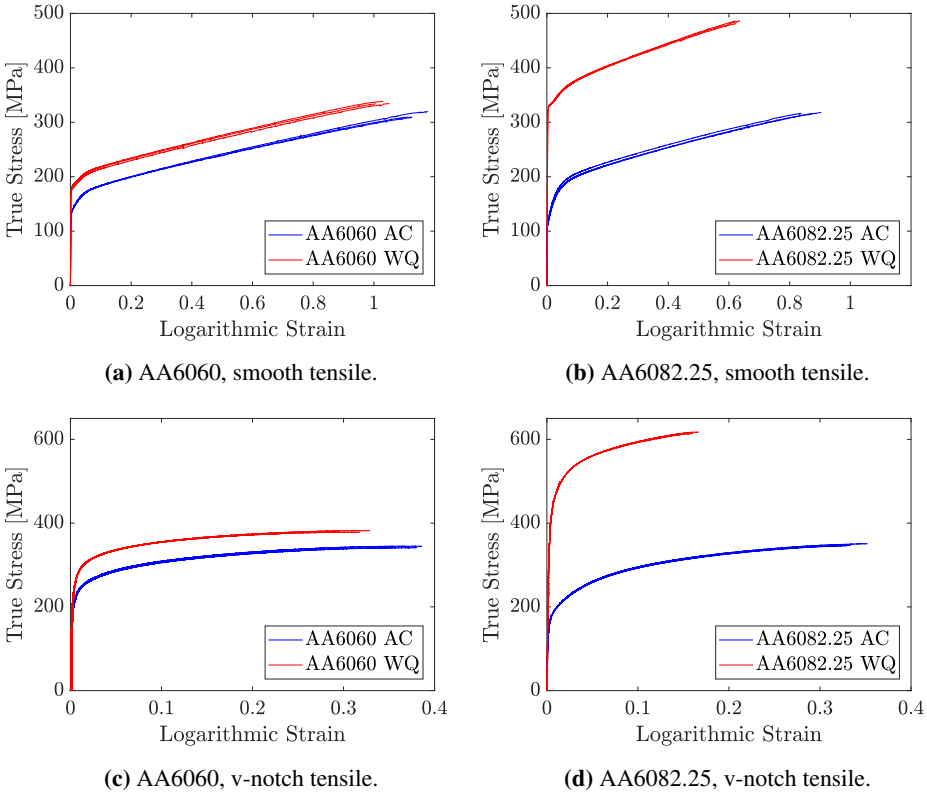

(a) AA6060, smooth tensile.

(b) AA6082.25, smooth tensile.

(c) AA6060, v-notch tensile.

(d) AA6082.25, v-notch tensile.

Figure 3.8: True stress vs. logarithmic strain for the smooth tensile test and v-notch tensile test. Plotted until maximum true stress.

Table 3.2: Maximum stress and accompanying strain for the smooth tensile tests.

Configuration	Logarithmic strain at maximum true stress	Maximum true stress [MPa]
AA6060 AC	1.14	312.70
AA6060 WQ	1.03	335.84
AA6082.25 AC	0.87	316.91
AA6082.25 WQ	0.63	484.54

Table 3.3: Maximum stress and accompanying strain for the v-notch tests.

Configuration	Logarithmic strain at maximum true stress	Maximum true stress [MPa]
AA6060 AC	0.37	342.82
AA6060 WQ	0.31	381.00
AA6082.25 AC	0.34	348.13
AA6082.25 WQ	0.16	614.71

3.5 The Kahn tear test

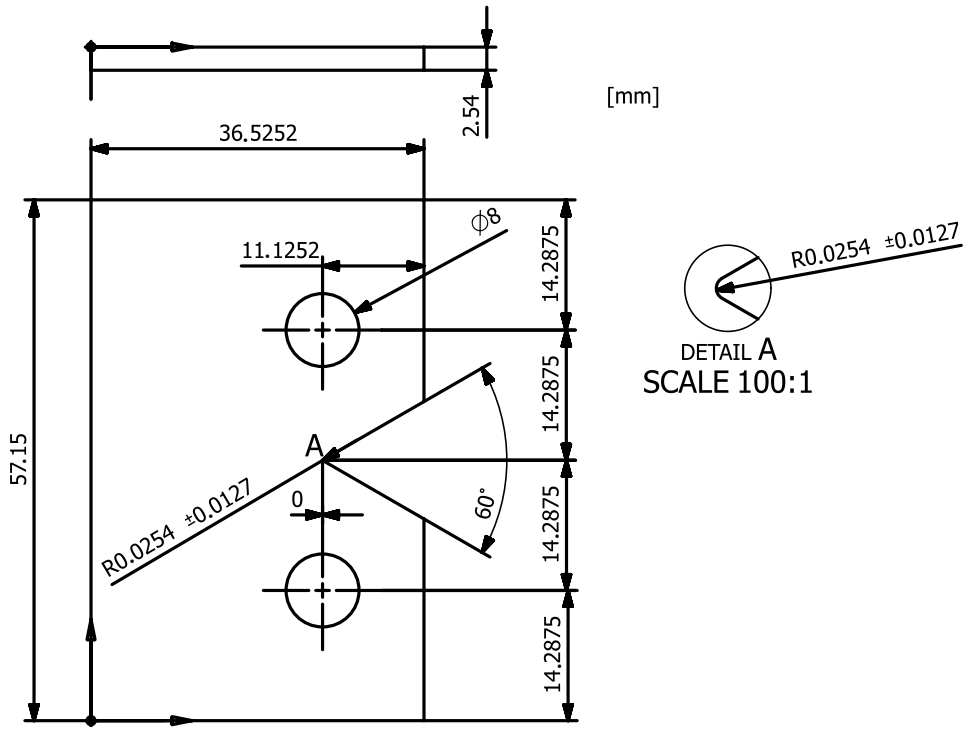

Figure 3.9: Test specimen geometry of the Kahn tear test.

3.5.1 Test specimen

The test specimen is made according to a type 2 specimen in the B 871-01 standard [12], except the notch root radius. The notch root radius could not be machined to the given value. The radius was supposed to be $2.54*10^{-2}$ mm, but the smallest radius available for machining was 0.2 mm. Since this is a comparative study, and the intention is not to establish standard values for the UIE or the UPE, the oversized notch radius is satisfactory. The geometry can be seen in Figure 3.9.

The test specimens were made for different alloys, orientations, and heat treatments. For the Kahn test, there was three different alloys, two different orientations, two different quenching methods and three repetitions of each specimen. This gives a total of:

$$N = 3 \text{ repetitions} * 2 \text{ heat treatments} * 3 \text{ alloys} * 2 \text{ orientations} = 36 \text{ tests} \tag{3.2}$$

The 36 test specimens were all measured carefully. The thickness was measured at three different points for each specimen. The average thickness, length, and width are 2.567 mm, 57.20 mm, and 36.56 mm respectively. These values deviate little from the given geometry. The standard deviation for the dimensions was 0.008 mm, 0.027 mm, and 0.016 mm respectively.

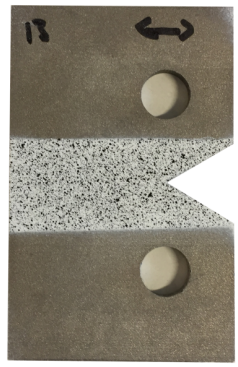

Figure 3.10: Kahn test specimen with speckle for Digital image correlation analysis.

3.5.2 Experimental setup

The tests were conducted in the laboratory at the Department of Structural Engineering. The test machine used was an Instron 5985 with a 250 KN load cell. Load and cross-head displacement were recorded for the experiment. Also, speckle painting was applied to the test specimen and video recorded while loading. This will be used for digital image correlation (DIC) and will be further explained in Section 4.5.1. The test setup can be seen in Figure 3.11.

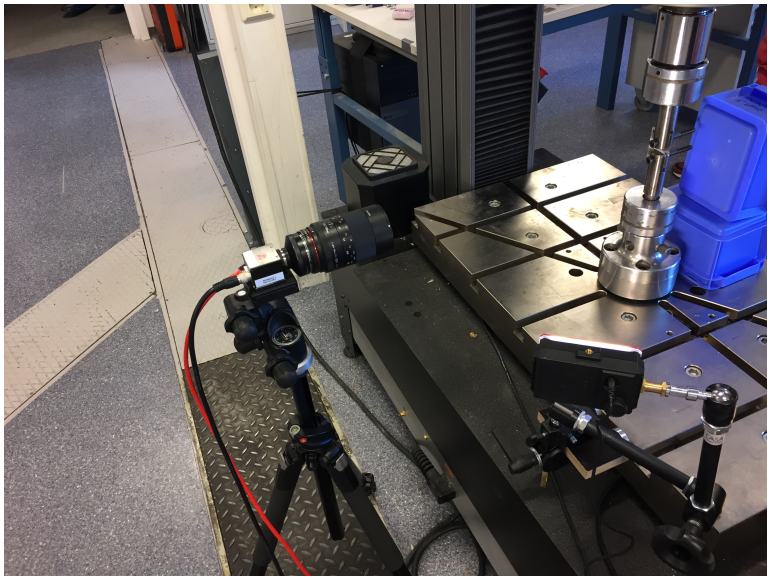

Figure 3.11: Test setup used for the Kahn tear tests. The blue boxes seen in the picture were used as background for the pictures taken by the camera to the left to ensure better contrast. An extra light source was also used, seen in the bottom right corner.

The test specimen was mounted in the machine using hardened bolts and spacers, holding the specimen in centre of the load axis. The spacers were 3D- printed to fit between the clevises and test specimen. The tests were stopped when the resulting force was approximately 2% of the maximum force. The maximum force for the different specimen varied, and so did the time elapsed before this 2% mark was reached. As a result, each test lasted from around five to twenty minutes.

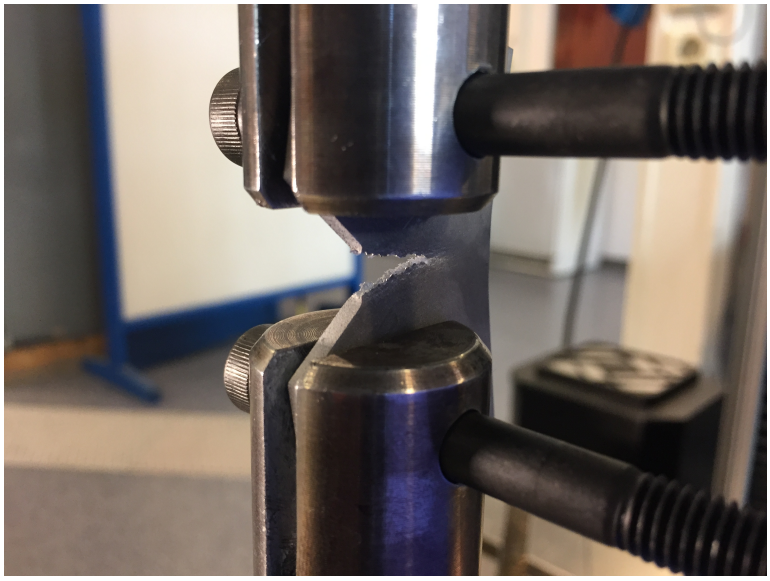

Figure 3.12: A Kahn specimen being loaded and failing by tearing.

3.5.3 Experimental results

A total of 37 tests were completed. The first test was a dummy test, taken from one of the sides that were machined away to machine the correct thickness of the test specimens. All the test specimens, except the dummy test, are listed in Table 3.4 showing the alloy, heat-treatment, material orientation, UPE for each specimen and average UPE for each configuration. A specimen being loaded can be seen in Figure 3.12. After the dummy test, everything worked, except for the crosshead velocity, that was too low. In the first test, it was set to 0.25 mm/min because it was concluded after private communication [22] that this would be an appropriate value. However, for this velocity, the test took 1 hr. The new crosshead velocity was adjusted to 1 mm/min. This velocity was also found from private communication [23]. At this velocity, the first actual test took ca. 20 min to complete. This was acceptable, and the crosshead velocity was then kept at 1 mm/min. Some of the less ductile test specimens, like the water-quenched AA6082.50, only took six min to complete with a crosshead velocity of 1 mm/min. Instead of adjusting the crosshead velocity, the number of frames per second taken by the camera was adjusted to acquire more information from the DIC-analysis.

Table 3.4: Alloy, quench, orientation and UPE for the Kahn tear tests.

Test No.	Alloy	Quench	Orientation	UPE [kJ/m^2]	Average UPE [kJ/m^2]
1	AA6060	AC	TD	260	
2	AA6060	AC	TD	244	
3	AA6060	AC	TD	248	251
4	AA6060	AC	ED	236	
5	AA6060	AC	ED	231	
6	AA6060	AC	ED	236	234
7	AA6060	WQ	TD	271	
8	AA6060	WQ	TD	275	
9	AA6060	WQ	TD	277	274
10	AA6060	WQ	ED	253	
11	AA6060	WQ	ED	263	
12	AA6060	WQ	ED	249	255
13	AA6082.25	AC	TD	220	
14	AA6082.25	AC	TD	213	
15	AA6082.25	AC	TD	221	218
16	AA6082.25	AC	ED	212	
17	AA6082.25	AC	ED	217	
18	AA6082.25	AC	ED	215	215
19	AA6082.25	WQ	TD	110	
20	AA6082.25	WQ	TD	104	
21	AA6082.25	WQ	TD	141	118
22	AA6082.25	WQ	ED	133	
23	AA6082.25	WQ	ED	154	
24	AA6082.25	WQ	ED	149	145
25	AA6082.50	AC	TD	141	
26	AA6082.50	AC	TD	142	
27	AA6082.50	AC	TD	177	154
28	AA6082.50	AC	ED	240	
29	AA6082.50	AC	ED	278	
30	AA6082.50	AC	ED	218	245
31	AA6082.50	WQ	TD	106	
32	AA6082.50	WQ	TD	969	
33	AA6082.50	WQ	TD	101	102
34	AA6082.50	WQ	ED	302	
35	AA6082.50	WQ	ED	267	
36	AA6082.50	WQ	ED	260	276

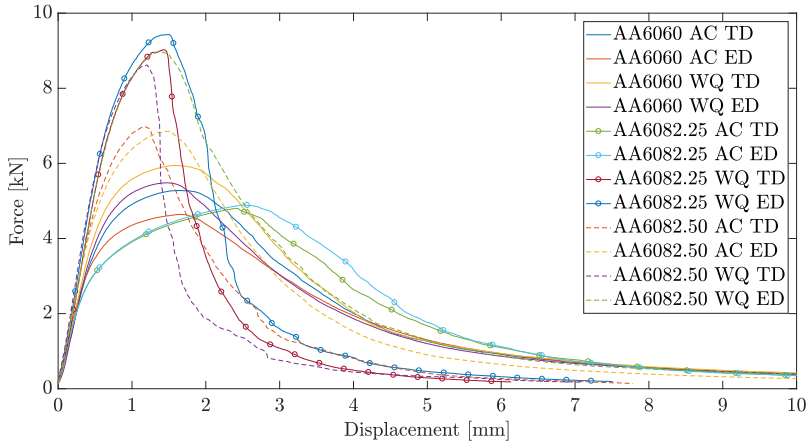

Figure 3.13: Force-displacement curves, one representative test of each configuration. The forces and the displacements are the ones measured by the test machine.

It became clear that the different alloys with the different specimen directions and heat treatments play a central role in the force-displacement curves. Plots of the force-displacement curves for each configuration can be seen in Figure 3.13. The different configurations are named like the v-notch and smooth tensile tests, except there is an additional two letter code at the end indicating material orientation. AA6060 showed a more anisotropic behaviour than AA6082.25 and AA6082.25. AA6082.25 exhibited the most isotropic properties. All the water-quenched specimens had higher maximum force than their air-cooled counterparts. This is consistent with the observed fact that a faster quench gives a higher yield strength.

In Figure 3.14 - Figure 3.16, two force- displacement series are plotted in pairs to compare the influence of either cooling method or orientation. Each configuration is related to two other configurations, with either the same cooling method or the same orientation. The different series are therefore plotted in two different plots.

When comparing the same cooling method and different orientations, the role of orientation varies quite a lot. For the air-cooled and water-quenched AA6060, air-cooled in Figure 3.14a and water-quenched in Figure 3.14b, the transverse direction has a higher maximum force than the extrusion direction. The maximum force is on average 13.4% higher for the transverse direction when the specimen is air-cooled, and 8.2% higher when water-quenched. For the same configuration with AA6082.25, as seen in Figure 3.15a and Figure 3.15b respectively, it is almost as the direction does not matter at all. The difference is also opposite to that of AA6060, the extruded direction has the highest maximum force, but by less than 3% higher in both cases. In the same plots with AA6082.50, seen in Figure 3.16a and Figure 3.16b, the differences in maximum force is also quite small. One observation that is interesting for AA6082.50 is that the difference in maximum force is quite small, but they are shifted relative to each other for both the air-cooled and the

water-quenched case. The curves also decrease at a slower rate for the extruded direction. With a shifted peak and a slower decrease, the extruded direction has a much larger UIE and UPE in both air-cooled and water-quenched.

When comparing different cooling methods and the same orientation, the differences within one plot is bigger than when comparing different orientations. For AA6060, the difference in maximum force between an air-cooled and a water-quenched specimen is the smallest of the alloys. As seen in Figure 3.14c and Figure 3.14d, one can see that the difference in maximum force is not more than around 10% for both directions. When looking at the same Figures for AA6082.25, Figure 3.15c and 3.15d, the difference between the cooling methods is much more substantial. The water-quenched specimens have a maximum force almost two times larger than the air-cooled specimens in both directions. For AA6082.50 the difference is not as big, around 25% larger value for the water-quenched specimen in the transverse direction, and 30% for the water-quenched in the extruded direction.

In Figure 3.17a, 3.17b and 3.18, bar charts can be seen showing the average UIE, UPE and maximum force, respectively, for all the different configurations. The red bars are AA6060, the blue ones AA6082.25, and the yellow ones AA6082.50. For AA6060 there is a positive correlation between maximum force and UPE. AA6060 AC ED has the lowest UPE and maximum force, and AA6060 WQ TD has the highest maximum force and UPE. This correlation is not seen for the UIE. For the other alloys, there is no positive correlation between UPE and maximum force. The air-cooled AA6082.25 samples have a lower maximum force than the water-quenched ones. In contrast, the air-cooled specimens of AA6082.25 have a higher UPE than their water-quenched counterparts. AA6082.50 shows interesting result. If ordering the test specimens related to maximum force, AA6082.50 can be arranged based on heat treatment. Considering the UPE however, they should be arranged based on orientation.

Table 3.5 shows the average values of the UIE, UPE and maximum force of the water-quenched specimens are divided by the same values of their air-cooled counterarts. The force-ratio is always larger than one. That is not the case for the UPE-ratio. An interesting aspect with these ratios is seen when comparing the plots of the configurations that have both ratios larger than one (AA6082.50 in ED and both AA6060) with the ones that do not (AA6082.50 in TD and both AA6082.25). Looking at the curves after peak force for the first group, one can see that the air-cooled and water-quenched specimens follow each other quite well. The maximum force is what contributes the most to a different UPE between them. For the other group, the curves do not follow each other; the water-quenched specimens have curves that drop much faster. Even though the maximum force is much higher, the displacement at failure is much lower and the curve drops much faster after peak force, resulting in a lower UPE. Table 3.6 shows the same as Table 3.5 only with the ratios of the test specimens in TD divided by their counterpart in ED. In general the differences are smaller compared to Table 3.5. The largest differences between ED and TD is for AA6082.50

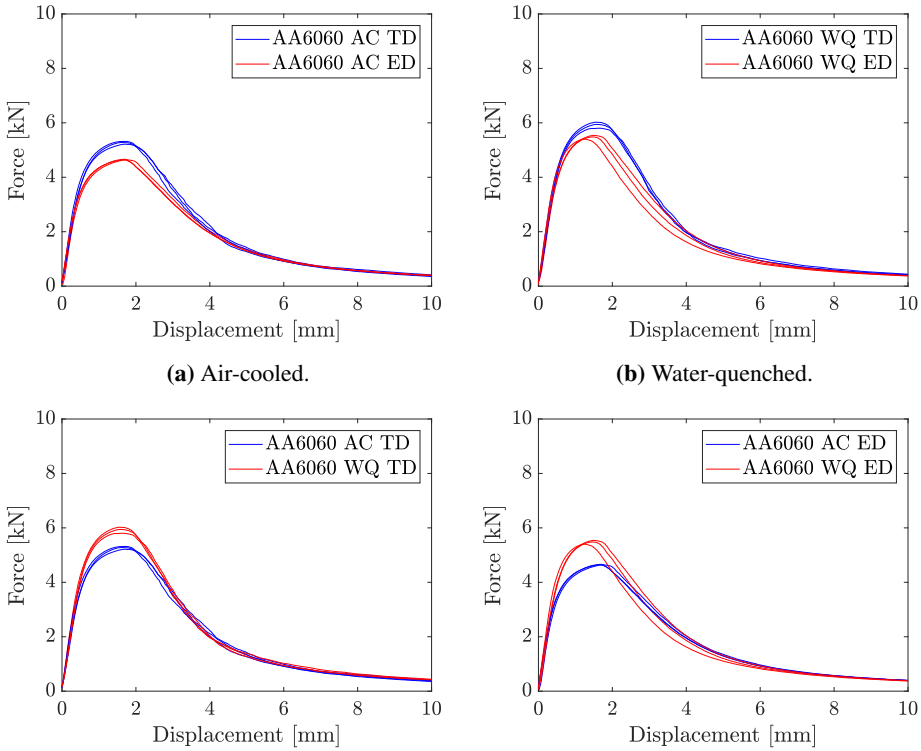

(a) Air-cooled.

(b) Water-quenched.

(c) Transverse direction.

(d) Extrusion direction.

Figure 3.14: Force-displacement curves for the test specimens conducted in AA6060. Each plot compares either orientation or heat treatment.

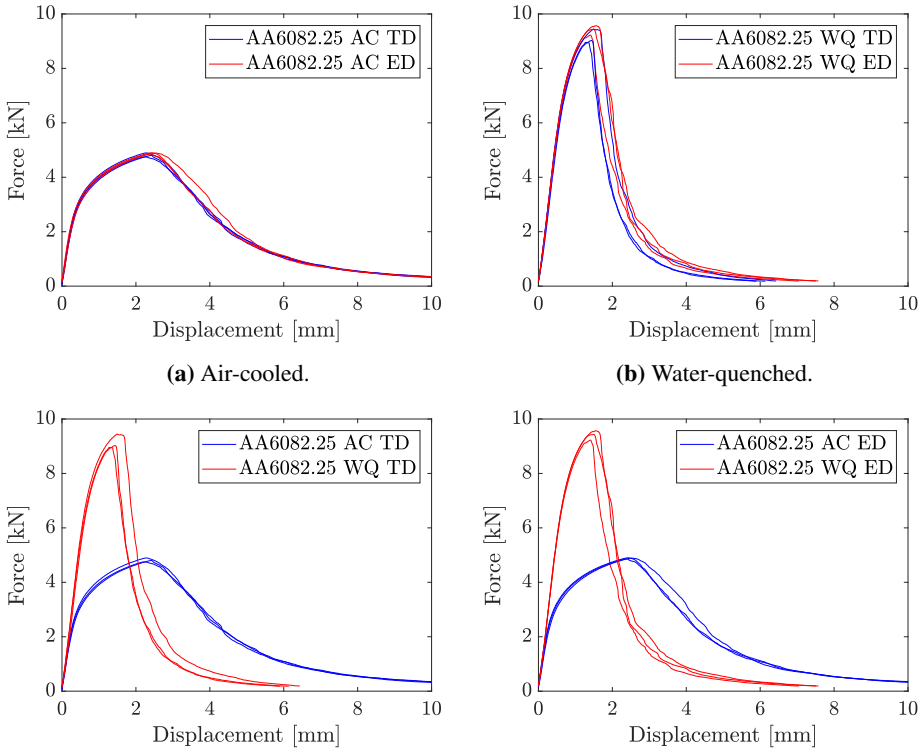

(a) Air-cooled.

(b) Water-quenched.

(c) Transverse direction.

(d) Extrusion direction.

Figure 3.15: Force-displacement curves for the test specimens conducted in AA6082.25. Each plot compares either orientation or heat treatment.

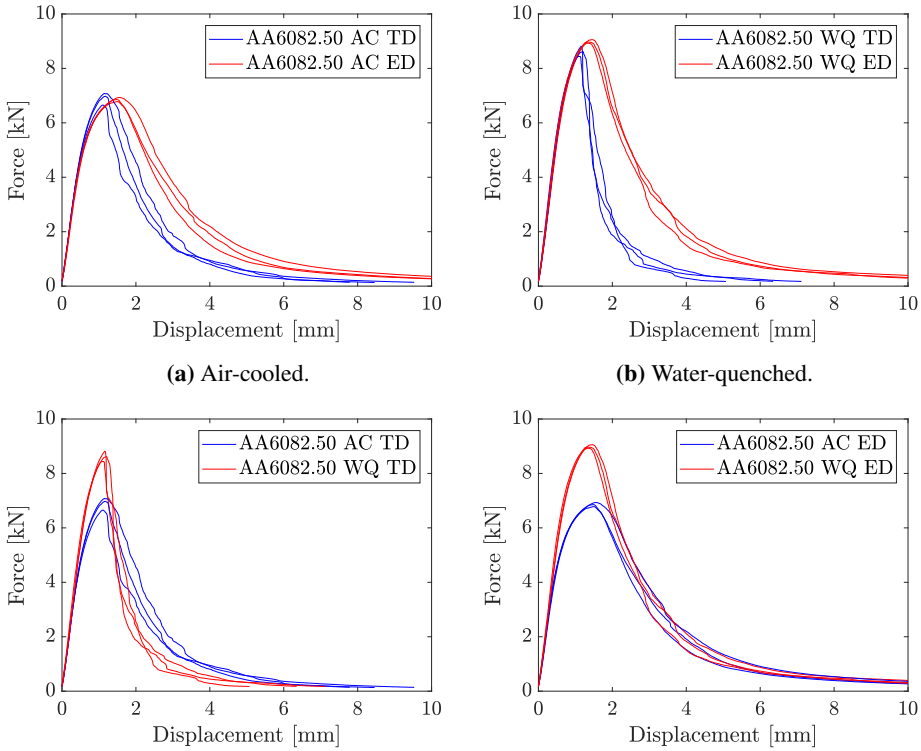

(a) Air-cooled.

(b) Water-quenched.

(c) Transverse direction.

(d) Extrusion direction.

Figure 3.16: Force-displacement curves for the test specimens conducted in AA6082.50. Each plot compares either orientation or heat treatment.

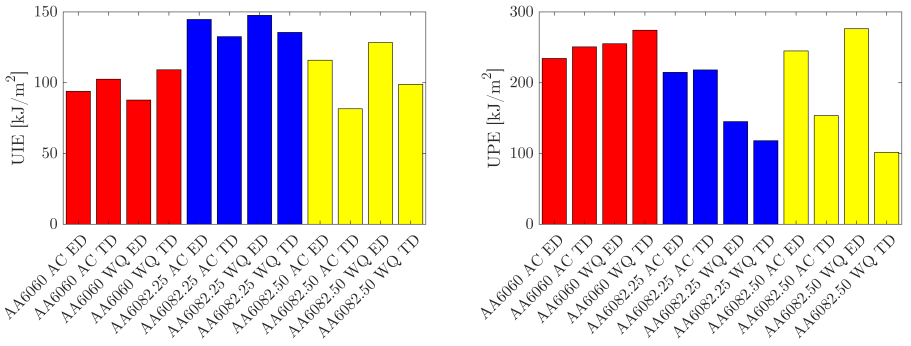

(a) UIE. **(b)** UPE.

Figure 3.17: Average UPE and UIE for each configuration.

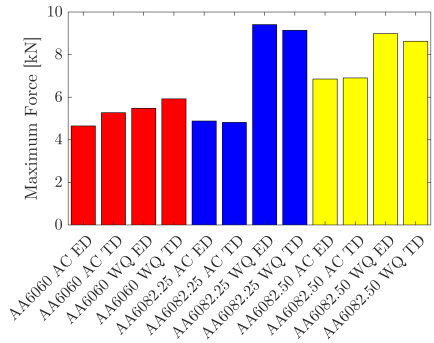

Figure 3.18: Average maximum force for each configuration.

Table 3.5: Ratios of the water-quenched test specimens divided by their air-cooled counterpart.

	UIE-ratio	UPE-ratio	F_{max}-ratio
6060WQTD/6060ACTD	1.06	1.09	1.12
6060WQED/6060ACED	0.93	1.09	1.18
6082.25WQTD/6082.25ACTD	1.02	0.54	1.90
6082.25WQED/6082.25ACED	1.02	0.68	1.93
6082.50WQTD/6082.50ACTD	1.21	0.66	1.25
6082.50WQED/6082.50ACED	1.11	1.13	1.31

Table 3.6: Ratios of the TD test specimens divided by their ED counterpart.

	UIE-ratio	UPE-ratio	F_{max}-ratio
6060ACTD/6060ACED	1.09	1.07	1.13
6060 WQTD/6060WQED	1.24	1.07	1.08
6082.25ACTD/6082.25 ACED	0.92	1.02	0.99
6082.25WQTD/6082.25WQED	0.92	0.81	0.97
6082.50ACTD/6082.50ACED	0.70	0.63	1.01
6082.50WQTD/6082.50WQED	0.77	0.37	0.96

When considering the work done by Unwin et al. [5], a faster quench gives a narrower PFZ. Based on a faster quench, the only value following the same pattern is the maximum force. Morgeneyer et al. [3] researched the effect of different quenching rates on AA6156 using the Kahn tear test. It was found that the air-cooled specimen had approximately half the UIE of the specimen quenched in water at a temperature of 20°C. These large difference in UIE were not observed in this experiment. The largest difference was between the water-quenched and air-cooled AA6082.50 specimens in TD which was 20% higher for the air-cooled specimens. This will be further explored in Section 3.8.

3.6 Investigation of fracture surfaces

The fracture surfaces of the Kahn tear test were examined by scanning electron microscopy (SEM). In Figure 3.19, the fracture surface of an air-cooled AA6060 specimen in the extrusion direction magnified by a factor of 20 can be seen. The extrusion direction is in this case normal to the plane. The fracture surfaces are referenced in relation to which test specimen they originate from. If a fracture surface is said to be in ED this means that the extrusion direction is normal to the plane, as indicated by the axis on the relevant figure. Some fracture surfaces are represented below. In the Appendix, an overview figure, a 100 times magnified figure and a 1000 times magnified figure can be found for each configuration. This figures can be useful for further exploring the fracture surfaces.

In Figure 3.19, there is a clear neck present. This fracture surface is also very homogeneous, as seen from Figure 3.21b. Some fracture surfaces exhibit different fracture modes, as the AA6082.50 WQ TD, seen in Figure 3.23c. A larger overview of this fracture surface can be seen in Figure 3.20. From this fracture surface, it can be seen that there is no obvious neck present.

In Figure 3.21, the fracture surfaces of all the configurations of AA6060 can be seen. The two figures to the left are in TD, and the ones on the right are in ED. The fracture surfaces in ED are more homogeneous compared to TD. Especially AA6060 AC TD seen in Figure 3.21a has smoother areas which may be intergranular fracture, i.e. that the fracture path is along the grain boundaries. This tendency is to some extent seen for the water-quenched counterpart in Figure 3.21c. In ED, the fracture surface is characterised by dimples, some containing particles, for both the air-cooled and the water-quenched. These dimples are clearly seen in the fracture surface of AA6060 AC ED, seen in Figure 3.21b. This feature is very dominating in this surface and indicates that the fracture mode is dominated by transgranular fracture. If comparing the fracture surfaces to the force- displacement plots in Figure 3.14a and Figure 3.14b, the TD specimens have curves that drop a bit faster. If this is due to a higher fraction of intergranular fracture is hard to say.

The fracture surfaces for AA6082.25 can be seen in Figure 3.22. The differences for these fracture surfaces became clearer when magnified by a factor of 1000. For AA6082.25, the direction does not play a significant role which was the case for AA6060. AA6082.25 AC TD has one wide zone which is almost white as seen in Figure 3.22a. It seems reasonable to assume that this is a intergranular fracture. This phenomenon is not present in the water-quenched counterpart seen in Figure 3.22c. AA6082.25 AC ED and AA6082.25 WQ ED, seen in Figure 3.22b and 3.22d respectively, are quite similar. It looks like there may be a larger fraction of intergranular fracture for the air-cooled compared to the water-quenched sample. The insignificant difference between the fracture surfaces when comparing different material orientations can be related to the force-displacement curves for AA6082.25 seen in Figure 3.15. AA6082.25 has the most isotropic behaviour of alloys investigated. However, AA6082.25 also has the biggest difference when it comes to heat-treatment. This large difference in strength seems to have only minor influence for the fracture surfaces.

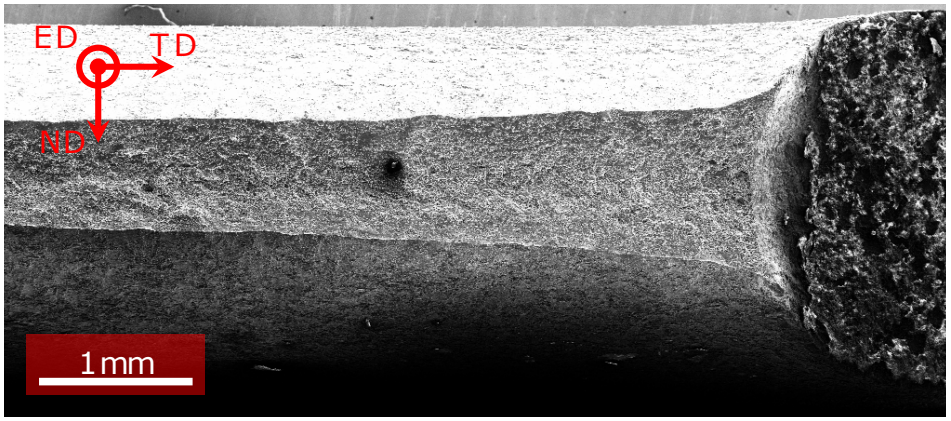

Figure 3.19: Fracture surfaces of a AA6060 AC ED Kahn tear test specimen. The figure is magnified by a factor of 20.

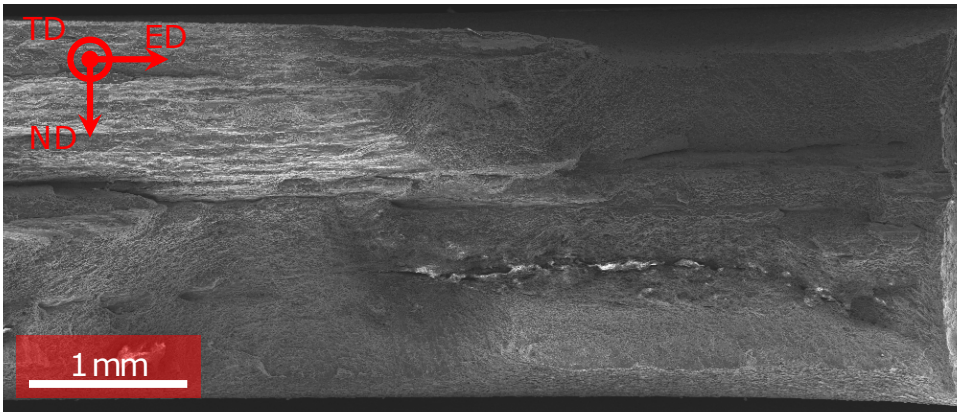

Figure 3.20: Fracture surfaces of a AA6082.50 WQ TD Kahn tear test specimen. The figure is magnified by a factor of 20.

The fracture surfaces of AA6082.50 can be seen in Figure 3.23. For both the air-cooled TD and ED sample there are smooth areas present in the fracture surface. This may indicate intergranular fracture. The rougher parts of these surfaces have some dimples with particles, but mostly another kind of dimples, smaller dimples seemingly without a particle. A higher magnification of the fracture surfaces of the air-cooled AA6082.50 in both TD and ED can be seen in Figure 3.24a and 3.24b respectively. In these figures these other kinds of dimples can be seen. What causes these dimples is uncertain. The fracture surface of AA6082.50 WQ ED seen in Figure 3.23d is almost purely dimpled, indicating mainly transgranular fracture.

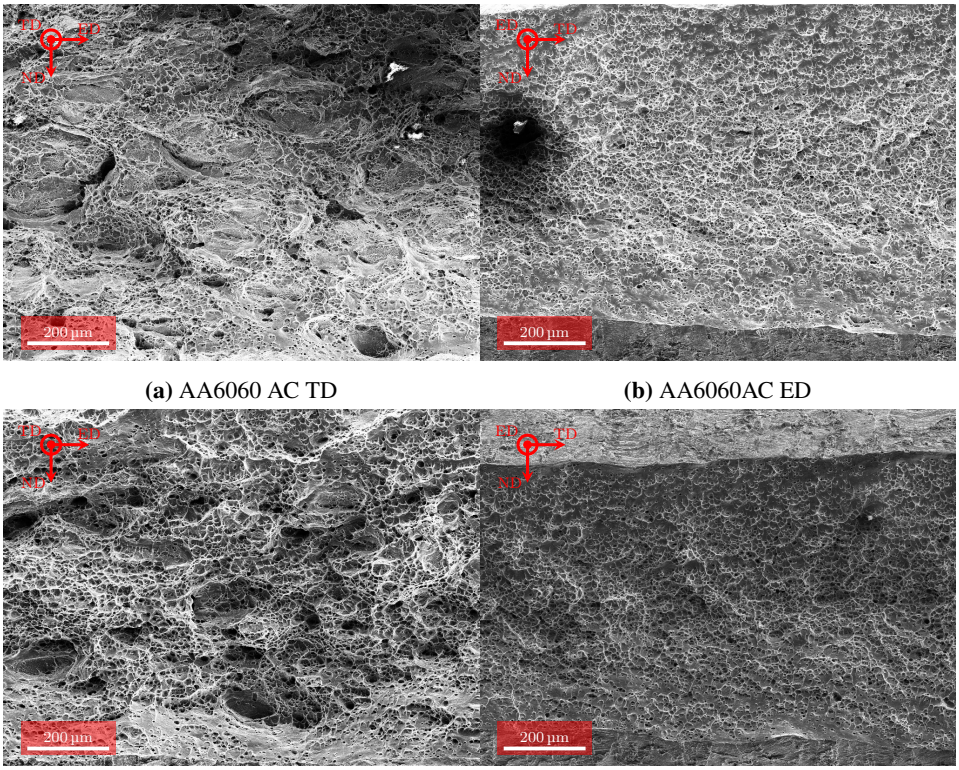

(a) AA6060 AC TD **(b)** AA6060AC ED

(c) AA6060 WQ TD **(d)** AA6060 WQ ED

Figure 3.21: Fracture surfaces of AA6060 Kahn tear test specimens. The figures are magnified by a factor of 100.

Figure 3.23c seems to have a mixture of transgranular and intergranular fracture. When comparing the force-displacement curves for AA6082.50, seen in Figure 3.16, AA6082.50 WQ ED is more ductile compared to AA6082.50 WQ TD. The higher ductility of AA6082.50 WQ ED compared to AA6082.50 WQ TD agrees well with the observations made in the SEM pictures of the fracture surfaces.

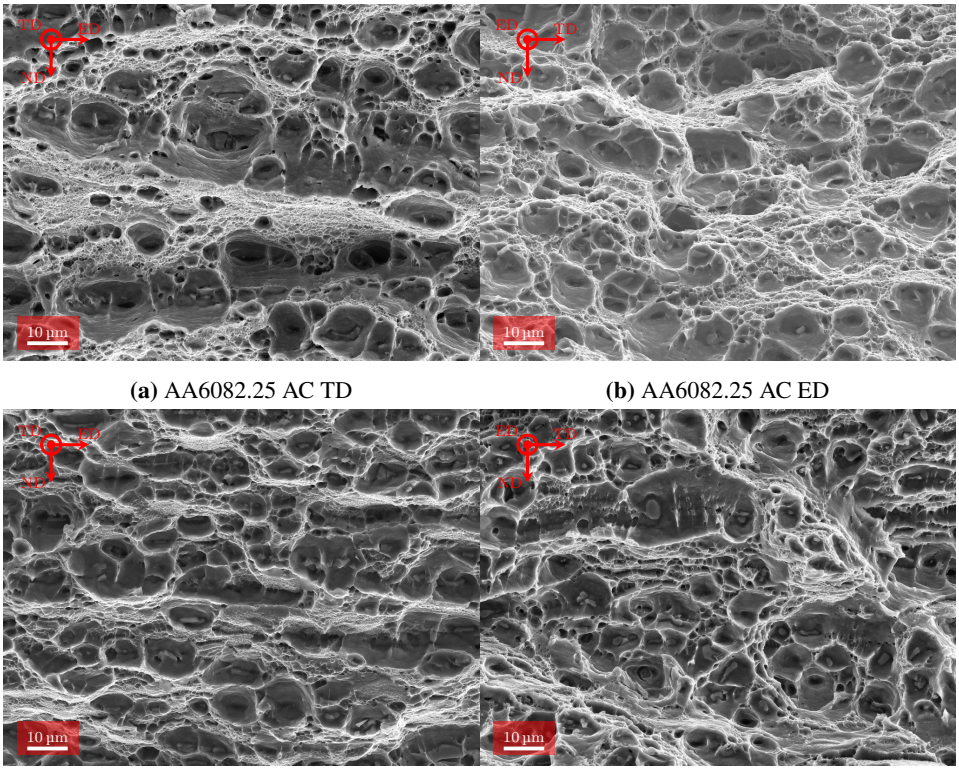

(a) AA6082.25 AC TD

(b) AA6082.25 AC ED

(c) 21AA6082.25 WQ TD

(d) AA6082.25 WQ ED

Figure 3.22: Fracture surfaces of AA6082.25 Kahn tear test specimens. The figures are magnified by a factor of 1000.

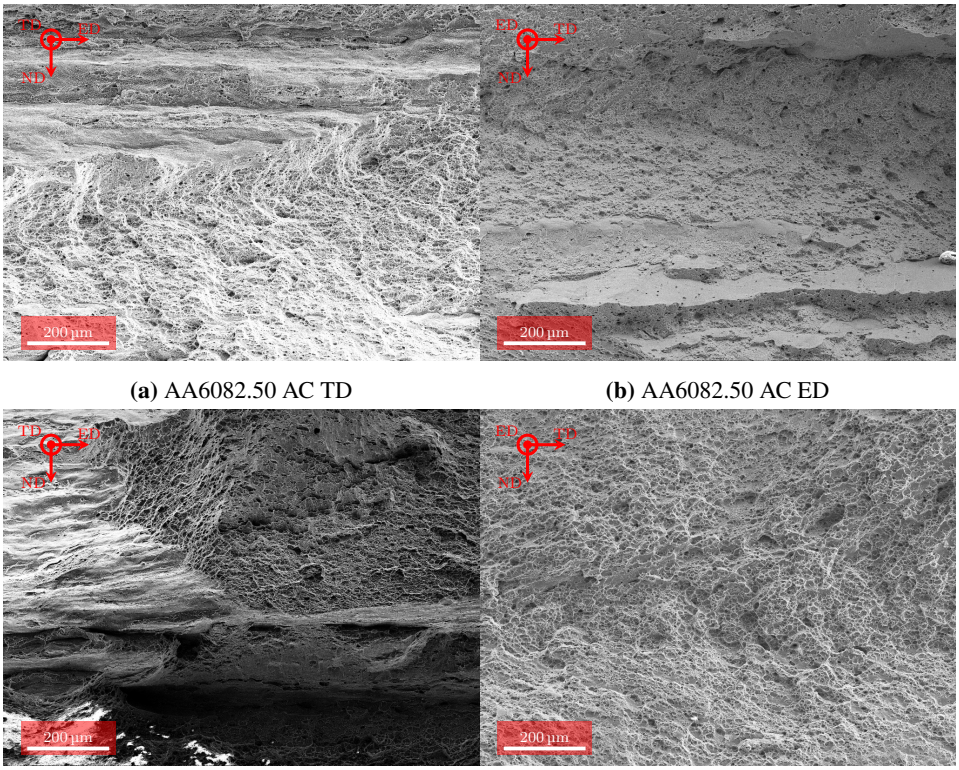

(a) AA6082.50 AC TD **(b)** AA6082.50 AC ED

(c) AA6082.50 WQ TD **(d)** AA6082.50 WQ ED.

Figure 3.23: Fracture surfaces of AA6082.50 Kahn tear test specimens. The figures are magnified by a factor of 100.

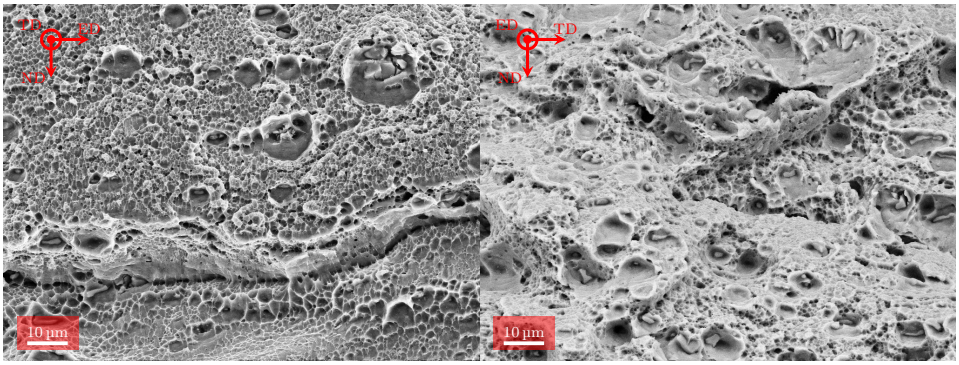

(a) AA6082.50 AC TD **(b)** AA6082.50 AC ED

Figure 3.24: Fracture surfaces of air-cooled AA6082.50 Kahn tear test specimens. The figures are magnified by a factor of 1000.

3.7 Investigation of microstructure

The microstructure of AA6060 and AA6082.25 was investigated using transmission electron microscopy (TEM). The microstructure of the air-cooled and water-quenched AA6060 can be seen in Figure 3.25a and 3.25b respectively. Both these figures are within the grain. From the figures it can be seen that the precipitates are a bit longer and in a larger number for the water-quenched AA6060, seen in Figure 3.25b. This explains a part of the reason for a higher strength of the water-quenched compared to the air-cooled, since dislocations will meet more resistance. In Figure 3.26a and 3.26b the microstructures of AA6082.25 AC and AA6082.25 WQ can be seen respectively. It is easy to see that the number of precipitates is much larger in the water-quenched seen in Figure 3.26b. The differences between the microstructures for an air-cooled and an water-quenched AA6082.25 is larger compared to AA6060. This makes sense since the same is seen for the force-displacement curves for the Kahn tear test in Section 3.5.3. The maximum force for a water-quenched AA6082.25 was almost twice as big as the air-cooled counterpart for both directions, as seen in Table 3.5. The same for AA6060 was only 12% and 18% for TD and ED respectively.

The width of the PFZ were measured and the results can be seen in Figure 3.27 and 3.28 for AA6060 and AA6082.25 respectively. Notice that the scale for the different figures are different, so they are not comparable by size, but the width of the PFZ is shown in each figure. The PFZ-widths are also shown in Table 3.7. For AA6060, the air-cooled has a PFZ-width of 170 nm and the water-quenched has a PFZ-width of 500 nm. The difference is quite large. However, this does not affect the force-elongation curves for AA6060 seen in Figure 3.14 in the same magnitude. The main difference between the force-elongation curve for AA6060 AC and AA6060 WQ for both ED and TD is the maximum force. This is probably first and foremost due to the difference in precipitate size and number as explained above. The width of the PFZ for AA6082.25 AC and AA6082.25 WQ can be seen

in Figure 3.28a and 3.28b respectively. The difference in PFZ-width between WQ and AC for AA608.25 has a magnitude of 10, which is much more than the difference for AA6060. Notice that the microstructure for AA6082.25 WQ varies quite a lot in the distribution of precipitates and the PFZ-width is measured where the PFZ-width is at its narrowest point. This large difference in PFZ-width does not reflect the difference in the force-elongation curve for the Kahn tear test for AA6082.25.

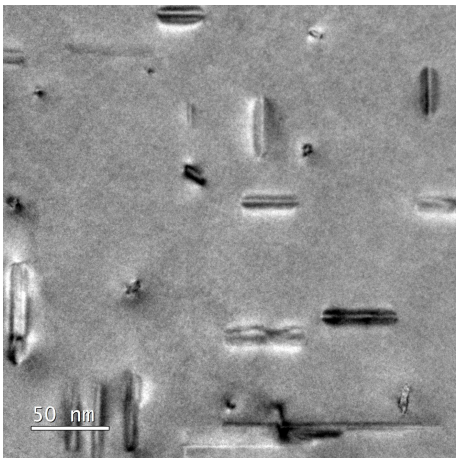

(a) AA6060 AC.

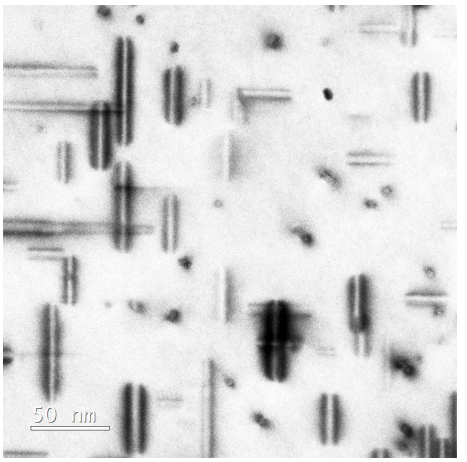

(b) AA6060 WQ.

Figure 3.25: Microstructure of AA6060 from TEM.

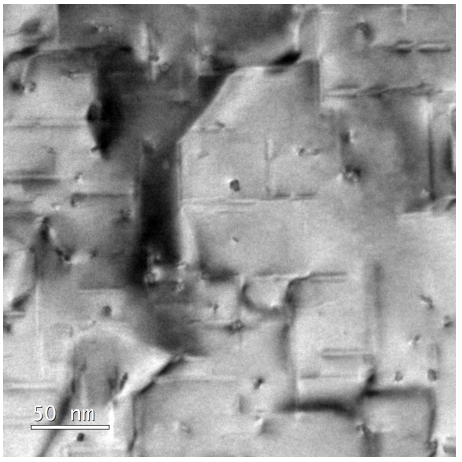

(a) AA6082.25 AC.

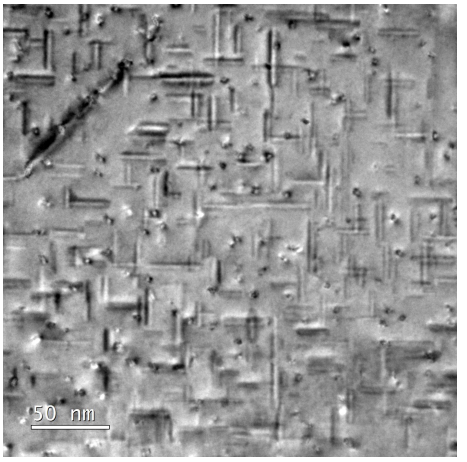

(b) AA6082.25 WQ.

Figure 3.26: Microstructure of AA6082.25 from TEM.

Table 3.7: Width of the PFZ for the different configurations.

Quenching method	AA6060 PFZ [nm]	AA6082.25 PFZ [nm]
AC	500	380*
WQ	170	40

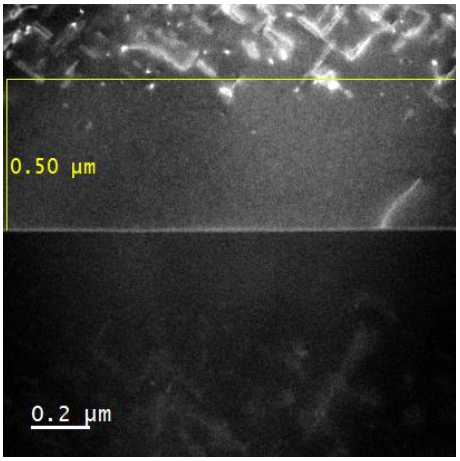

(a) AA6060 AC.

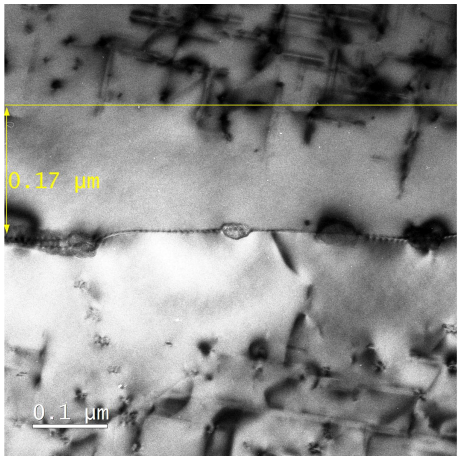

(b) AA6060 WQ.

Figure 3.27: PFZ-width of AA6060. Figure 3.27a is a High Angle Annular Dark Field (HAADF) from Scanning Transmission Electron Microscope (STEM). Figure 3.27b is taken from TEM.

3.8 Unexpected results

When this research started it was expected that the air-cooled specimens would have reduced ductility in terms of a smaller UPE. This was not the case. The UPE for the air-cooled Kahn tear test specimens is in three out of six cases larger than their water-quenched counterpart. In the cases where the water-quenched specimens has larger UPEs, the difference is maximum 13% and is mainly due to an increased maximum force. If comparing to the results of Morgeneyer et al. [3] seen in Figure 3.29 it can be seen that the UPE for the curve of the air-cooled specimen is smaller compared to the water-quenched ones. Morgeneyer et al. [3] also used two different water-quenches, one in water at 20°C and one at 60°C. The effect of this is quite interesting, as the two different quenching rates results in a very similar maximum force, but a faster decrease after maximum force for the one quenched in water at 60°C.

The quenching rates used in this thesis was may not be ideal for investigating the effect of the PFZ. A similar effect to that achieved between the water-quenches examined by Morgeneyer et al. [3] could have given a more desirable result. However, using air-cooling for the alloy investigated by Morgeneyer et al. [3] gave both reduced UIE, UPE and F_{max}. The alloy investigated by Morgeneyer et al. [3] was AA6156 and responds differently to quenching than the ones used in this thesis. Morgeneyer et al. [3] also

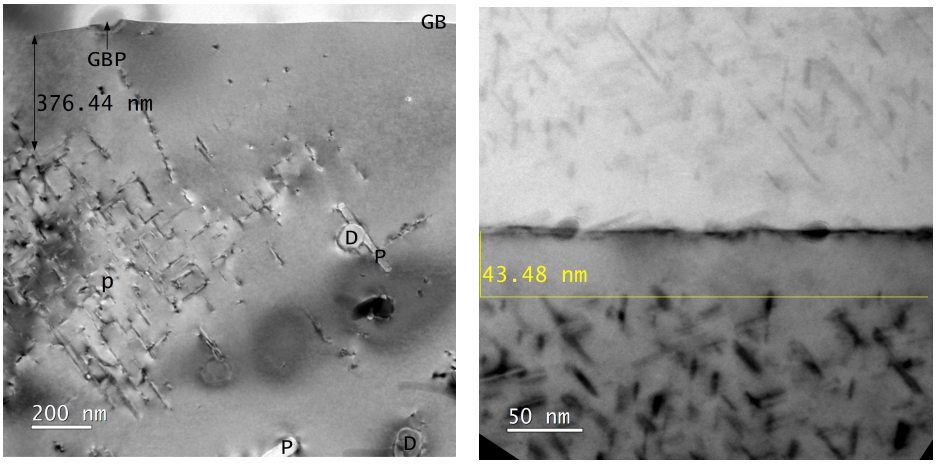

(a) AA6082.25 AC. **(b)** AA6082.25 WQ.

Figure 3.28: PFZ-width of AA6082.25 from TEM. In Figure 3.28a it is indicated what the different objects are. This was done by Emil Christiansen. D indicates disperoids, p indicates β''-precipitates, P indicates β-precipitates, GB indicates grain boundary and GBP indicates grain boundary particle.

plotted the crack length against the crack mouth opening displacement. This showed that for almost any given crack mouth opening displacement, the crack length was longer for the air-cooled specimen compared to the other two. This means that the crack propagated faster, indicating less resistance to crack propagation. This was not done in this thesis.

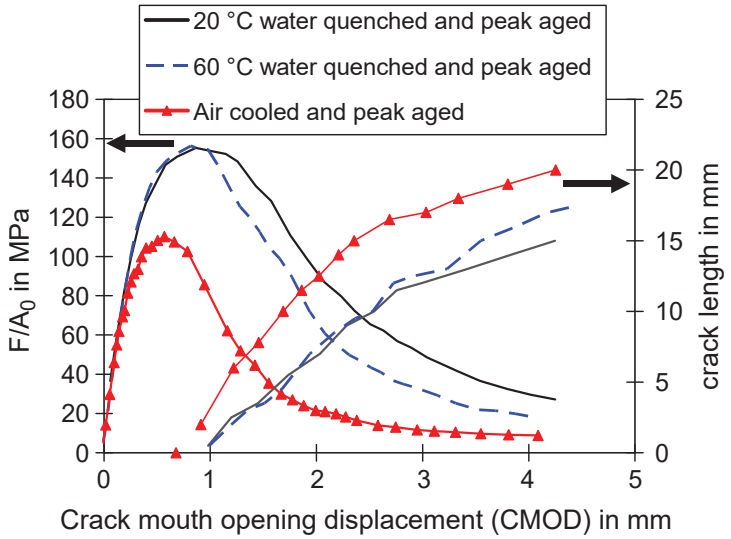

Figure 3.29: F/A_0-Crack mouth opening displacement and crack length- crack mouth opening displacement for AA6156. Adopted from Morgeneyer et al. [3].

Chapter 4

Numerical study

The tests performed in the experimental study are modelled in this chapter using the finite element- analysis-tool Abaqus. The component test in the numerical study is the Kahn tear test. The smooth tensile test was used to calibrate the strain hardening properties of the materials, and the v-notch tensile test was used to calibrate the fracture model of the materials. This was done by finding the initial volume fraction f_o giving a fracture strain similar to the experiments. This value was checked for the smooth tensile test to see if it fitted the experimental data. The reason for using the v-notch tensile test for calibrating the fracture model is that the Kahn tear test is more like the v-notch tensile test in terms of triaxiality compared to the smooth tensile test. Finally, the Kahn tear test was modelled with all the calibrated data.

First, an introduction to the units used in Abaqus is presented, followed by the hardening parameters found from the curve fitting. Then the calibration of the v-notch tensile test is performed, followed by a simulation for the smooth tensile tests. Lastly, the Kahn tear test is simulated.

4.1 Units in Abaqus

When modelling in Abaqus, the program does not provide any information about the units. This means that the user needs to keep control over the units. The first unit one needs to decide is the length, which is decided when the geometry is specified. In this thesis, millimetre is used. Every unit containing length from this point is defined with respect to mm. Density is the next unit defined, and mass is put to tonne so that the density equals:

$$[\rho] = \frac{\text{tonne}}{\text{mm}^3} \tag{4.1}$$

The force unit used is Newton. Newton is defined as:

$$\text{N} = \frac{\text{kg} * \text{m}}{\text{s}^2} \tag{4.2}$$

Inserting tonne and millimetre into Eq. 4.2, the correct time unit is found:

$$\frac{\text{kg} * \text{m}}{\text{s}^2} = \frac{10^{-3}\text{tonne} * 10^{3}\text{mm}}{\text{s}^2} = \frac{\text{tonne} * \text{mm}}{\text{s}^2} \tag{4.3}$$

It is seen that using tonne and millimetres is equivalent to using kilograms and meters, resulting in the time unit being defined in seconds. Properties with pressure units, such as yield stress and Young's modulus are then modelled in N/mm^2, which is equivalent to:

$$\frac{\text{N}}{\text{mm}^2} = \frac{\text{N}}{(10^{-3}\text{m})^2} = \text{MPa} \tag{4.4}$$

The boundary conditions will be applied in the form of velocity. The velocity is given in mm/s. All necessary units are then covered and summed up in Table 4.1. The density used is $2.7 * 10^{-9}$ tonne/mm^3. and the Young's modulus is 70000 MPa.

Table 4.1: Quantities with belonging units used for modelling in Abaqus.

Quantity	Unit
Length	mm
Mass	tonne
Density	tonne/mm^3
Force	N
Time	s
Pressure	MPa
Velocity	mm/s

4.2 Work-hardening parameters

To calibrate the material model, the smooth tensile tests were used first. From the experimental data, the true-stress-strain curves were calculated, as shown in Section 3.4. To be able to make Voce-curves from the smooth tensile tests a Bridgman-LeRoy correction was performed, as explained in Section 2.1.3. This correction is done after necking due to a triaxial stress state introduced in the necking area. The Bridgman-LeRoy correction gives the equivalent von Mises stress.

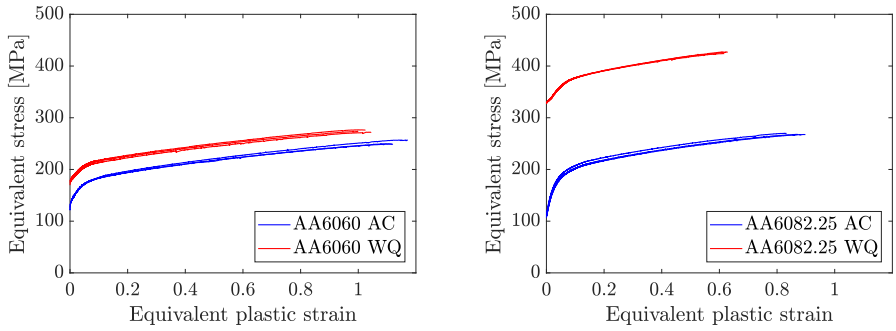

(a) AA6060. **(b)** AA6082.25.

Figure 4.1: Equivalent stress vs. plastic strain curves calibrated based on the smooth tensile test.

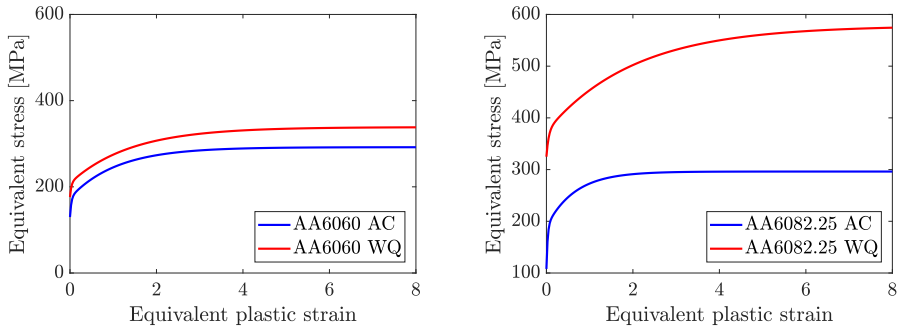

(a) AA6060. **(b)** AA6082.25.

Figure 4.2: Equivalent stress vs. plastic strain curves defined by the Voce rule.

Table 4.2: Voce-parameters from the smooth tensile tests.

Material	σ_0(MPa)	C_1	C_2	Q_1(MPa)	Q_2(MPa)
AA6060AC	129.9	0.9186	32.81	117.3	44.76
AA6060WQ	176.3	0.7091	31.84	129.8	32.43
AA6082.25AC	107.9	1.523	36.14	106.5	81.81
AA6082.25WQ	324.9	0.4927	19.84	204.3	49.16

The equivalent stress- logarithmic plastic strain plots can be seen in Figure 4.1. These curves were fitted to the Voce-rule introduced in Section 2.1.3. From the fitting, the variables presented in Table 4.2 were determined. The Voce-rule was then used to tabulate the equivalent stress and equivalent plastic strain in Abaqus. The curves were calculated in MATLAB using a 0.025 step length for plastic strains ranging from zero to eight. The plots can be seen in Figure 4.2. The plastic strain was put as high as eight to ensure that

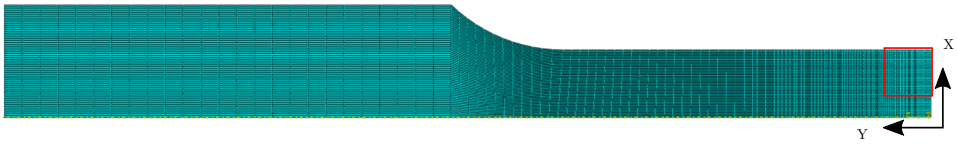

Figure 4.3: Smooth tensile test specimen mesh. The red square indicates where the close-up shown in Figure 4.5a is taken from. The coordinate system indicates directions from Abaqus.

no strain exceeds the tabulated values. By plotting them this far, it is also easy to see that the curves saturate to the value of $\sigma_0 + Q_1 + Q_2$.

4.3 Smooth round tensile test

The smooth tensile test was modelled using an axisymmetric model in Abaqus. The solver used was explicit. No mass scaling was used, but a time scale resulting in negligible kinetic energy compared to the internal- and strain-energy was used. Different time scales were performed to find a time scale with negligible kinetic energy. The geometry of the finite element model is shown in Figure 4.3. A close-up of the smooth tensile test specimen mesh indicated by the red square shown in Figure 4.3 can be seen in Figure 4.5a. The elements used were linear axisymmetric elements with reduced integration, CAX4R-elements. The size of the elements was varied, with large elements at the thick end of the test specimen, reducing the element size linearly closer to the thin end of the test specimen. The smallest element was 0.05 millimetres in length and height. The elements near the centre line becomes profoundly distorted. Using too large elements will result in high artificial strains and affect the result, resulting in the need of small elements near the centre line. The smallest elements in use could have been applied for the entire model, but this is unnecessary. Using larger elements where the deformations are smaller saves computing time and gives a negligible effect on the result.

4.4 V-notch round tensile test

The v-notch tensile test was like the smooth tensile test modelled using an axisymmetric model in Abaqus and the same solver and scaling methods were used. The geometry of the finite element model with mesh is shown in Figure 4.4. Figure 4.5b shows a close-up of the v-notch specimen at the notch root. This close-up corresponds to the red square in Figure 4.4. The elements used along the centre line are 0.025*0.020 mm^2 in size. In area this is one fifth the size of the smallest elements used in the smooth tensile test. This was due to larger local deformations around the notch root, smaller elements were therefore needed to give a satisfactory simulation. The elements used for the v-notch tensile test was the same as for the smooth tensile test, linear axisymmetric elements with reduced integration, CAX4R-elements.

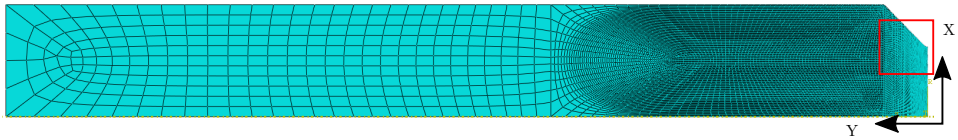

Figure 4.4: V-notch tensile test specimen mesh. The red square indicates where the close-up shown in Figure 4.5b is taken from. The coordinate system indicates directions from Abaqus.

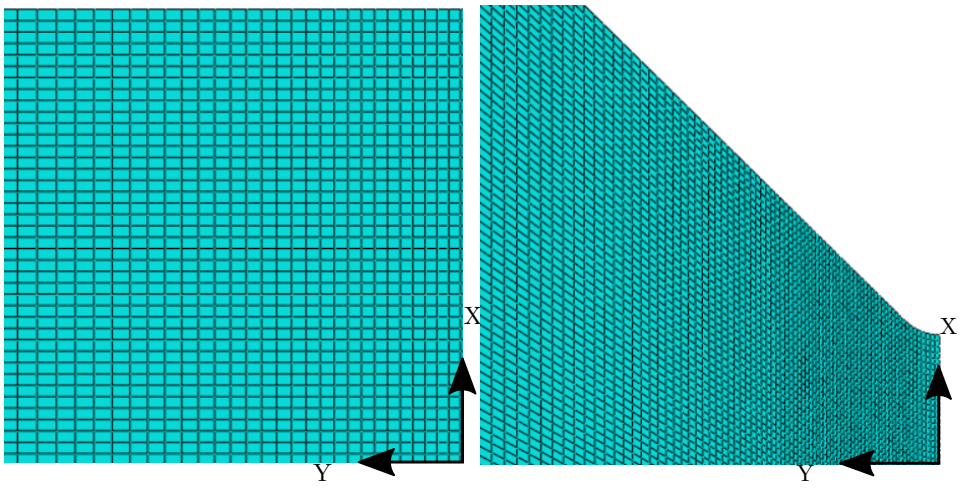

(a) Close-up of the smooth tensile test mesh. **(b)** Close-up of the v-notch tensile test mesh.

Figure 4.5: Close-up of the smooth- and v-notch- tensile test specimen mesh. The close-ups are taken from the squares shown in Figure 4.3 and 4.4. The coordinate system indicates directions from Abaqus.

4.4.1 Calibration of the initial volume fraction

The initial void volume fraction, f_0, is as mentioned in Section 2.7 used in the GTN- model to represent as the name indicates, the initial volume fraction of voids. The effect of this parameter on the true stress-strain curve for the v-notch tensile test is investigated in this section. The upper boundary for the initial volume fractions was put equal to the fraction of constituent particle found by Frodal et al.[21], which is $f_p = 0.0093$ and $f_p = 0.0120$ for AA6060 and AA6082.25 respectively. The void volume fraction at failure, f_F, and the critical void volume fraction, f_c are kept constant at 0.6, which was decided after private communication [22]. This means that the elements fail when the void volume fraction equals 0.6. Notice that the maximum theoretical value of f with the values used of q_1 and q_3 used in this thesis is 2/3, as given in Eq. 2.27.

Figure 4.6a and Figure 4.6b show the contour plots of equivalent plastic strain and void volume fraction in the v-notch specimen right before the first element breaks. It can be seen that there is an ongoing crack developing going up to the left in the figures. This insta-

bility eventually leads to the crack path shown in Figure 4.7. The crack path changed from simulation to simulation, but it does not affect the true stress- logarithmic strain curves for the simulations since failure occurs at the very end of the simulation.

The true-stress-strain curves for simulations with the different values of the initial volume fraction and the experimental curves are presented below. The curves are plotted further compared to the experimental results presented in Chapter 3. The reason for this is to illustrate the difference in fracture strain. This is also how the void volume fraction was calibrated, by visually matching the fracture strain, as this is easy to see. The strain at maximum stress is more difficult to identify, as the slope is very flat near this point. The simulated curves were often overestimated near the maximum stress, making it difficult to match the strain at maximum stress. The fracture strain on the other hand was much easier to match.

The true stress vs. logarithmic strain curves from the experiments together with the simulations for the air-cooled AA6060 can be seen in Figure 4.8. For the air-cooled AA6060, an initial void volume fraction of 0.0031 was found to give the most accurate result compared to the experiments. Changing f_0 changes the fracture strain and has a small influence on the maximum stress. The calibrated initial void volume fraction was checked with the smooth tensile test, as seen in Figure 4.9. In this figure, it can be seen that using an initial void volume fraction equal to 0.0031 gives a good result for the smooth tensile test. The maximum stress is quite similar, but the strain at maximum stress is shifted. In the same figure, a curve from a simulation of AA6060 AC without porosity in the GTN-model, which means $f_0 = 0$, can be seen. The stress grows way beyond the maximum point.

The result of the calibration of the water-quenched AA6060, the air-cooled AA6082.25 and the water quenched AA6082.25 can be seen in Figure 4.10, 4.12 and 4.14 respectively. The calibrated values can be seen in Table 4.3. The air-cooled and water-quenched AA6060 have quite similar initial void volume fractions. The initial void volume fraction of the air-cooled AA6082.25 is a bit larger than the configurations of AA6060. The water-quenched AA6082.25 however, has a much higher initial void volume fraction compared to the others. This can be explained by the low fracture strain of this configuration. The void volume fraction at failure was held constant, so to obtain an earlier fracture the initial void volume fraction needed to be larger.

The simulated curves follow the experiments satisfactorily. An interesting observation is that the simulations of the air-cooled AA6060 have the most similar curves compared to the curves from the experiment. The other configurations have simulations where the calculated stress is larger compared to the experimental values at almost any given point. This is probably due to modelling limitations of the GTN-model. AA6060 and AA6082.25 were shown to be pressure sensitive by Holmen et al. [9]. This together with anisotropic effects may be the reason for a difference between the simulated curves and the experimental ones.

The smooth tensile test simulations for AA6060 WQ, AA6082.25 AC and AA6082.25

WQ can be seen in Figure 4.11, 4.13 and 4.15, respectively. All of them fit the slope of the stress quite well, but the strains at maximum stress are significantly overestimated for both configurations of AA6082.25, especially the water-quenched one. The reason for this may be that the elements used were not small enough.

In Figure 4.16 the void volume fraction is plotted against the equivalent plastic strain in the notch-root element for AA6082.25 WQ. From this figure, it can be seen that a higher initial void volume fraction leads to a faster void growth. The faster the void growth, the faster the elements reach the critical void volume fraction resulting in a lower fracture strain.

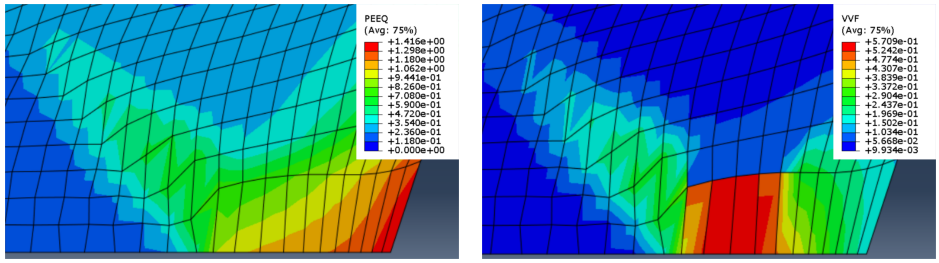

(a) Equivalent plastic strain. **(b)** Void volume fraction.

Figure 4.6: Contour plots showing equivalent plastic strain and void volume fraction in the v-notch tensile test right before the first elements fail.

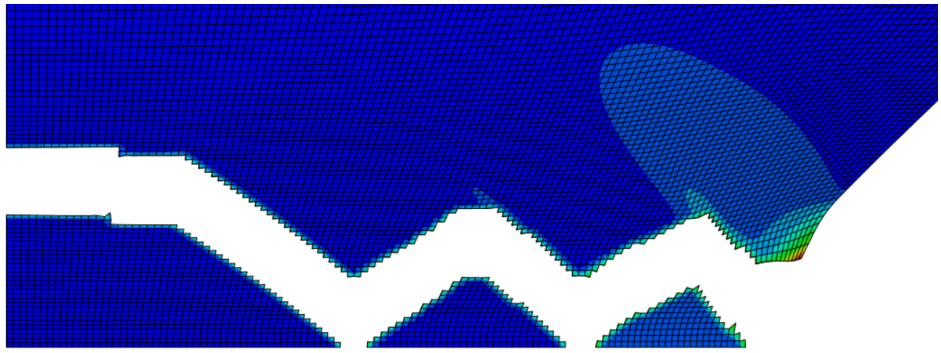

Figure 4.7: Crack path of one of the v-notch test simulations.

Table 4.3: Initial void volume fractions for the different materials calibrated from the v-notch tensile test.

Alloy	Initial void volume fraction, f_0
AA6060AC	0.0031
AA6060WQ	0.0035
AA6082.25AC	0.0042
AA6082.25WQ	0.01

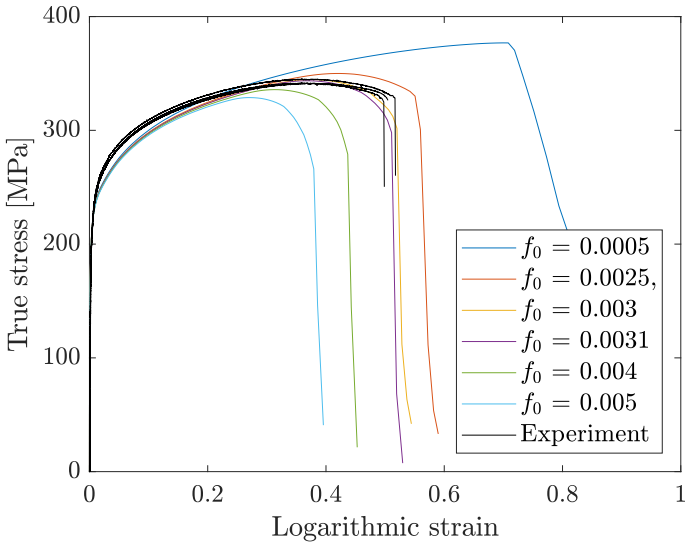

Figure 4.8: True stress vs. logarithmic strain curves for different initial void volume fractions for the AA6060 AC v-notch tensile test.

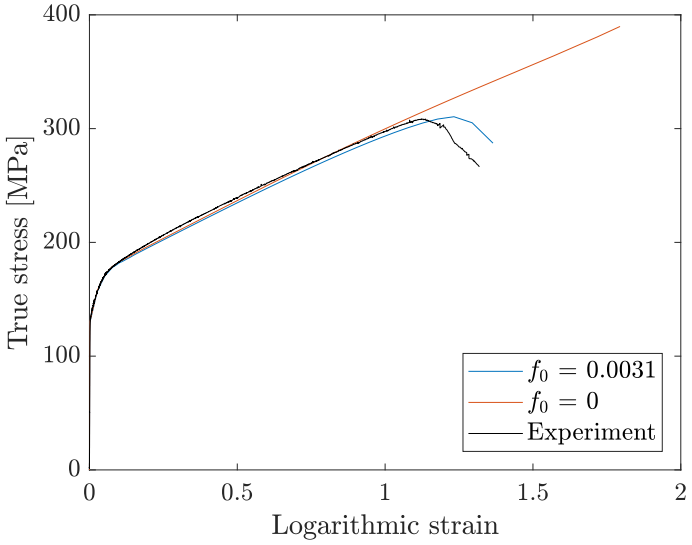

Figure 4.9: True stress vs. logarithmic strain curves for the AA6060 AC smooth tensile test. The blue curve is with the initial void volume fraction calibrated from the v-notch tensile test and the brown one is with $f_0 = 0$ resulting in no porosity in the material.

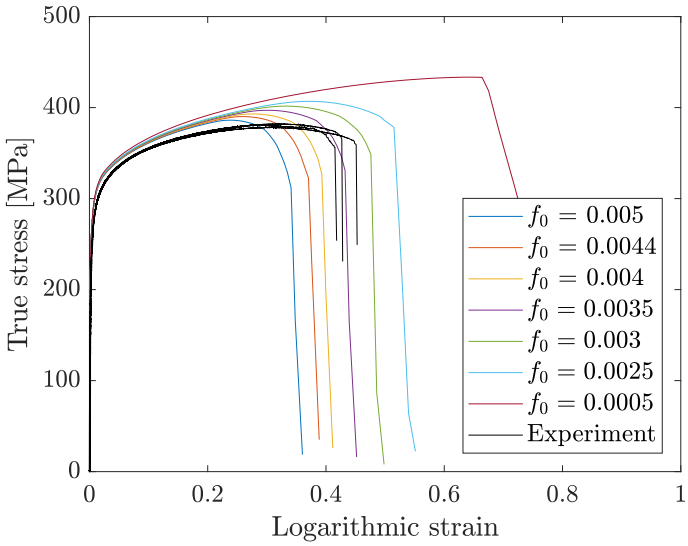

Figure 4.10: True stress vs. logarithmic strain curves for different initial void volume fractions for the AA6060 WQ v-notch tensile test.

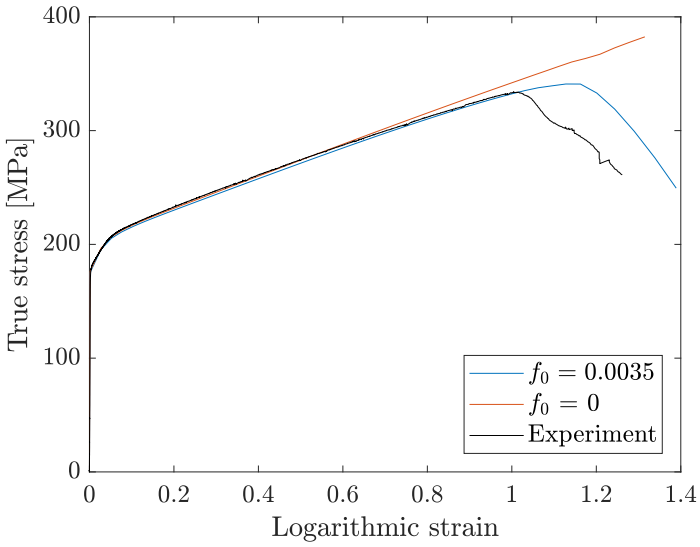

Figure 4.11: True stress vs. logarithmic strain curves for the AA6060 WQ smooth tensile test. The blue curve is with the initial void volume fraction calibrated from the v-notch tensile test and the brown one is with $f_0 = 0$ resulting in no porosity in the material.

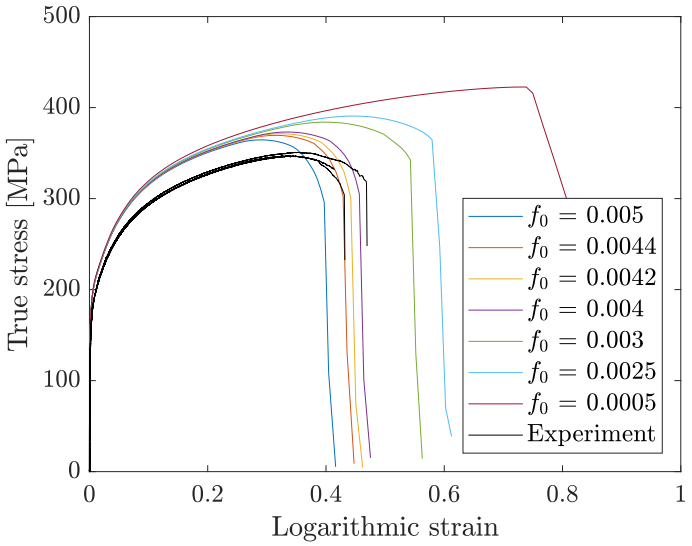

Figure 4.12: True stress vs. logarithmic strain curves for different initial void volume fractions for the AA6082.25 AC v-notch tensile test.

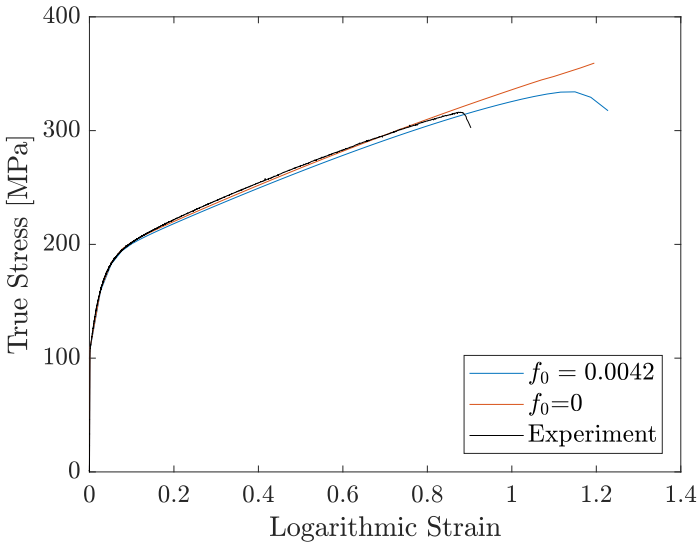

Figure 4.13: True stress vs. logarithmic strain curves for the AA6082.25 AC smooth tensile test. The blue curve is with the initial void volume fraction calibrated from the v-notch tensile test and the brown one is with $f_0 = 0$ resulting in no porosity in the material.

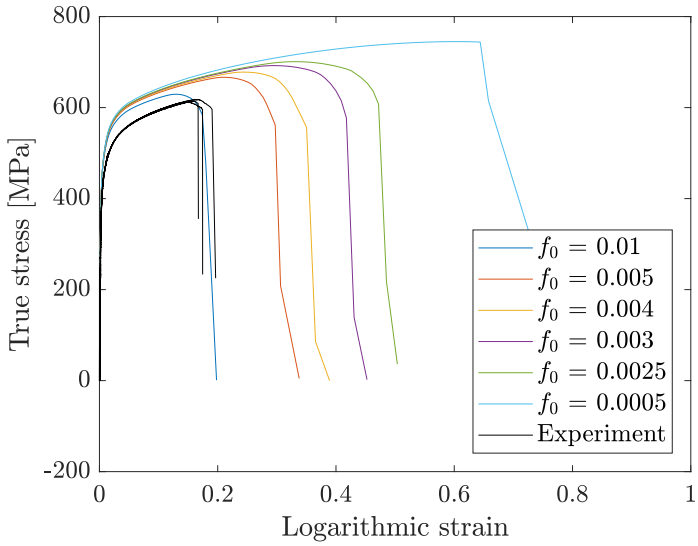

Figure 4.14: True stress vs. logarithmic strain curves for different initial void volume fractions for the AA6082.25 WQ v-notch tensile test.

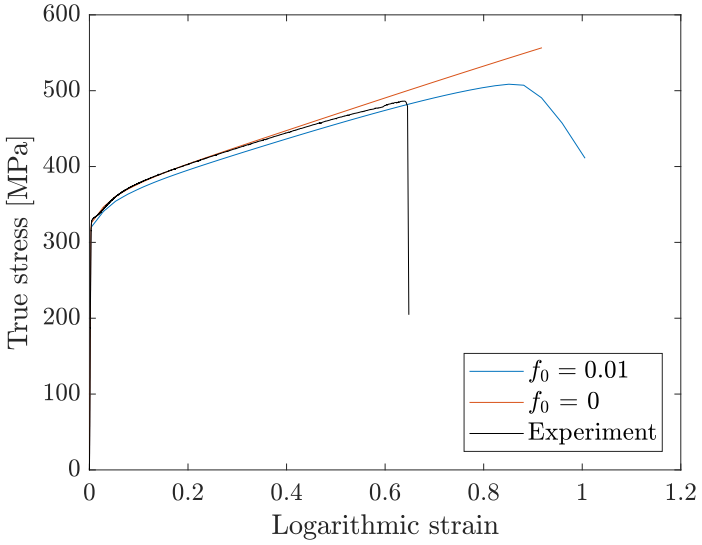

Figure 4.15: True stress vs. logarithmic strain curves for the AA6082.25 WQ smooth tensile test. The blue curve is with the initial void volume fraction calibrated from the v-notch tensile test and the brown one is with $f_0 = 0$ resulting in no porosity in the material.

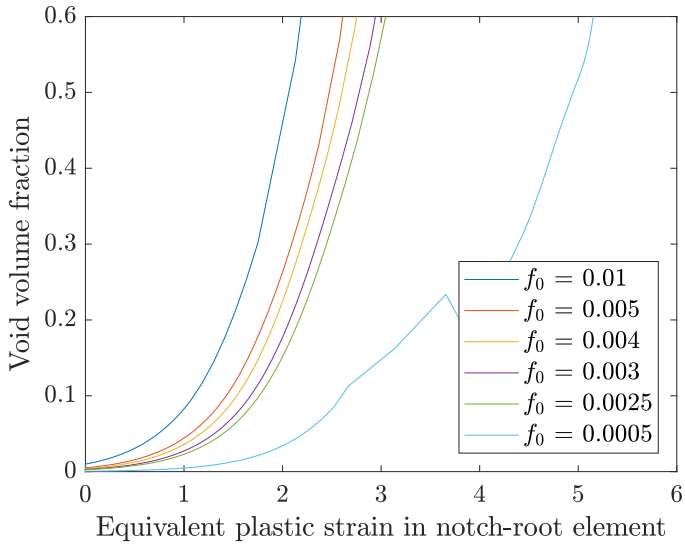

Figure 4.16: Void volume fraction-equivalent plastic strain curves for the AA6082.25 WQ v-notch tensile test for the same initial void volume fractions used in the true stress-true strain curves for AA6082.25 WQ.

4.5 The Kahn tear test

4.5.1 DIC- analysis

The pictures taken during the Kahn tear tests were used to perform a digital image correlation (DIC) analysis. The software eCorr was used to perform the DIC-analysis. A mesh consisting of Q4 elements was applied to the central region of the test specimen as shown in Figure 4.19. An element size of $25 * 25$ pixels was used. eCorr runs through the picture series, and based on the initial average gray tone in one element it traces the element's movement and shape as loading is applied.

The crosshead displacement read from the loading machine cannot be used to compare with the applied displacement in the simulation because the crosshead displacement from the machine may be affected by the stiffness. The displacements extracted from the DIC-mesh, however, can be used to compare with the Abaqus model. Vectors were made in the mesh in eCorr, and the elongation of the vector was traced during loading. One of these vectors can be seen in Figure 4.18.

Q4 elements are two dimensional. There are therefore only two in-plane principal strains, ε_1 and ε_2. If there are negligible elastic strains and plastic incomprehensibility is assumed [24], which is done in this case, the third principal strain ε_3 can be calculated through the

constant volume equation:

$$\varepsilon_1 + \varepsilon_2 + \varepsilon_3 = 0 \tag{4.5}$$

ε_3 can then be expressed as:

$$\varepsilon_3 = -(\varepsilon_1 + \varepsilon_2) \tag{4.6}$$

From the three principal strains, the effective strain ε_{eff} from the von Mises norm is as follows:

$$\varepsilon_{eff} = \sqrt{\frac{2}{3}(\varepsilon_1^2 + \varepsilon_2^2 + \varepsilon_3^2)} \tag{4.7}$$

The Q4 elements are not deleted unless specified. If not specified, the elements which cross the crack path will be distorted unreasonably, as seen in Figure 4.17a. The strain to failure for the elements needed to be adjusted to erode elements at the right time during the crack propagation. For AA6060 a critical strain value of 1 was found to be sufficient. For AA6082.25 AA6082.50, a critical strain value of 0.5 was sufficient. These estimations were only based on what appeared reasonable. They are therefore only rough estimates. In Figure 4.17b the DIC-analysis with element erosion can be seen. The elements are relatively large, so the crack is not followed perfectly.

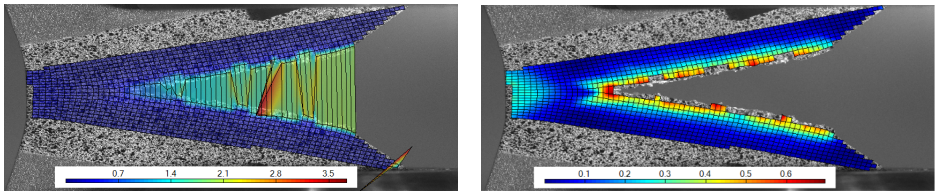

(a) Without element erosion. **(b)** With element erosion.

Figure 4.17: The DIC-mesh of a AA6060 AC TD specimen before and after element erosion is applied.

4.5.2 Numerical model

The Kahn tear test was modeled using linear 3D- brick elements with reduced integration, C3D8R-elements, in Abaqus. The simulation was done using the explicit solver. No mass scaling was used, but a time scaling with negligible dynamic effects was used. This saves computational time. The whole meshed model can be seen in Figure 4.20 and a close-up around the notch tip can be seen in Figure 4.21. Due to symmetry in the z-direction and y-direction, seen in Figure 4.20, only one-fourth of the geometry was modeled, applying symmetry boundary conditions to simulate the test. The fracture is expected to go along the x-axis seen in Figure 4.20, a fine mesh was therefore used along this path, and a coarser mesh in the rest of the model to save computational time. The smallest elements were approximately 0.05 millimeters in width, height, and depth. The smallest elements used for the v-notch tensile test are smaller in length and width than the smallest for the Kahn tear test. Axisymmetric elements are 2-dimensional, hence they have no depth.

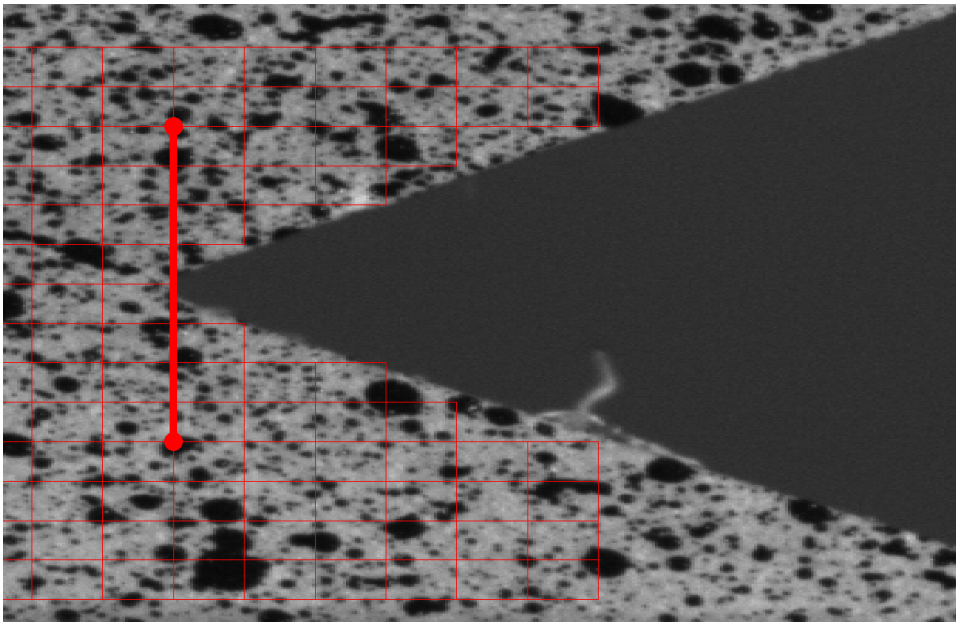

Figure 4.18: The vector used to extract elongation for the force-elongation curve in eCorr.

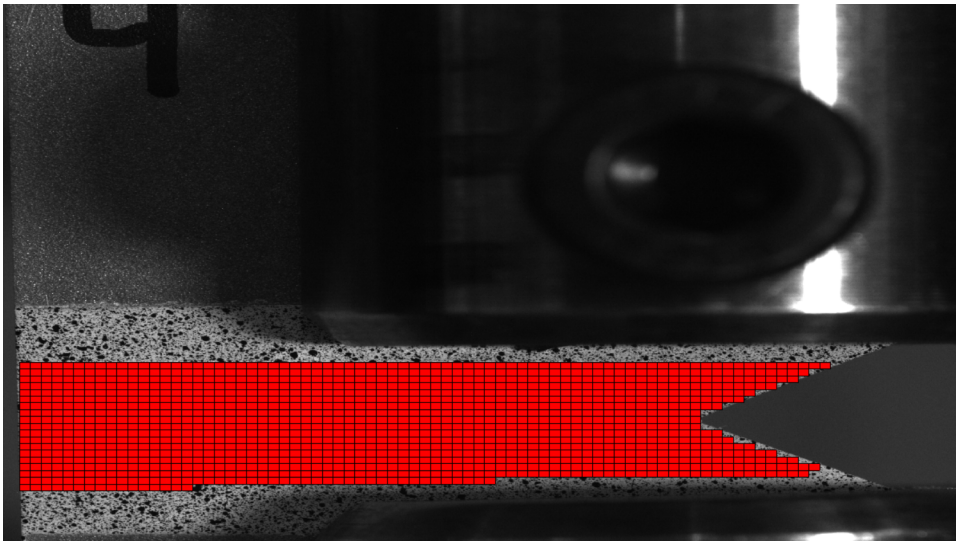

Figure 4.19: Q4 mesh on test specimen 4 used in the DIC- analysis.

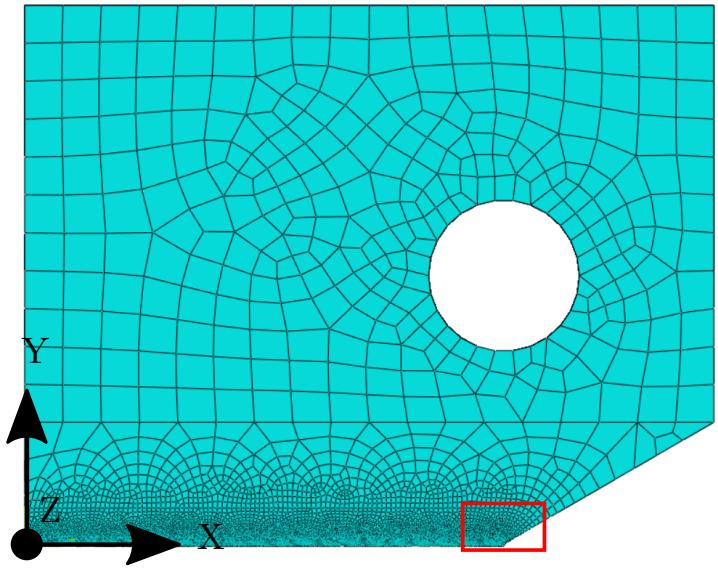

Figure 4.20: Kahn tear test geometry with mesh. The red square indicates where the close-up in Figure 4.21 is taken from.

The reason for smaller elements needed for the v-notch tensile test is that usually axisymmetric elements need to be smaller compared to 3D- elements to give a satisfactory result. The Kahn tear test was conducted in both ED and TD. The smooth tensile tests and the v-notch tensile test were only in TD. The experiments in TD will be the main comparison to the simulations, but the data from the tests in ED will also be presented. No smooth tensile tests or v-notch tensile tests were conducted for AA608.50. For this reason, no simulations will be performed on this alloy.

4.5.3 Numerical results

The calibrated initial void volume fraction from the v-notch test simulations were used for the Kahn tear test simulation. To give comparable results the resulting force from the simulation was plotted against the elongation of a vector from the simulation corresponding to the vector defined in eCorr. The vector from the simulation can be seen in Figure 4.18. The vector defined from the simulation was taken from the notch root to a node lying in a similar distance to the one from the DIC- analysis, as seen in Figure 4.21. A deformed simulated Kahn tear test can be seen in Figure 4.30. The figure is mirrored making it easier to see the deformation.

4.5.3.1 Force-elongation curves

The result for AA6060AC can be seen in Figure 4.23. The simulated force-elongation curve fits the experimental curves quite well. The experimental maximum force in TD is only about 5% higher than in the simulation. It is interesting to see that the curve from

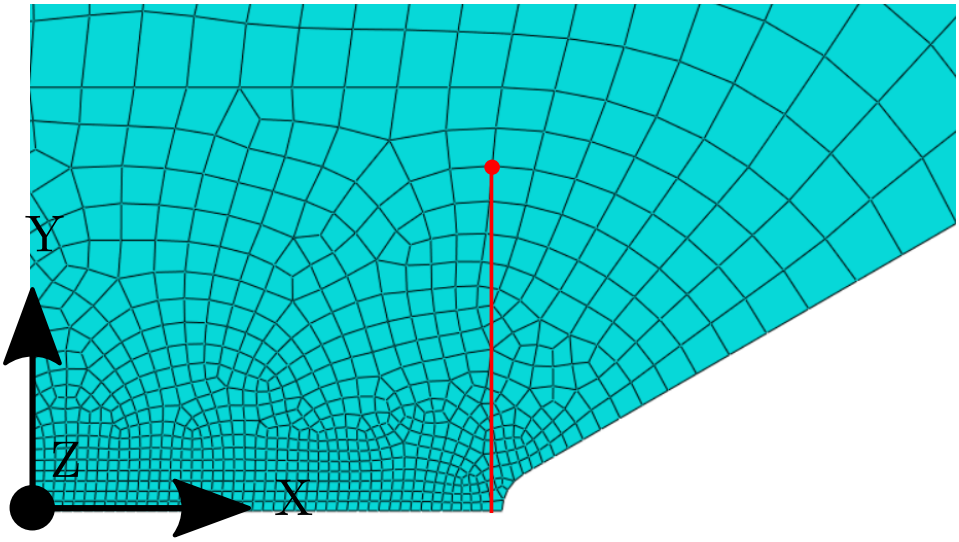

Figure 4.21: Close-up of the Kahn tear test mesh. The red dot indicates the node in which the displacement is extracted from. The red line is the monitored vector used to plot the force-elongation curve for the simulation. The close-up is taken from the area indicated by the square in Figure 4.20.

the simulation lies between the two experimental ones. The curves also follow each other quite well after maximum force. The applied velocity in the simulation was 1 m/s and from the energy curves in Figure 4.22b it can be seen that the strain energy is larger than the kinetic energy. The internal energy seen in Figure 4.22a is much larger than the kinetic energy. These observations together with a smooth force curve indicates that the velocity should not affect the result. This is desirable since the experiment was quasi-static. Different velocities were tested for the simulation. A higher velocity resulted in a higher maximum force.

The most promising simulation is the one for AA6060 WQ. The force-elongation curve of the simulation and a representative curve for the experiment in both TD and ED can be seen in Figure 4.24 and it is seen that the simulation curve follows the experimental in TD very well. The one in ED lies a bit underneath.

The force-elongation curve of the simulation of AA6082.25 AC with representative curves from the experiments can be seen in Figure 4.25. The plots do not follow each other as well as for AA6060 AC and AA6060 WQ. AA6082.25 was established in Section 3.5 to be the most isotropic alloy of the ones tested, as also seen in Figure 4.25. The maximum force is overestimated by 10% compared to TD. After maximum force, the curve from the simulation lies above the experimental ones. They have a similar slope, but the simulation overestimates the force value. This may be due to the observed intergranular fracture in the AA6082.25 AC. The GTN model can simulate fracture by void nucleation, growth and coalescence only. If there are other fracture mechanisms present, the simulated result may

differ from the experimental one.

The force-elongation curve of AA6082.25 WQ can be seen in Figure 4.26. This is the most inaccurate result compared to the experiments. The maximum force is better matched compared to the AA6082.25 AC, with a difference of only around 5% compared to TD, which is about the same as for AA6060 AC. The main problem is after maximum force. The force-elongation curve from the experiments drops quite quickly compared to the simulation. The reason for a larger mismatch, in this case, is probably some of the same reasons as for AA6082.25 AC. The fracture mechanisms present in AA6082.25 WQ is not only fractured by void nucleation, growth and coalescence. There are probably some fracture mechanisms related to the intergranular fracture, observed in Section 3.6. These fracture mechanisms are not represented by the GTN model.

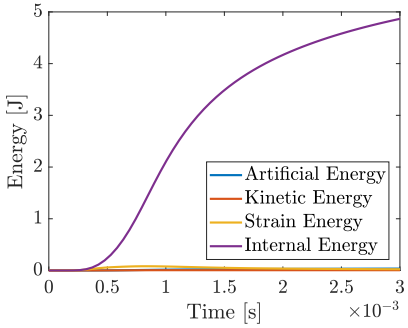

(a) Energies from the simulation of AA6060AC, including internal energy.

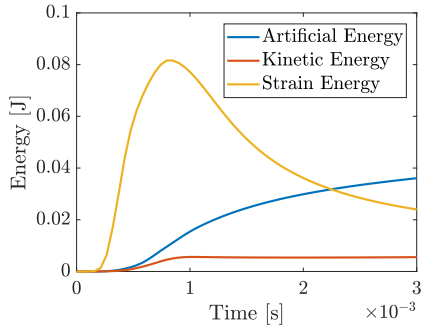

(b) Energies from the simulation of AA6060AC, not including internal energy.

Figure 4.22: Energies from the AA6060 AC simulation.

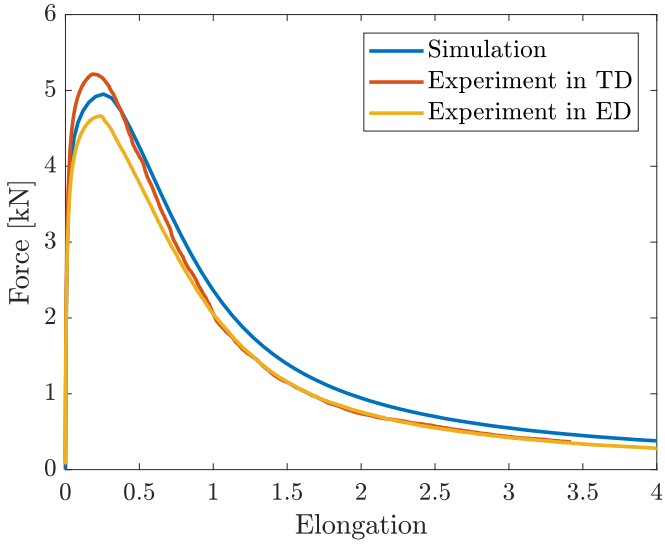

Figure 4.23: Fore-Elongation curves for the simulation and a representative test specimen in TD and ED of AA6060 AC.

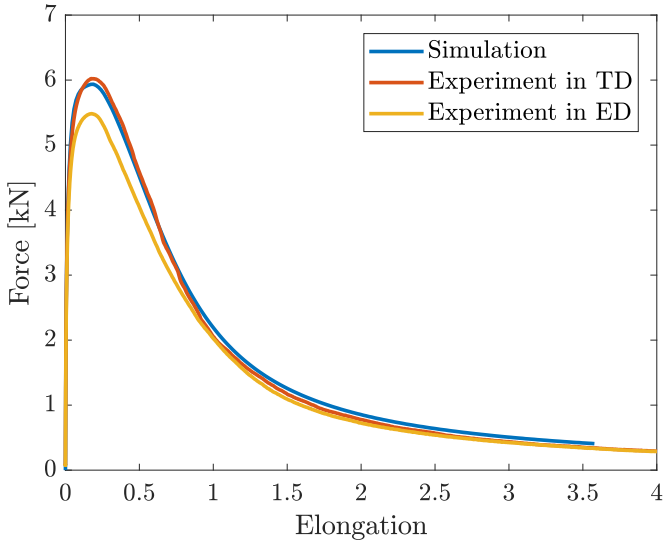

Figure 4.24: Fore-Elongation curves for the simulation and a representative test specimen in TD and ED of AA6060 WQ.

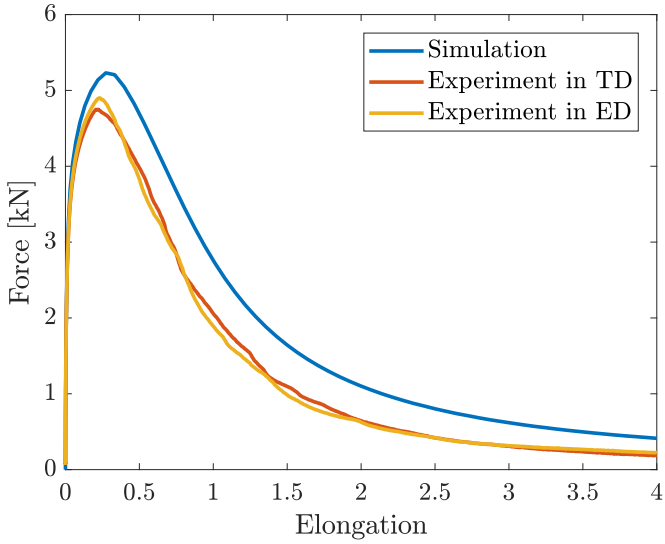

Figure 4.25: Fore-Elongation curves for the simulation and a representative test specimen in TD and ED of AA6082.25 AC.

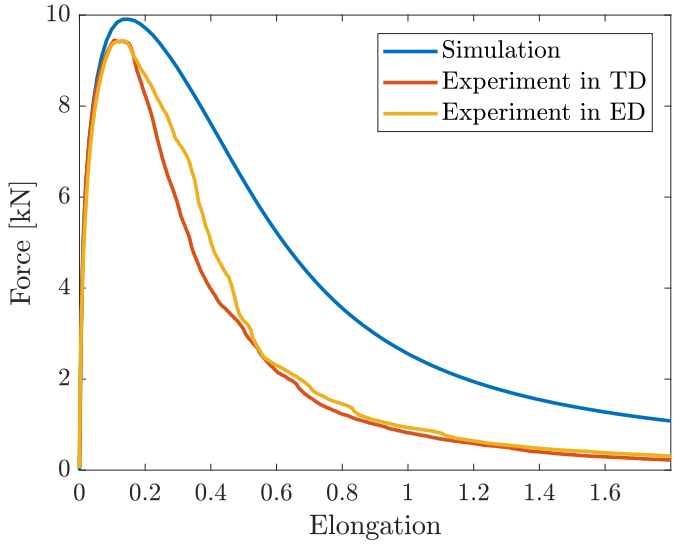

Figure 4.26: Fore-Elongation curves for the simulation and a representative test specimen in TD and ED of AA6082.25 WQ.

4.5.3.2 Deformation patterns

Figure 4.27 and 4.28 show the strain fields at maximum force for AA6082.25 WQ. Figure 4.27 shows the strain field from the simulation and Figure 4.28 shows the strain field from the experiments computed using eCorr. The equivalent strains from Abaqus and the effective strains from eCorr can be compared to each other. The largest strains present in the simulation are around 1.75. The largest strains from the experiment are only around 0.35. The reason for this large difference is that the simulation uses much smaller elements resulting in larger local strains in the small elements near the crack tip. In Figure 4.27 the gray area contains strains that are larger than the maximum strain from Figure 4.28. The red color in both figures represent the same strain. Going further away from the notch root it can be seen that the strains from the simulation become more similar to the experimental values.

To illustrate the evolution of the void volume fraction, a series of figures taken at different time steps during the simulation of AA6082.25 WQ can be seen in Figure 4.33a-4.33f. Figure 4.33a is taken at the time step before the first elements fail. Figure 4.33c is taken at the first time step at which elements have been deleted. It can be observed that the first elements to fail are located just within the notch root. The bottom part of the figure is the centre line of the geometry. As time goes, it can be seen that the elements fail in a triangular pattern. In Figure 4.33f none of the outer elements has failed yet, but many of the elements within have. The reason for this failure pattern will be further explained below.

To understand the order of how the elements fail, the triaxiality ratio and the void volume fraction were studied. Figure 4.29a and 4.29b shows the void volume fraction vs. the equivalent plastic strain curves for different elements. Figure 4.29c shows which curve belongs to which element. The numbering of elements is done by putting the two elements at the notch root equal to element no. 1 for the inner and outer edge respectively. The neighbouring element to the left in Figure 4.33a is element no.2 and so forth. Every other element is skipped until element no. 19. In other words, every element with an odd number ranging from 1 to 19 is plotted. It can be seen that the elements along the outer edge in Figure 4.29b are more deformed compared to the corresponding elements along the inner edge seen in Figure 4.29a. The triaxiality ratios for the elements along the outer edge can be seen in Figure 4.29e, and along the inner edge in Figure 4.29d. In these figures it can be seen that the triaxiality is much higher in the elements along the inner edge compared to the corresponding elements along the outer edge. This explains why the inner elements fails first. It can be observed that the elements located just within the notch root have larger triaxiality ratios compared to the elements out at the notch root. Element no. 7 along the inner edge is the first element to fail among those plotted. From Figure 4.29d it can be seen that this element also has the highest triaxiality ratio.

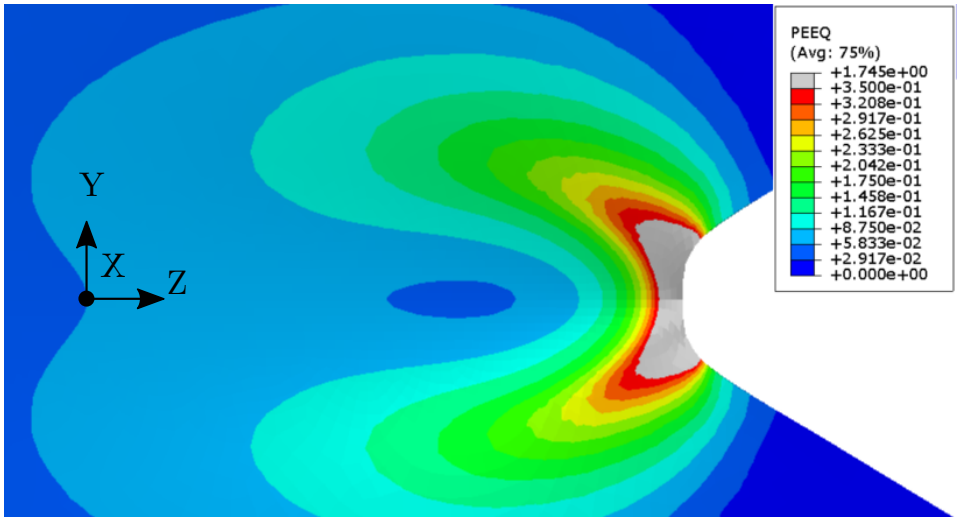

Figure 4.27: Equivalent plastic strain at maximum force in the simulation of AA6082.25 WQ.

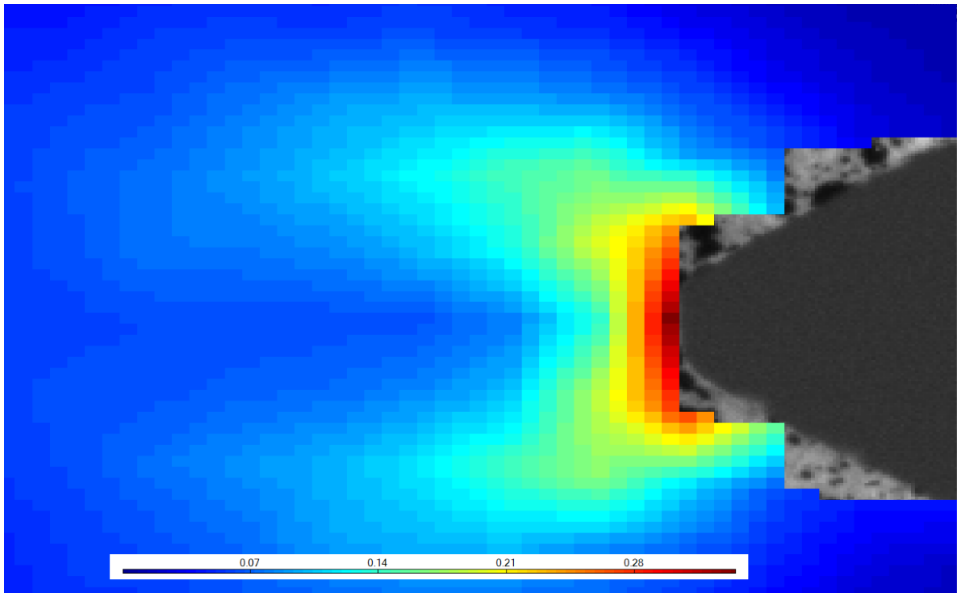

Figure 4.28: Efficient strain at maximum force in a representative Kahn tear test specimen for AA6082.25 WQ TD.

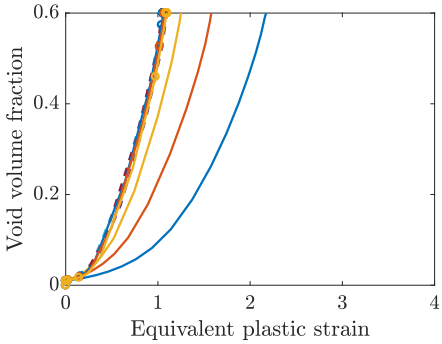

(a) Void volume fraction- equivalent plastic strain along inner edge.

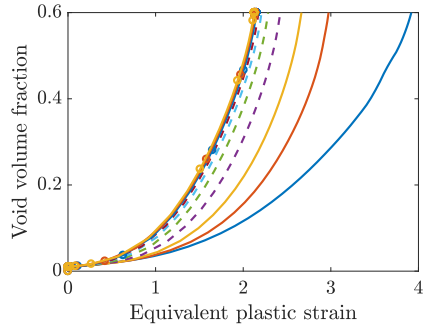

(b) Void volume fraction- equivalent plastic strain along outer edge.

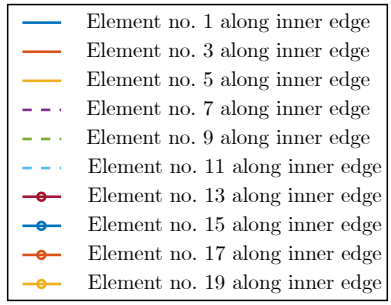

(c) Legends for Figure 4.29a, 4.29b, 4.29d and 4.29e

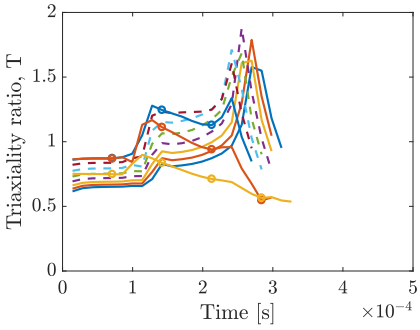

(d) Triaxiality ratio, T, along inner edge as a function of simulation time.

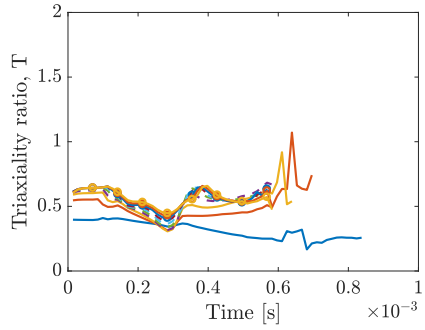

(e) Triaxiality ratio, T, along inner edge as a function of simulation time

Figure 4.29: Deformations at different point on the simulation curve in Figure 4.35.

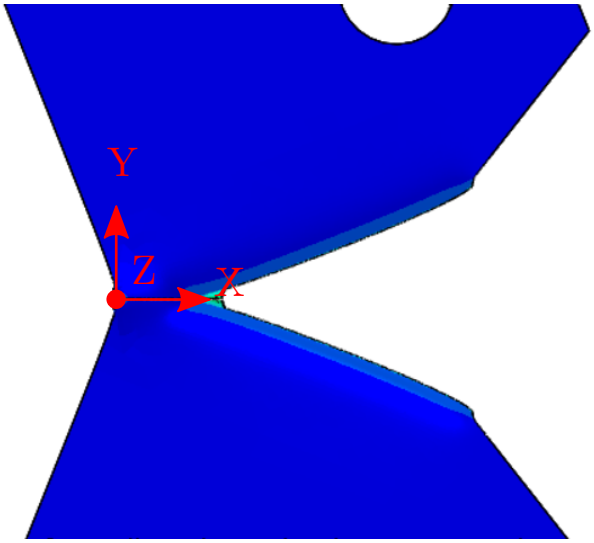

Figure 4.30: Deformed finite element model of the Kahn tear test.

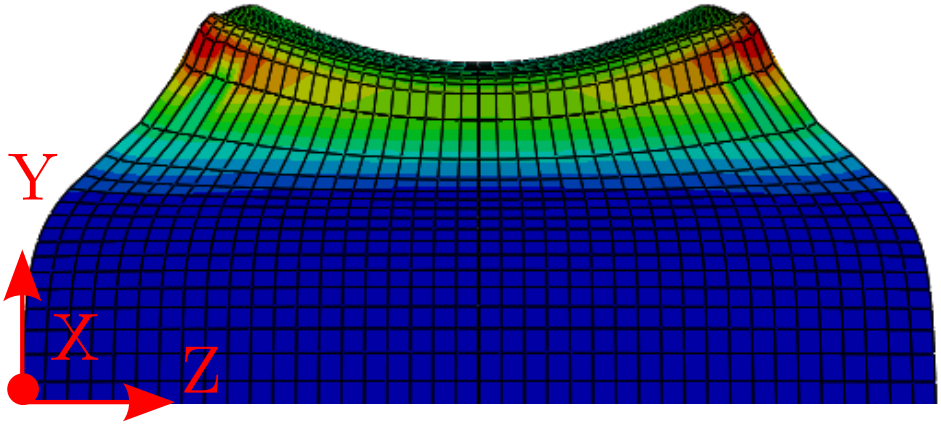

Figure 4.31: The simulation gives a distinguishable neck. This one is from AA6060 AC

Figure 4.35 shows the force-elongation curve of the simulation and experiment in TD of AA6082.25 WQ with points indicating at which point on the curves the deformations in Figure 4.34 and 4.36 are taken from. One point on the simulation curve is related to a point on the experimental curve in that the elongations at the two points are approximately the same. Figure 4.34 shows how the deformation looks like for the simulation, and Figure

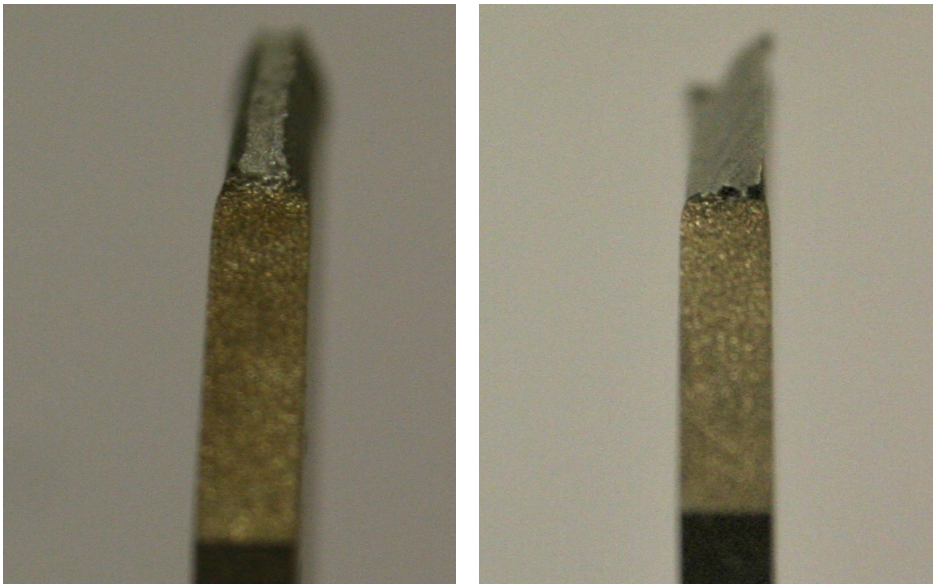

(a) AA6060 WQ TD. **(b)** AA6082.50 WQ TD.

Figure 4.32: Neck of two different water-quenched Kahn tear test specimens.

4.36 shows the deformation at the different points on the experimental curve in TD. Comparing the deformations in Figure 4.35 and 4.36 it can be seen that the experiment has a fracture surface that is not perpendicular to the loading direction. All the fracture surfaces from the simulations were similar and all were perpendicular to the loading direction. Figure 4.31 shows that the simulation using AA6060 AC exhibit necked regions. This neck was also present for the other simulations. As mentioned in Section 3.6, not all of the experiments had a distinguishable neck. The less ductile tests like AA6082.50 WQ TD, seen in Figure 4.32b has almost no neck at all. The other test specimens of AA6082.25 had almost no neck either. The neck of AA6060 WQ TD can be seen in Figure 4.32a, where a clear neck can be seen. This was also seen in some level for the other test specimens of AA6060 as well. This difference in fracture appearance further explains the difference between the simulated force-elongation curve and the experimental curves for AA6082.25 WQ.

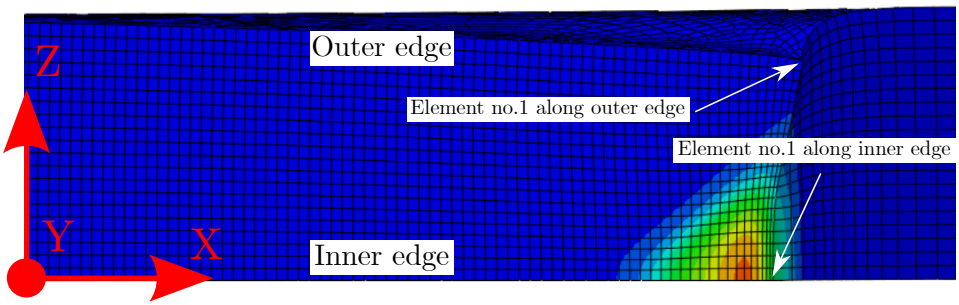

(a) Void volume fraction at a crosshead displacement of 0.51 mm. Figure also indicates inner and outer edge and numbering used for Figure 4.29.

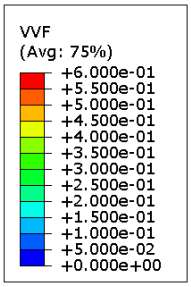

(b) Void volume fraction values for Figure 4.33a and 4.33c-4.33f.

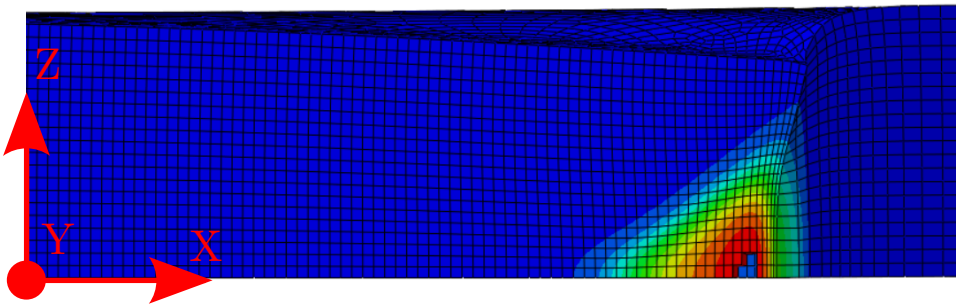

(c) Void volume fraction at a crosshead displacement of 0.57 mm.

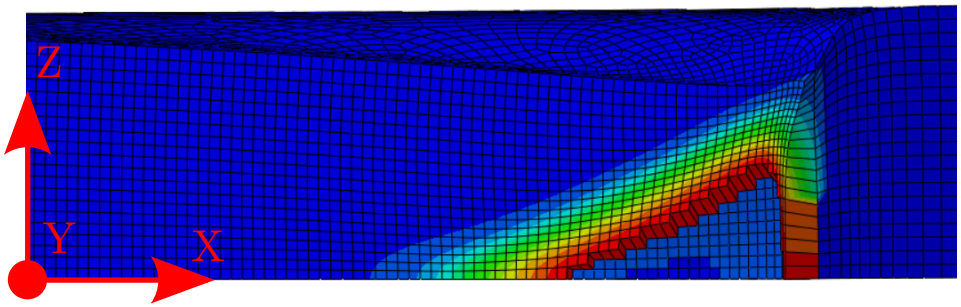

(d) Void volume fraction at a crosshead displacement of 0.74 mm.

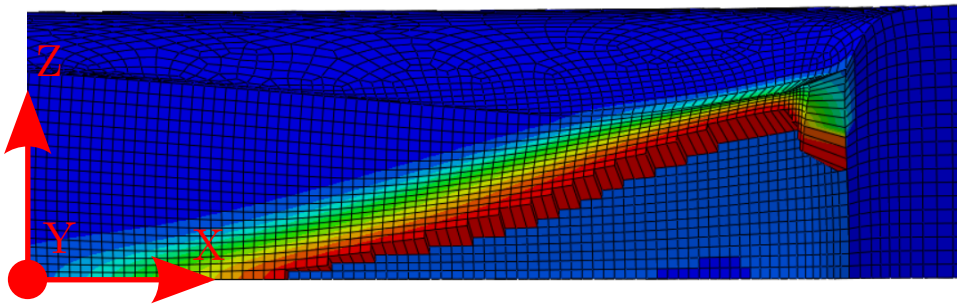

(e) Void volume fraction at a crosshead displacement of 1.08 mm.

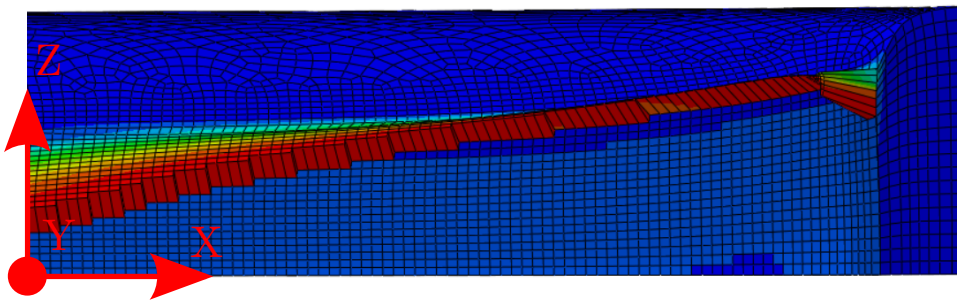

(f) Void volume fraction at a crosshead displacement of 1.65 mm

Figure 4.33: The evolution of the void volume fraction and crack propagation near the notch root for th Kahn tear test.

(a) Deformation at point 1a from Figure 4.35 with equivalent plastic strain. The test simulated is AA6082.25 WQ. The strain values are shown in Figure 4.34c.

(b) Deformation at point 2a from Figure 4.35 with equivalent plastic strain. The test simulated is AA6082.25 WQ. The strain values are shown in Figure 4.34c.

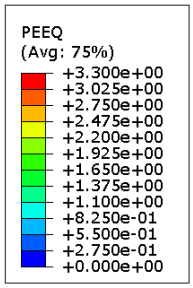

(c) Strain values for Figure 4.34a-4.34d and 4.34e-4.34f.

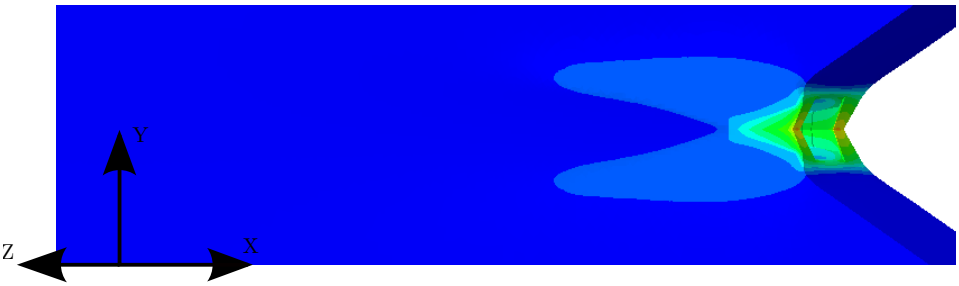

(d) Deformation at point 3a from Figure 4.35 with equivalent plastic strain. The test simulated is AA6082.25 WQ. The strain values are shown in Figure 4.34c.

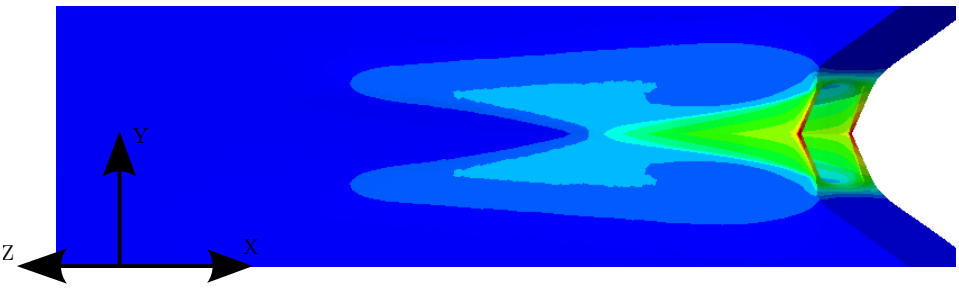

(e) Deformation at point 4a from Figure 4.35 with equivalent plastic strain. The test simulated is AA6082.25 WQ. The strain values are shown in Figure 4.34c.

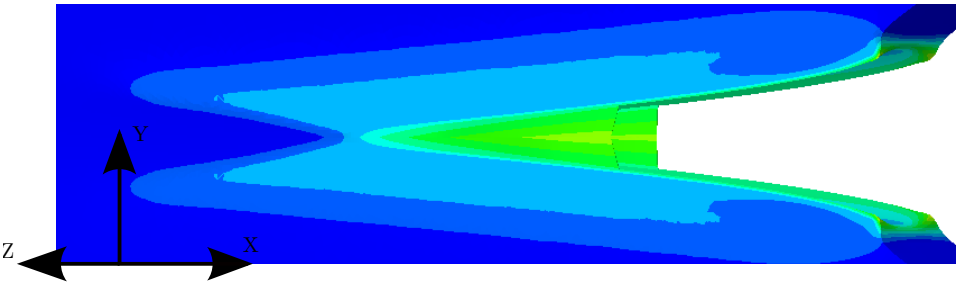

(f) Deformation at point 5a from Figure 4.35 with equivalent plastic strain. The test simulated is AA6082.25 WQ. The strain values are shown in Figure 4.34c.

Figure 4.34: Deformations at different point on the simulation curve in Figure 4.35.

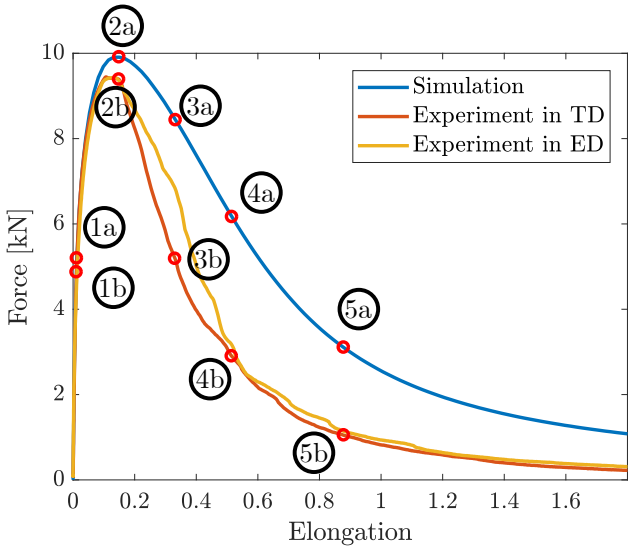

Figure 4.35: Force-elongation curves for AA6082.25 WQ with points indicating where the pictures in Figure 4.34 and 4.36 are taken from.

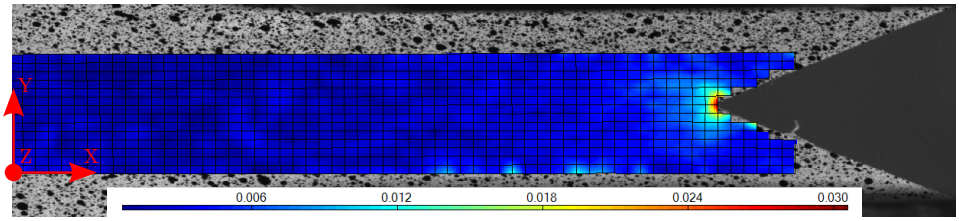

(a) Deformation of AA6082.25 WQ TD at point 1b from Figure 4.35 with effective strain.

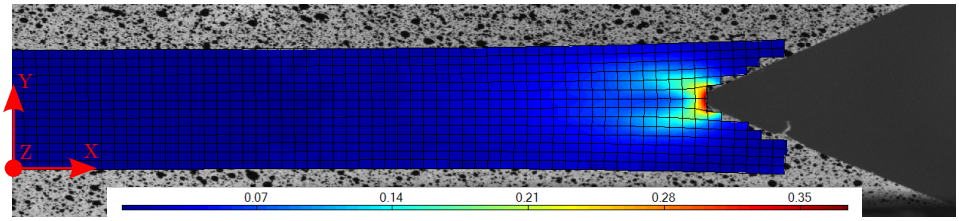

(b) Deformation of AA6082.25 WQ TD at point 2b from Figure 4.35 with effective strain.

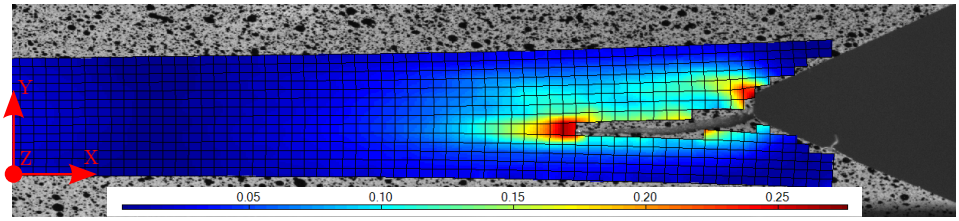

(c) Deformation of AA6082.25 WQ TD at point 3b from Figure 4.35 with effective strain.

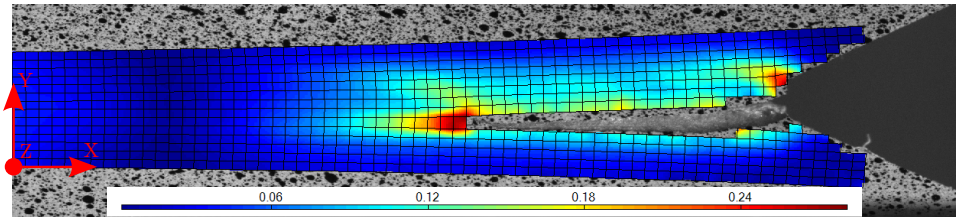

(d) Deformation of AA6082.25 WQ TD at point 4b from Figure 4.35 with effective strain.

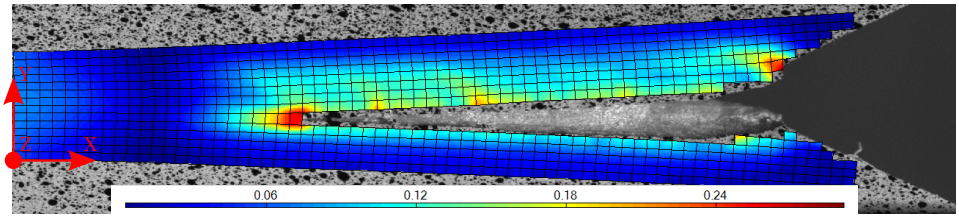

(e) Deformation of AA6082.25 WQ TD at point 5b from Figure 4.35 with effective strain.

Figure 4.36: Deformations at different point on the simulation curve in Figure 4.35.

Chapter 5

Concluding remarks

The effect of different quenching methods and different material orientations were examined for the alloys AA6060, AA6082.25 and 6082.50. AA6060 and AA6082.25 were examined using three different tests; the round smooth tensile test, the round v-notch tensile test and the Kahn tear test. The last alloy, AA6082.50 was only examined with the Kahn tear test. The test specimens for the smooth tensile tests and v-notch tests were conducted in one material orientation only. Essential mechanical properties were found for all tests.

All three tests conducted in the experimental part of the thesis were simulated. The smooth tensile tests were used to find the hardening behaviour of the different materials. The v-notch tensile tests were used to calibrate the fracture model. At the end, the Kahn tear test was modelled to examine the limitations of the GTN-model.

The conclusions are given below.

Experimental Study
For the smooth tensile test, the differences in the true-stress vs. logarithmic-strain curves were first and foremost an increased yield strength for the water-quenched compared to the air-cooled material. The hardening behaviour of the air-cooled and water-quenched AA6082.25 was a bit different, with a steeper slope for the air-cooled specimens at the beginning. For the v-notch tensile test, the air-cooled and water-quenched AA6060 had quite similar true stress vs. logarithmic strain curves, with a higher yield stress for the water-quenched material. The difference in maximum stress for AA6082.25 was much larger compared to AA6060 for both the smooth tensile test and the v-notch tensile test. The difference in strain at maximum stress was larger for AA6082.25 compared to AA6060 for both tests.

For the Kahn tear test the effect of quenching rate and material orientation was quite different for the three alloys. AA6082.25 had the most isotropic properties, but had the largest

differences stemming from quenching rate. AA6060 was least affected from quenching rate. AA6082.50 was most affected from material orientation.

The UPE of the water-quenched test specimens was larger compared to their air-cooled counterpart in three out of six cases. For the cases where it was smaller, the difference was not that large, and was mainly due to a higher maximum force. In conclusion, in terms of UPE, the water-quenched specimens were less or almost equally ductile compared to their air-cooled counterpart.

The PFZ of AA6060 AC was more than twice the size of AA6060 WQ. However, this had very little effect on the UPE. The water-quenched specimens had 9% larger UPE compared to their air-cooled counterpart for both TD and ED. The PFZ appears not to play a dominant role in this case. For AA6082.25, the UPE for the water-quenched specimens is much smaller compared to their air-cooled counterparts. This can not be explained by the PFZ-width, since the air-cooled specimens had almost ten times wider PFZ compared to their water-quenched counterparts. The difference in strength between the PFZ and the grain interior is probably not that large for the air-cooled specimens for both AA6060 and AA6082.25, resulting in a less influential PFZ.

From the fractography it seems to be more intergranular fracture present for the air-cooled specimens of AA6082.25 compared to the water-quenched counterparts. This is probably related to a wider PFZ for the air-cooled specimens. The fracture surfaces of AA6060 also had some intergranular fracture, but this was more dependent on orientation than quenching rate. The difference in PFZ-width was also smaller between air-cooled and water-quenched materials for AA6060 compared to AA6082.25. The width of the PFZ seems to influence the level of intergranular fracture. However, this does not influence the ductility in terms of the UPE in a significant way.

The same ageing period that gave peak strength for the water-quenched test specimens was applied to the air-cooled test specimen. It is not certain this ageing period gave peak strength for the air-cooled specimens. Gräf and Hornbogen [4] found that intergranular fracture was at maximum for peak strength. If the air-cooled specimens were not aged to peak strength this means that intergranular fracture could be less dominant.

Numerical Study
The fracture strains were matched very well with the calibrated initial volume fraction for the v-notch tensile test. The shape of the stress curves were simulated in a satisfactory manner, but the simulations showed larger stresses in general. The smooth tensile tests were simulated with the calibrated void volume fraction from the v-notch tensile test. The true-stress vs. logarithmic strain-curves fitted very well to the ones from the experiments. The strains at maximum stress were a bit overestimated.

The Kahn tear test was simulated using the GTN-model with the initial volume fraction calibrated from the v-notch test simulation. The force-elongation curves were plotted against the experimental data for each test. AA6060 was simulated very well, with both

the maximum force and general shape of the curve very close to the experimental curve, especially for the water-quenched one. AA6082.25 was not matched as satisfactory as AA6060, especially not the slope after maximum force, when the crack propagates.

The alloys simulated were shown to be pressure sensitive by Holmen et al. [9]. The alloys are also anisotropic. Pressure sensitivity and anisotropy effects were not accounted for. This is probably a part of the reason for overestimated stresses in the simulations, especially for the v-notch tensile test and the Kahn tear test because of higher triaxiality ratios. The overestimated stresses in the simulation of the Kahn tear test with AA6082.25 are probably also due a significant presence of intergranular fracture compared to AA6060. The GTN-model does not model this kind of fracture, only void nucleation, growth and coalescence within the grains. It may be that intergranular fracture happens with less resistance resulting in a stiffer curve for the simulations compared to the experiments.

Main result
The idea was to compare water-quenched aluminium alloys aged to peak strength to air-cooled materials aged to peak strength in order to investigate the effect of a wider PFZ. For the air-cooling, the PFZ did not affect the ductility of the materials in terms of the UPE in a significant way. The difference in strength between the grain interior and the grain boundaries was probably small, resulting a more ductile material. A wider PFZ did result in more intergranular fracture, but not the overall ductility. The overall strength was lowered, resulting in a more ductile material for the air-cooled specimens.

Chapter 6

Future work

Exploring different quenching rates
The difference in quenching rate between air-cooling and water-quenching at room temperature is quite large. It would be of interest to investigate quenching rates lying in between to see how this affects the result. Finding quenching rates that give larger difference in strength between the grain interior and PFZ is also of interest.

Finding peak strength for the air-cooled test specimens
The ageing period giving peak strength for the water-quenched test specimens were also applied for the air-cooled test specimen. It is not certain that this gives peak strength for the air-cooled test specimen. Finding the strength- ageing time curve for the air-cooled test specimens would make it possible to find peak strength.

Investigating the effect of f_F, f_c and void nucleation
The only parameter changed in the GTN-model was the initial void volume fraction, f_0. The effect of changing the void volume fraction at failure, f_F, and the critical void volume fraction, f_c, would be of interest to see how this affects the result. There was no void nucleation modelled. The effect of void nucleation could also be of interest.

Accounting for anisotropy and pressure sensitivity
Using material models that accounts for anisotropy and pressure sensitivity could give more accurate results, and should be investigated.

Expanding the GTN-model to model intergranular fracture
The GTN-model only accounts for fracture by void nucleation, growth and coalescence. It is of interest to be able to model intergranular fracture as well. This is a complex subject and should be further investigated.

References

[1] M. F. Ashby and D. R. H. Jones. *Engineering materials 1, an introduction to their properties and applications, Second edition*. Butterworth-Heinemann, 1996.

[2] D. Dumont, A. Deschamps, and Y. Brechet. On the relationship between microstructure, strength and toughness in AA7050 aluminum alloy. *Material Science and Engineering*, A356:326–336, 2003.

[3] T. F. Morgeneyer, M. J. Starink, S. C. Wang, and I. Sinclair. Quench sensitivity of toughness in an al alloy: Direct observation and analysis of failure initiation at the precipitate-free zone. *Acta Materialia*, 56(12):2872–2884, 2008.

[4] M. Gräf and E. Hornbogen. Observation of ductile intercrystalline fracture of an Al-Zn-Mg-alloy. *Acta Metallurgica*, 25(8):883–889, 1977.

[5] P. N. T. Unwin, G. W. Lorimer, and R. B. Nicholson. The origin of the grain boundary precipitate free zone. *Acta Metallurgica*, 17:1363–1377, 1969.

[6] A. L. Gurson et al. Continuum theory of ductile rupture by void nucleation and growth: Part I—Yield criteria and flow rules for porous ductile media. *Journal of Engineering Materials and Technology*, 99(1):2–15, 1977.

[7] V. Tvergaard and A. Needleman. Analysis of the cup-cone fracture in a round tensile bar. *Acta Metallurgica*, 32(1):157–169, 1984.

[8] O. Chabanet, D. Steglich, J. Besson, V. Heitman, D. Hellmann, and W. Brocks. Predicting crack growth resistance of aluminium sheets. *Computational Materials Science*, 26:1–12, 2003.

[9] J. K. Holmen, B. H. Frodal, O. S. Hopperstad, and T. Børvik. Strength differential effect in age hardened aluminum alloys. *International Journal of Plasticity*, 99:144–161, 2017.

[10] O. S. Hopperstad and T. Børvik. *Materials Mechanics Part I*. Structural Impact Laboratory, NTNU, 2015.

[11] G. Le Roy, J. D. Embury, G. Edwards, and M. F. Ashby. A model of ductile fracture based on the nucleation and growth of voids. *Acta Metallurgica*, 29(8):1509–1522, 1981.

[12] Standard test method for tear testing of aluminum alloy products. *ASTM International*, 2004.

[13] I. Polmear. *Light Alloys, from Traditional Alloys to Nanocrystals*. Elsevier, 2006.

[14] W. Z. Misiolek and R. M. Kelly. Extrusion of aluminum alloys. *ASM Handbook*, 14A: Metalworking: Bulk Forming:522–527, 2005.

[15] T. L. Anderson. *Fracture mechanics, fundamentals and applications*. Taylor and Francis, 2011.

[16] V. Tvergaard. On localization in ductile materials containing spherical voids. *International Journal of Fracture*, 18(4):237–252, 1982.

[17] V. Tvergaard. Influence of voids on shear band instabilities under plane strain conditions. *International Journal of Fracture*, 17(4):389–407, 1981.

[18] T. F. Morgeneyer. *Micromechanical Studies and Modelling of Toughness in High Strength Aluminium Alloys*. PhD thesis, University of Southampton, 2008.

[19] C.V. Singh and D.H. Warner. Mechanisms of Guinier–Preston zone hardening in the athermal limit. *Acta Materialia*, 58:5797–5805, 2010.

[20] S. C. Jha, T. H. Sanders JR, and M. A. Dayananda. Grain boundary precipitate free zones in Al-Li alloys. *Acta Metallurgica*, 35:473–482, 1987.

[21] B. H. Frodal, K. O. Pedersen, T. Børvik, and O. S. Hopperstad. Influence of precompression on the ductility of AA6xxx aluminium alloys. *International Journal of Fracture*, 206(2):131–149, 2017.

[22] O. S. Hopperstad and B. H. Frodal. Private communication. 2017.

[23] B. H. Frodal. Private communication. 2017.

[24] eCorr Documentation. `http://folk.ntnu.no/egilf/ecorr/doc/definitions/strain/logstrains.html`. Accessed: 19-10-2017.

Appendix

Fractography for all the different configurations investigated in the Kahn test are presented below.

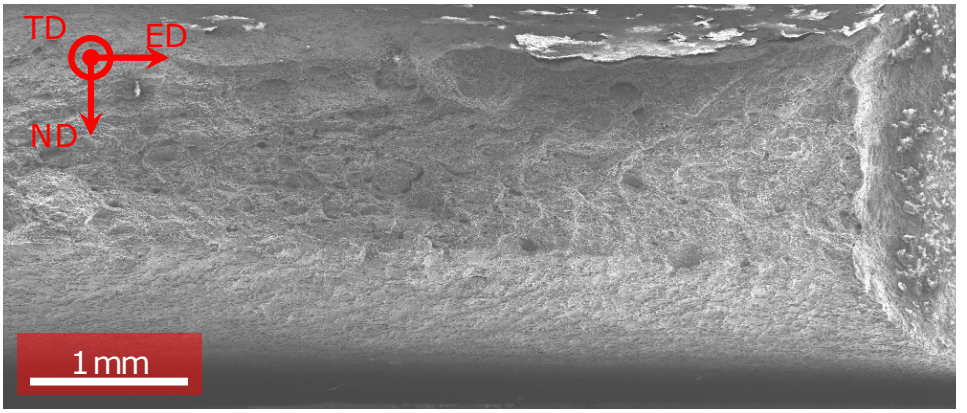

(a) Magnified by a factor of 20.

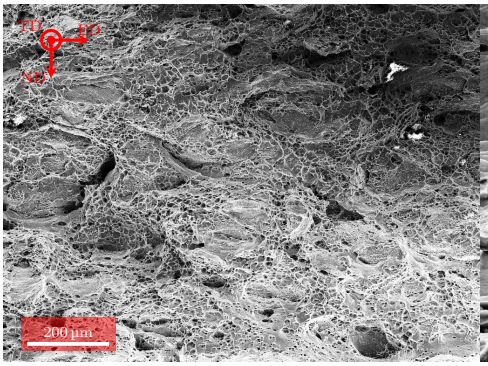

(b) Magnified by a factor of 100.

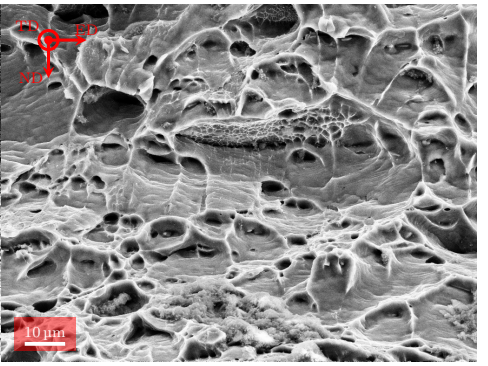

(c) Magnified by a factor of 1000.

Figure 6.1: Fracture surfaces of a AA6060 AC TD Kahn tear test specimen.

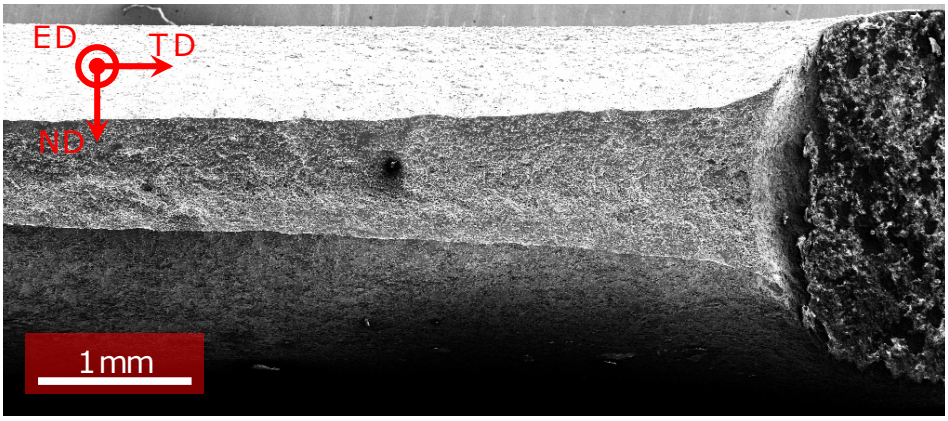

(a) Magnified by a factor of 20.

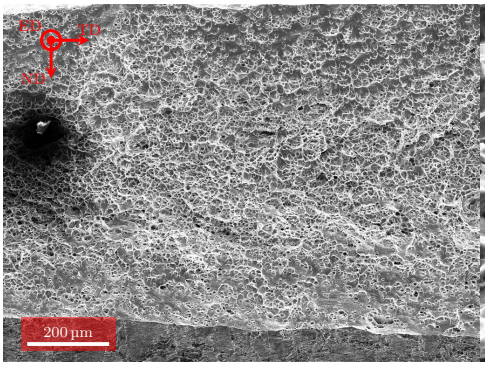

(b) Magnified by a factor of 100.

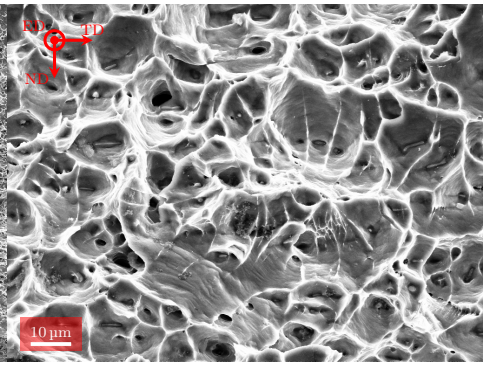

(c) Magnified by a factor of 1000.

Figure 6.2: Fracture surfaces of a AA6060 AC ED Kahn tear test specimen.

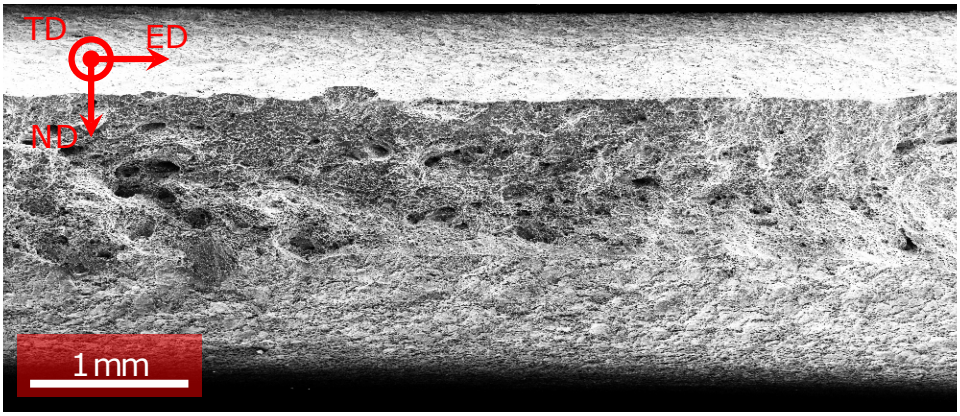

(a) Magnified by a factor of 20.

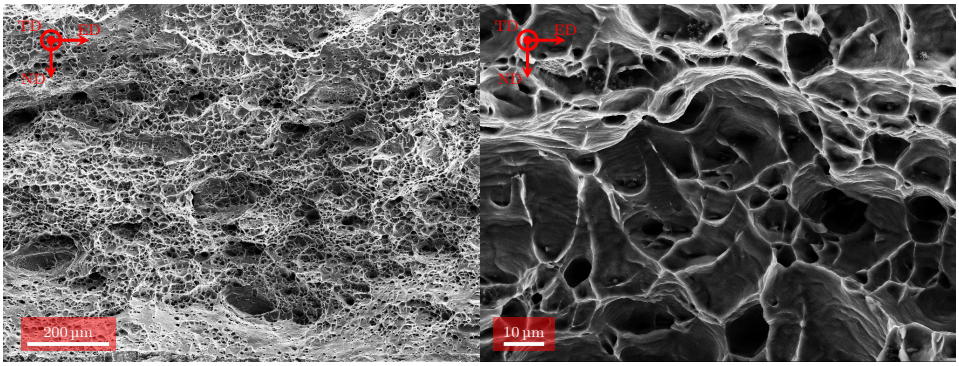

(b) Magnified by a factor of 100.

(c) Magnified by a factor of 1000.

Figure 6.3: Fracture surfaces of a AA6060 WQ TD Kahn tear test specimen.

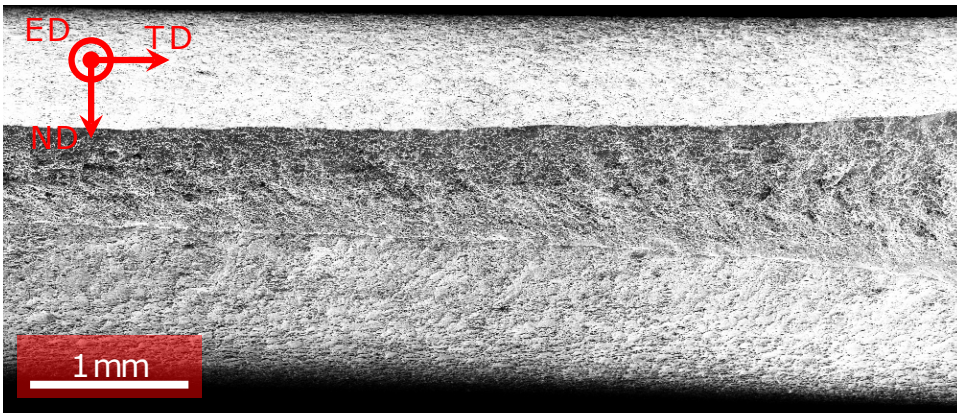

(a) Magnified by a factor of 20.

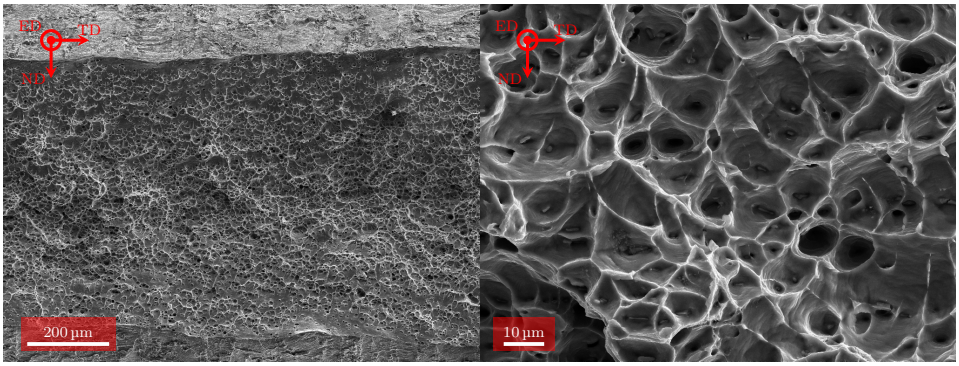

(b) Magnified by a factor of 100.

(c) Magnified by a factor of 1000.

Figure 6.4: Fracture surfaces of a AA6060 WQ ED Kahn tear test specimen.

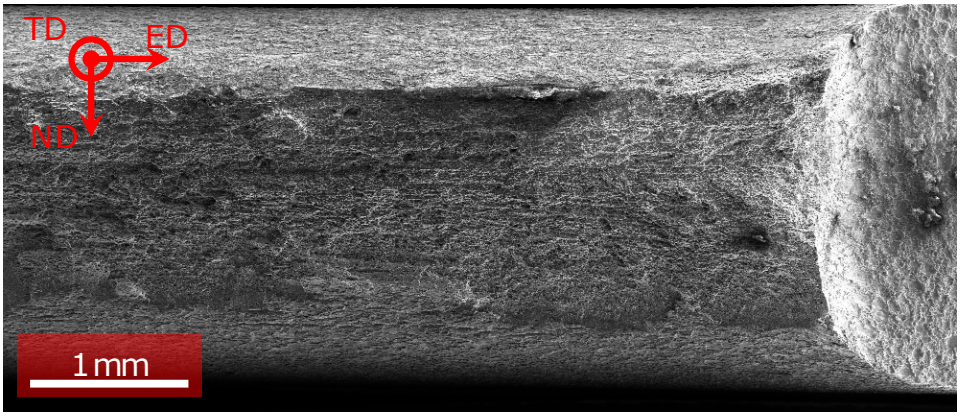

(a) Magnified by a factor of 20.

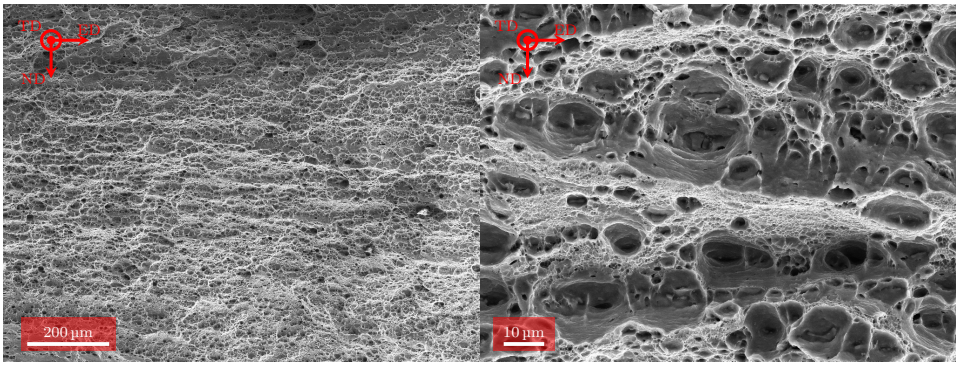

(b) Magnified by a factor of 100.

(c) Magnified by a factor of 1000.

Figure 6.5: Fracture surfaces of a AA6082.25 AC TD Kahn tear test specimen.

(a) Magnified by a factor of 20.

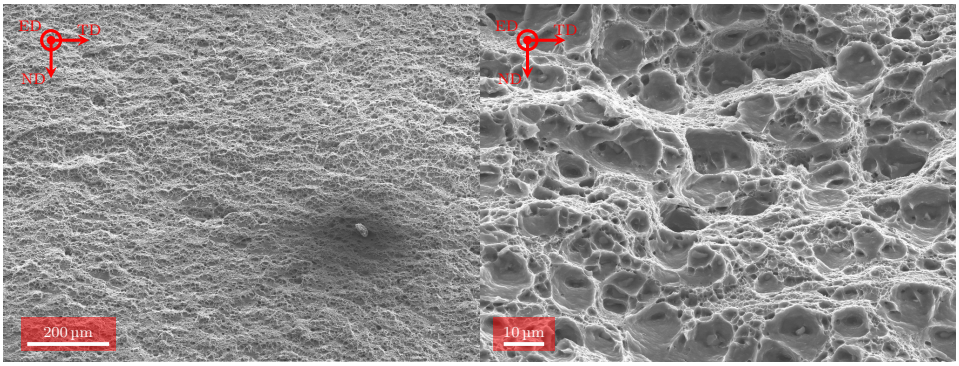

(b) Magnified by a factor of 100.

(c) Magnified by a factor of 100.

Figure 6.6: Fracture surfaces of a AA6082.25 AC ED Kahn tear test specimen.

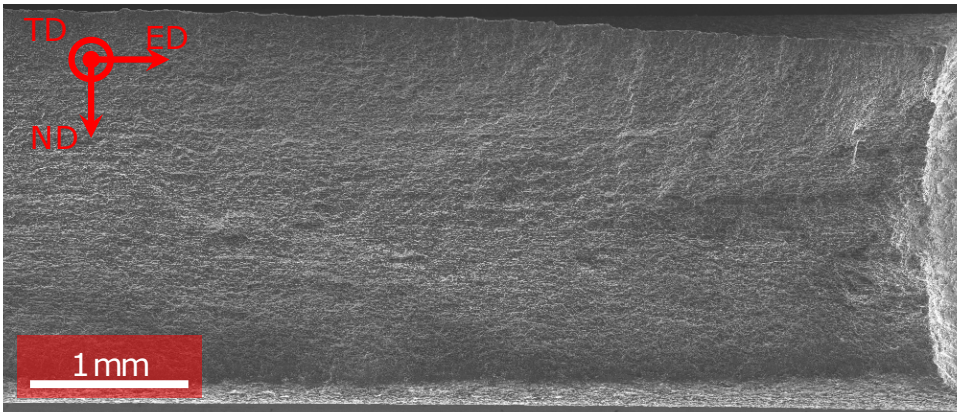

(a) Magnified by a factor of 20.

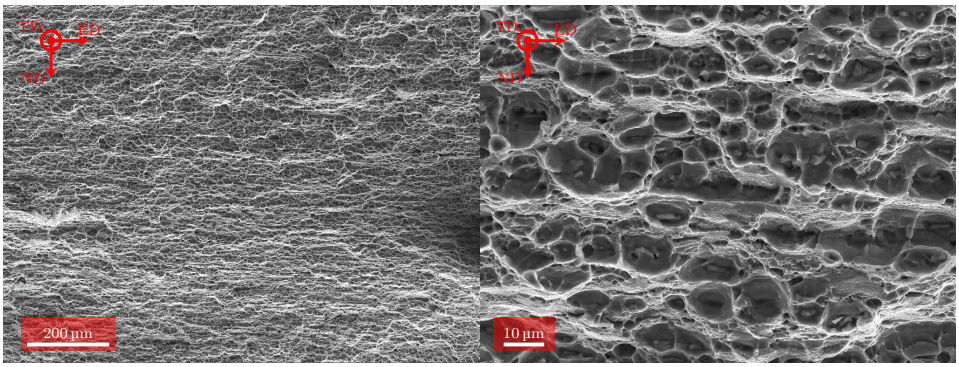

(b) Magnified by a factor of 100. **(c)** Magnified by a factor of 1000.

Figure 6.7: Fracture surfaces of a AA6082.25 WQ TD Kahn tear test specimen.

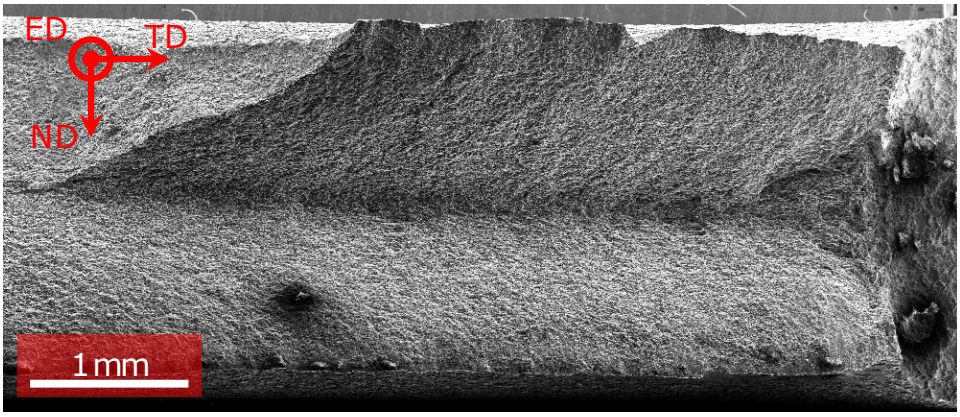

(a) Magnified by a factor of 20.

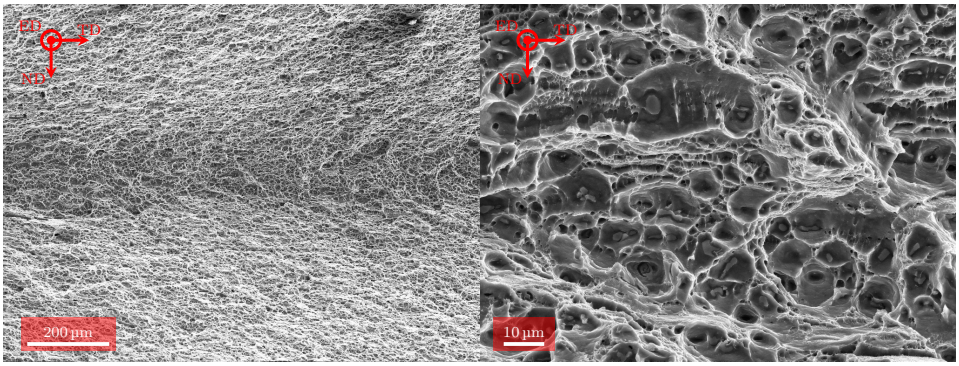

(b) Magnified by a factor of 100.

(c) Magnified by a factor of 100.

Figure 6.8: Fracture surfaces of a AA6082.25 WQ ED Kahn tear test specimen

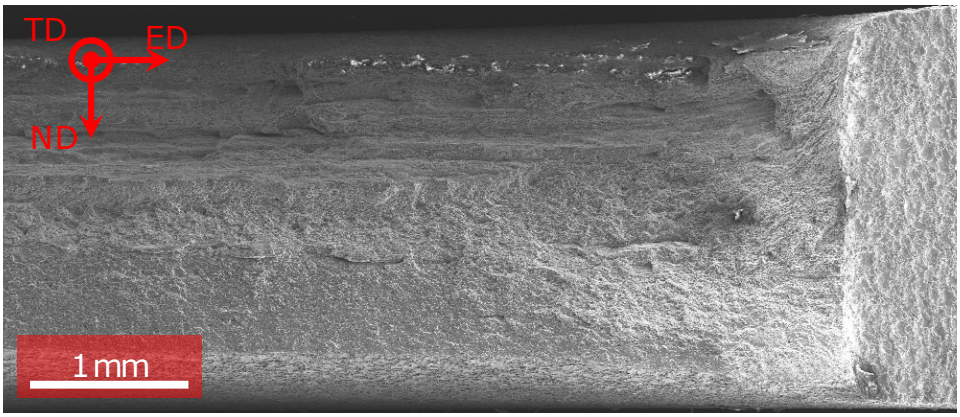

(a) Magnified by a factor of 20.

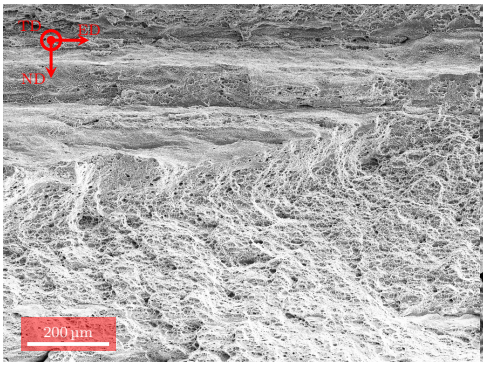

(b) Magnified by a factor of 100.

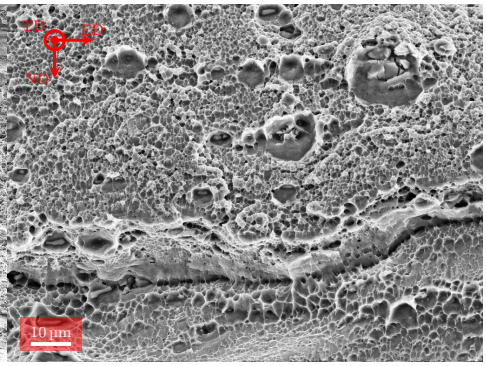

(c) Magnified by a factor of 1000.

Figure 6.9: Fracture surfaces of a AA6082.50 AC TD Kahn tear test specimen.

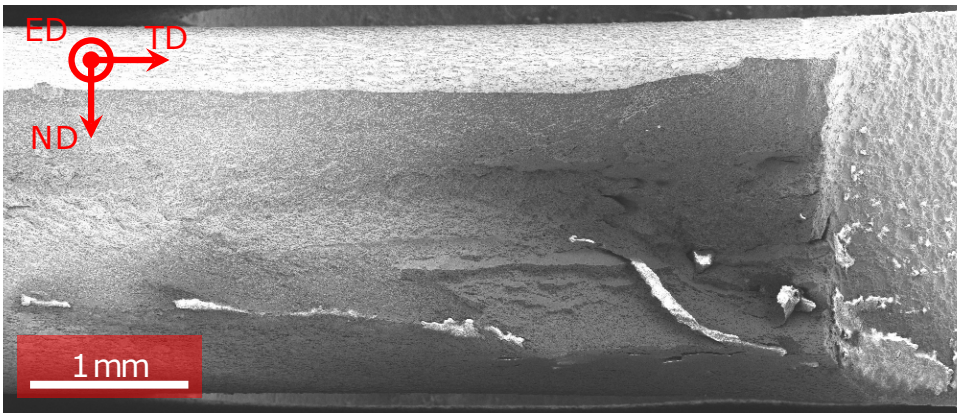

(a) Magnified by a factor of 20.

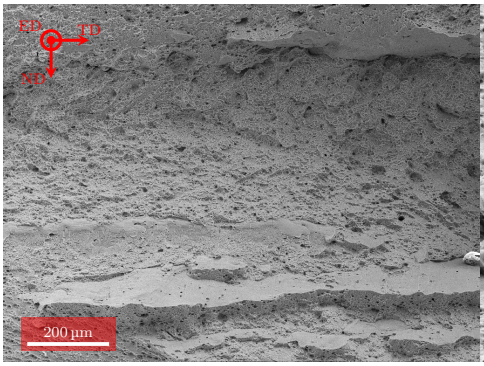

(b) Magnified by a factor of 100.

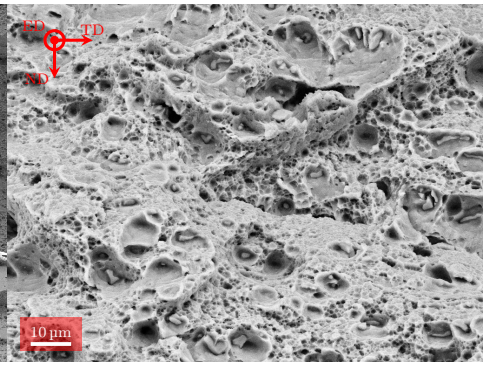

(c) Magnified by a factor of 1000.

Figure 6.10: Fracture surfaces of a AA6082.50 AC ED Kahn tear test specimen.

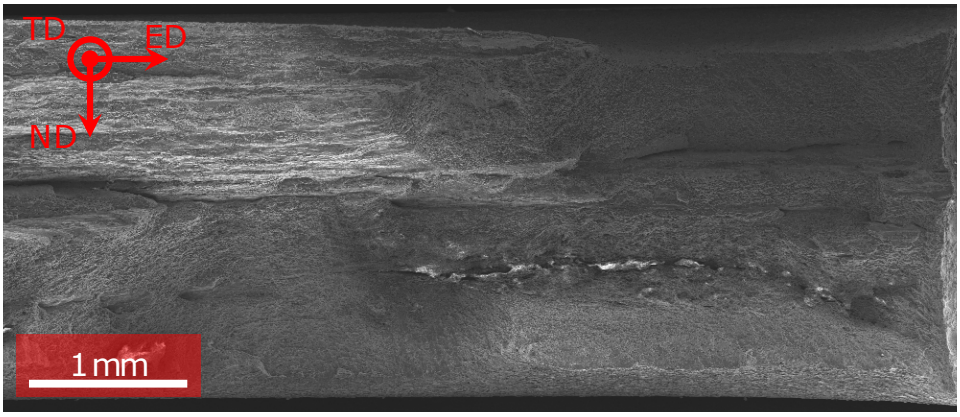

(a) Magnified by a factor of 20.

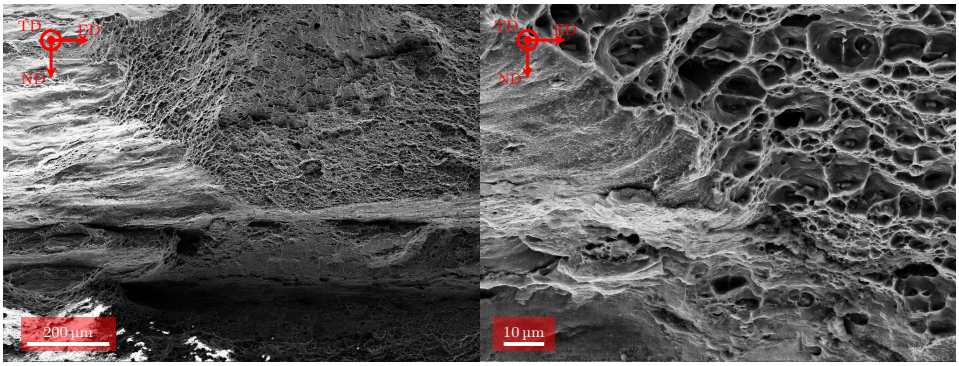

(b) Magnified by a factor of 100.

(c) Magnified by a factor of 1000.

Figure 6.11: Fracture surfaces of a AA6082.50 WQ TD Kahn tear test specimen

(a) Magnified by a factor of 20.

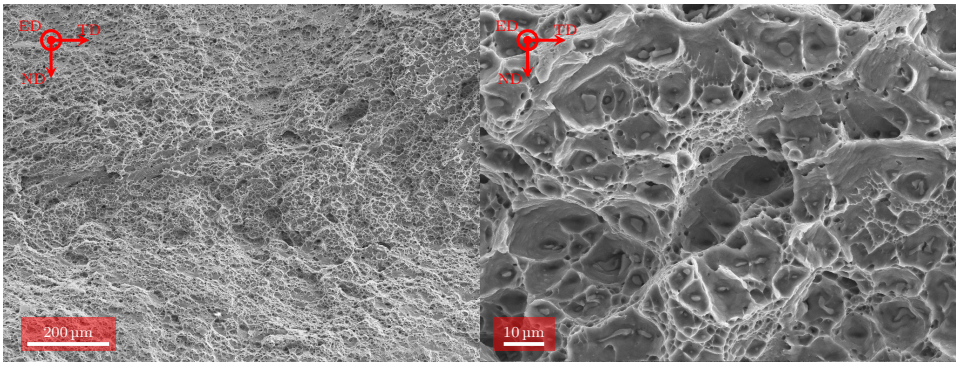

(b) Magnified by a factor of 100.

(c) Magnified by a factor of 1000.

Figure 6.12: Fracture surfaces of a AA6082.50 WQ ED Kahn tear test specimen.